Physik - Department

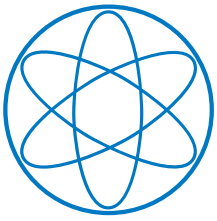

# Particle & Energy Dependence of the Near-Infrared to Vacuum-Ultraviolet Scintillation Ratio of a Liquid Argon-Xenon Mixture

Dissertation
von

Andreas Himpsl

Technische Universität München

Physik-Department

Lehrstuhl für Experimentalphysik und Astroteilchenphysik

# Particle & Energy Dependence of the Near-Infrared to Vacuum-Ultraviolet Scintillation Ratio of a Liquid Argon-Xenon Mixture

Andreas Himpsl

Vollständiger Abdruck der von der Fakultät der Physik der Technischen Universität München zur Erlangung des akademischen Grades eines

Doktors der Naturwissenschaften (Dr. rer. nat.)

genehmigten Dissertation.

Vorsitzende(r): Prof. Dr. Alejandro Ibarra

Prüfer der Dissertation:

1. apl. Prof. Dr. Andreas Ulrich
2. Prof. Dr. Lothar Oberauer

Die Dissertation wurde am 18. April 2018 bei der Technischen Universität München eingereicht und durch die Fakultät der Physik am 7. Juni 2018 angenommen.

**Abstract**

The search for the postulated weakly interacting particles of dark matter require highly sensitive scintillator materials. Investigations of the scintillator and improvements of the detectors are crucial for the energy resolution of the experiments for direct dark matter search, in particular concerning the lower limit of the mass as well as of the cross section of the postulated particles.

The present study investigated a mixture of the liquid rare gases argon and xenon with a volumetric fraction of $10^{-5}$ of xenon. The emission spectrum of this mixture was discovered in a previous work concerning the effect of impurities in liquid argon. The scintillation spectrum has two pronounced peaks: The peak of the xenon excimer in the vacuum-ultraviolet (VUV) at 174.0 $nm$ and the peak of a Wannier-Mott exciton in the near-infrared (NIR) at 1173 $nm$. The NIR emission exists solely in the liquefied rare gas mixture. The intensities of both peaks are comparable for electron-beam excitation (10.1 $keV$). Additionally, a smaller peak of the argon excimer can be found in the VUV at 127.0 $nm$.

A simplified model describes the scintillation process of both xenon emissions as a cascade: The NIR is followed by the VUV emission, each emitting one photon. In the course of this study a dependence on the particle-type as well as on the particle energy was found. Strong indications of superheating and boiling in the core of the particle tracks were discovered.

The experiments were performed to investigate the dependence of the emissions on the particle type, keeping in mind that the intensity ratio of the spectrally separated emissions could be used by future detectors for particle discrimination and background suppression. Based on the great flexibility regarding particle type and energy the experiments were performed at a linear accelerator. The accelerator was operated in continuous-beam mode and overlaps of particle tracks were excluded by setting a beam-current limit. A dependence on the particle current below the limit was not found within the measurement accuracy.

The linear energy transfer (LET) $^{dE}/_{dx}$ was expected to have an influence on the intensity ratio due to its significant effect on the excitation density. Different ions (hydrogen, lithium, carbon, sulfur, iodine) and energies (depending on the ion between 12.0 and 109.7 $MeV$, i. e. between 0.317 and 19.97 $^{MeV}/_{Nucleon}$) were chosen to cover a wide range of LETs averaged over the penetration depths (4.4 to 3500 $^{MeV}/_{mm}$). The liquid rare gas mixture was kept to be stable in a narrow temperature range and was purified continuously to prevent quenching of the emissions by impurities, like e. g. oxygen.

Two photomultiplier tubes (PMTs) were used in photon-counting mode for light detection. Each PMT is only sensitive to one of the two wavelength regions, NIR and VUV, respectively. For each individual measurement each PMT was calibrated using corresponding LEDs and photodiodes.

The measurements for every ion and the chosen energies were performed including systematic background measurements. The individual measurements using carbon ions of a certain energy were repeated on several days to determine measurement uncertainties and the reproducibility of the data.

The measured intensity ratios (NIR/VUV) vary between 0.02 and 0.17 for the present setup. Various dependences of the intensity ratios are discussed, in particular the dependence on the energy density.

The radial distribution of energy deposition due to secondary electrons along the particle path ($^{dE}/_{dx}$) is an aspect for determining of the energy density $^{dE}/_{dV}$. It can be demonstrated that the diameter of the particle track is decreasing towards the end, whereas the LET is reaching its maximum in the Bragg peak near the end. Energy deposition values in the range from $\sim 40\,^{\mu eV}/_{Atom}$ to $\sim 35\,^{eV}/_{Atom}$ and power densities in the core of the track (volume of 66 % energy deposition) larger than $\sim 2.2 \cdot 10^{21}\,^{W}/_{m^3}$ could be determined. Both quantities are strong indications of superheating and boiling within the particle tracks in the liquid rare gas mixture. This phenomenon is known as “thermal spike” from investigations of solids.

In the last part of this thesis, the knowledge gained is applied to the situation of a dark matter detector in the case of a $100\,keV$ recoil particle. The limits of only using the electronic stopping power $^{dE}/_{dx}|_{el}$ and an important influence of nuclear collisions at these low energies are discussed.

**Zusammenfassung**

Die Suche nach den postulierten schwach wechselwirkenden Teilchen der dunklen Materie erfordert den Einsatz von hocheffizienten Szintillatormaterialien. Die Untersuchung des Szintillators und die Verbesserung der Detektoren sind von entscheidender Bedeutung um eine Erhöhung der Empfindlichkeit und eine Verbesserung der unteren Grenzen für Masse und Wirkungsquerschnitt der postulierten Teilchen zu erreichen.

In dieser Arbeit wird eine flüssige Edelgasmischung von Xenon in Argon untersucht, deren Emissionsspektrum zuvor im Rahmen einer Untersuchung des Einflusses von Verunreinigungen auf flüssiges Argon entdeckt wurde. Die Mischung enthält einen Xenon-Volumenanteil von $10^{-5}$. Das Szintillationsspektrum besitzt zwei ausgeprägte Maxima: Das des Xenon-Excimers im Vakuumultraviolet (VUV) bei $174.0\,nm$ und das des Wannier-Mott-Exzitons im Nahinfrarot (NIR) bei $1173\,nm$. Die NIR-Emission tritt dabei nur in der verflüssigten Edelgasmischung auf. Die Lichtintensität beider Emissionen ist für die verwendete Mischung und unter Elektronenstrahlanregung ($10,1\,keV$) vergleichbar. Zusätzlich findet sich noch die Emission des Argon-Excimers im VUV bei $127\,nm$.

Der Szintillationsprozess kann durch ein einfaches Modell beschrieben werden, bei dem beide Xenonemissionen nacheinander (NIR vor VUV) mit jeweils einem Photon stattfinden. Im Rahmen dieser Arbeit konnte sowohl eine Teilchen- als auch eine Energieabhängigkeit des NIR-zu-VUV-Intensitätsverhältnisses nachgewiesen werden. Desweiteren wurden starke Hinweise auf ein Überhitzen und Verdampfen der flüssigen Edelgasmischung im Inneren der einzelnen Teilchenspuren gefunden.

Die Experimente wurden auf Grund der vermuteten Teilchenabhängigkeit durchgeführt, mit der Idee, das Intensitätsverhältnis (NIR/VUV) der beiden spektral weit getrennten Emissionen für zukünftige Detektoren zur Teilchenidentifikation und damit zur Unterdrückung von Untergrund nutzbar zu machen. Wegen der großen Flexibilität bezüglich Teilchenart und Energie fanden die Experimente an einem Linearbeschleuniger statt. Der Beschleuniger wurde dabei im Gleichstrommodus betrieben und eine Überlappung der Teilchenspuren durch Strombegrenzung ausgeschlossen. Eine Teilchenstromabhängigkeit unterhalb des Begrenzung wurde innerhalb der Messgenauigkeit nicht gefunden.

Ein möglicher Einfluss auf das Intensitätsverhältnis wurde vom linearen Energietransfer (LET) $^{dE}/_{dx}$ erwartet, weil er maßgeblich zur Anregungsdichte beiträgt. Um einen großen Bereich des mittleren LETs in der flüssigen Argon-Xenon-Mischung

abzudecken ($4,4$ bis $3500\,{}^{MeV}/_{mm}$), wurden verschiedene Ionen ausgewählt (Wasserstoff, Lithium, Kohlenstoff, Schwefel, Iod) und mit unterschiedlichen Energien (je nach Ion zwischen $12,0$ und $109,7\,MeV$ bzw. zwischen $0,317$ und $19,97\,{}^{MeV}/_{Nukleon}$) auf die verflüssigte Edelgasmischung geschossen. Die flüssige Edelgasmischung muss dabei in einem engen Temperaturbereich stabil gehalten und kontinuierlich gereinigt werden, um keine Auslöschung der Emissionen durch Verunreinigungen, wie z. B. Sauerstoff, zu bekommen.

Die Lichtdetektion im Experiment wurde mit zwei Photoelektronenvervielfachern (PMTs) im Photonenzählmodus durchgeführt. Jeder der beiden PMTs ist jeweils nur auf einen der beiden Wellenlängenbereiche, NIR bzw. VUV, empfindlich und wurde mit entsprechenden LEDs und Photodioden bei jeder Einzelmessung kalibriert.

Die Messungen für jedes Ion und die jeweils ausgewählten Energien erfolgte nach einem festen Messprotokoll, das auch systematische Untergrundsmessungen einschließt. Die Einzelmessungen mit Kohlenstoff einer bestimmten Energie wurden dabei an jedem Tag wiederholt, um die Messgenauigkeit und die Reproduzierbarkeit der Daten zu bestimmen.

Im verwendeten Aufbau variieren die Intensitätsverhältnisse (NIR/VUV) in einem Bereich von $0,02$ bis $0,17$. Es werden verschiedene Abhängigkeiten des Intensitätsverhältnisses –insbesondere von der Energiedichte – diskutiert.

Für die Bestimmung der deponierten Energiedichte ${}^{dE}/_{dV}$ im Medium wurde der Aspekt der radialen Verteilung der Energiedeposition durch Sekundärelektronen entlang des Teilchenpfades (${}^{dE}/_{dx}$ aus SRIM-Daten) verwendet. Es kann gezeigt werden, dass der Teilchenspurdurchmesser zum Ende hin abnimmt, während der lineare Energietransfer erst dort im Bragg-Peak sein Maximum erreicht. Es wurden Energiedepositionen in Bereichen von $\sim 40\,{}^{\mu eV}/_{Atom}$ bis $\sim 35\,{}^{eV}/_{Atom}$ und Leistungsdichten bis zu mindestens $\sim 2,2 \cdot 10^{21}\,{}^{W}/_{m^3}$ im Kern (Volumen mit $66\,\%$ Energiedeposition) der Teilchenspuren bestimmt. Beide Größen sind starke Anzeichen dafür, dass es in den Teilchenspuren zur Überhitzung und zum Verdampfen der flüssigen Edelgasmischung kommt, ein Phänomen, das aus Untersuchungen von Festkörpern als "Thermal Spike" bekannt ist.

Im letzten Teil der Arbeit werden die gewonnenen Erkenntnisse auf die Situation eines Teilchendetektors im Falle eines $100\,keV$-Rückstoßteilchens angewendet. Dabei werden die Grenzen der alleinigen Betrachtung des elektronischen Bremsvermögens ${}^{dE}/_{dx}|_{el}$ und der dominante Einfluss von Kernstößen bei diesen niedrigen Energien diskutiert.

# Contents

# Chapter 1

# Introduction

## 1.1 Dark Matter in the Universe

One of the great endeavors in modern astroparticle physics is the search for dark matter candidates.

Already in the first half of the 20th century, different physicistsfound a discrepancy between the observed mass and the distribution of stellar velocities within spiral galaxies (rotation curves). Besides the modification of gravitational theories, the most popular explanatory approach is the postulation of dark matter [1, 2, 3, 4, 5]. Additional indications for dark matter have been found ever since, like in recently more thoroughly investigated gravitational lens effects [6]. The identification of dark matter particles would expand the standard model of particle physics.

Today, the aim is still to proof the existence of particles of non-ordinary matter. Several dark matter particles have been postulated, but most of them have outstanding parameters, making it even harder to detect them [7]. Suspects that should soon be reachable in their mass and cross-section parameter-space are axions, extremely light particles with a boson-like character which can couple very weakly to electromagnetic radiation and to baryonic matter [8, 9]. Other potentially detectable candidates are WIMPs, the weakly interacting massive particles, that – as the name suggests – couple only via the weak interaction to observable matter [5].

## 1.2 Direct Dark Matter Search Experiments

The detection of any kind of dark matter particles could be achieved in two ways. Firstly in an indirect manner by searching for products of specific particle reactions

or by the analysis of collisions in high-energy colliders. Secondly by direct detection via scattering processes in baryonic matter [10]. In the following the focus is on these scattering processes, enabling the direct dark matter search.

Nucleus scattering of dark matter candidates can be detected using baryonic matter. The core issue is to find materials which offer a high sensitivity and a high purity. However, also high densities are a beneficial for the experiments. Based on various detector materials different direct dark matter experiments have been developed.

A detector concept that is using phase transitions is PICO at the Laboratori Nazionali del Gran Sasso (LNGS) in Italy. This concept is using different superheated carbon compounds, following the technique of a bubble chamber. The amount of target material in the largest one those chambers is $36.8\,kg$ [11].

There are not many experiments left that are working with less than $1\,kg$ of target material. But the DAMIC experiment at SNOLAB, Canada is installed with $100\,g$ of highly sensitive charge-coupled devices based on $Si$. With this technology it is possible to record intensity and position [12].

Also $Ge$ is a possible semiconductor material. It is point-contacted and cooled to liquid nitrogen temperatures in the CDEX experiment. This experiment is using $1\,kg$ of $Ge$ and is located at CJPL in China [13].

Even lower temperatures are used in the cryogenic dark matter search. The SuperCDMS experiment, tested in the Soudan Underground Laboratory in USA and heading for SNOLAB in Canada, uses superconducting films on $Ge$ of several hundred grams. Due to the superconducting film these detectors have to be cooled to $\sim 45\,mK$ for the detection of phonons in addition to photons [14, 15].

Another cryogenic rare event search with superconducting thermometers (CRESST) is located at the LNGS, using $CaWO_4$ crystals in combination with a light detector for the dark matter search. Their operation temperature is at $\sim 10\,mK$ and puts the detector modules into a position for a leading exclusion limit for WIMPs down to $0.35\,{}^{GeV}/_{c^2}$ [16, 17, 18, 19].

A great variety of experiments is using liquid rare gases. Rare gases are known for their high scintillation yields and the density of the liquid phase is high enough to allow experiments with a feasible spatial expansion by still reaching adequate kilogram-year-values of exposure for the detectors ([20, 21, 10] and refs. therein). Especially $Ar$ and $Xe$ are widely used. Two kinds of liquid rare gas detectors often used in rare event search will be described in the next section.

## 1.3 Liquid Rare Gas Detectors in Dark Matter Search

The great benefit of liquid rare gases is their outstanding scintillation efficiency [22, 20] and linearity regarding energy measurements [23, Ch. 8, 19]. Their low $W$-values[1] of $23.6\,eV$ for liquid $Ar$ and $15.6\,eV$ for liquid $Xe$ [23, Ch. 19], lead to promising high energy resolutions of $2.7\,\%$ [24] and $4.3\,\%$ [25], respectively.

Liquid scintillators do not bind free electrons [26] and an applied electric field of $\sim 10^{5}{}^{V}/_{m}$ allows to separate the created ion-electron pair at a saturated electron drift velocity of $3{\cdot}10^{13}{}^{m}/_{s}$ [27, 28]. The drift length of electrons can reach several meters in pure rare gases [29]. Thus, large detector volumes are feasible, whereby $Ar$ is the cheaper solution but $Xe$ can score with its lower $W$-value. The application of electric fields led to the development of the time protection chamber (TPC) method in the 1970s [30]. As the drift velocities are known, a position reconstruction can be made by time measurements between scintillation light and charge pulses [31]. Each of both signals allows a measurement of the energy deposition. The next step is the use of a partially condensed liquid — thus the detector chamber contains a liquid to gas phase boundary — a so-called double phase detector. Using high electric fields perpendicular to the phase boundary, ion-electron pairs can be separated after their generation by an incident particle before recombination occurs. Once the separated charges leave the liquid phase, a light signal proportional to the amount of charge is generated [30, 32, 33].

Liquid rare gas double-phase detectors combine several advantages: The high probability of interaction of incident particles with the dense scintillation medium, the high scintillation yield of rare gases, the charge multiplication and light generation of accelerated electrons [34, 35], and the relatively easy purification of large amounts by continuous cycling [26]. Examples for this kind of detector are the XENON10 and XENON100 experiments as well as their successor XENON1T, which are located at LNGS and mainly differ in the mass of the active volume with $3.5\,t$ in the largest one [36, 37, 38]. The American counterpart is the LUX experiment at the Stanford Underground Research Facility (SURF) which will be followed by the LZ experiment, containing $7\,t$ of liquid $Xe$ [39, 40]. In China the particle and astrophysical xenon (PandaX) experiments are using double-phase $Xe$ detectors, too [41, 42]. The rare gas $Ar$ is also operated in a double-phase setting in the DarkSide experiments at LNGS [43, 44].

Besides the double-phase concept also single-phase detectors have been involved in the dark matter search. In the Kamioka mine in Japan the XMASS detector

[1] The energy necessary to create an ion pair.

is installed, using nearly $1\,t$ of liquid $Xe$. A successor containing $5\,t$ is planned [45, 46]. The $Ar$ counterpart is the Canadian DEAP-3600 experiment at SNOLAB with a $3.6\,t$ filling. DEAP-50T is already in development [47, 48].

The wide use of liquid rare gases emphasizes the importance of detailed studies on these materials. The next section will describe a $Xe$-related feature. This emission feature was found during impurity measurements.

## 1.4 Discovery of a NIR/VUV-Scintillating Liquid Ar-Xe Mixture

The Physics Department of the Technical University of Munich is heavily involved in dark matter search experiments. This includes the production and investigations of $CaWO_4$ as a solid scintillator for the CRESST experiment [18] as well as of liquid $Ar$ for GERDA [49, 50] as a veto. Furthermore, liquid $Ar$ is studied as a scintillation material for various experiments.

Studying scintillation properties of liquid $Ar$ includes, besides the emission spectrum [51], the measurement of the attenuation length – especially of its own scintillation light – and effects of impurities as well as the time spectra of the light emission [52, 53].

In this context a characterization of the impact of a xenon impurity[2] on the scintillation spectrum of liquid argon was investigated by A. Neumeier [54]. He observed the vacuum-ultraviolet (VUV) scintillation of $Ar_2^*$ and $Xe_2^*$ excimers and discovered an unknown near-infrared (NIR) emission in the liquid mixture of both rare gases.

### 1.4.1 Emission Spectrum

All rare gases have emissions in the vacuum-ultraviolet wavelength region, between $60\,nm$ ($He$) and $190\,nm$ ($Xe$), as can be seen in figure 1.1. The broad intense peak emitted by the rare gases has its origin in a special scintillation mechanism.

[2] Heavier rare gas atoms are easier to ionize than lighter ones. Thus, light of the heaviest rare gas component is always most intense.

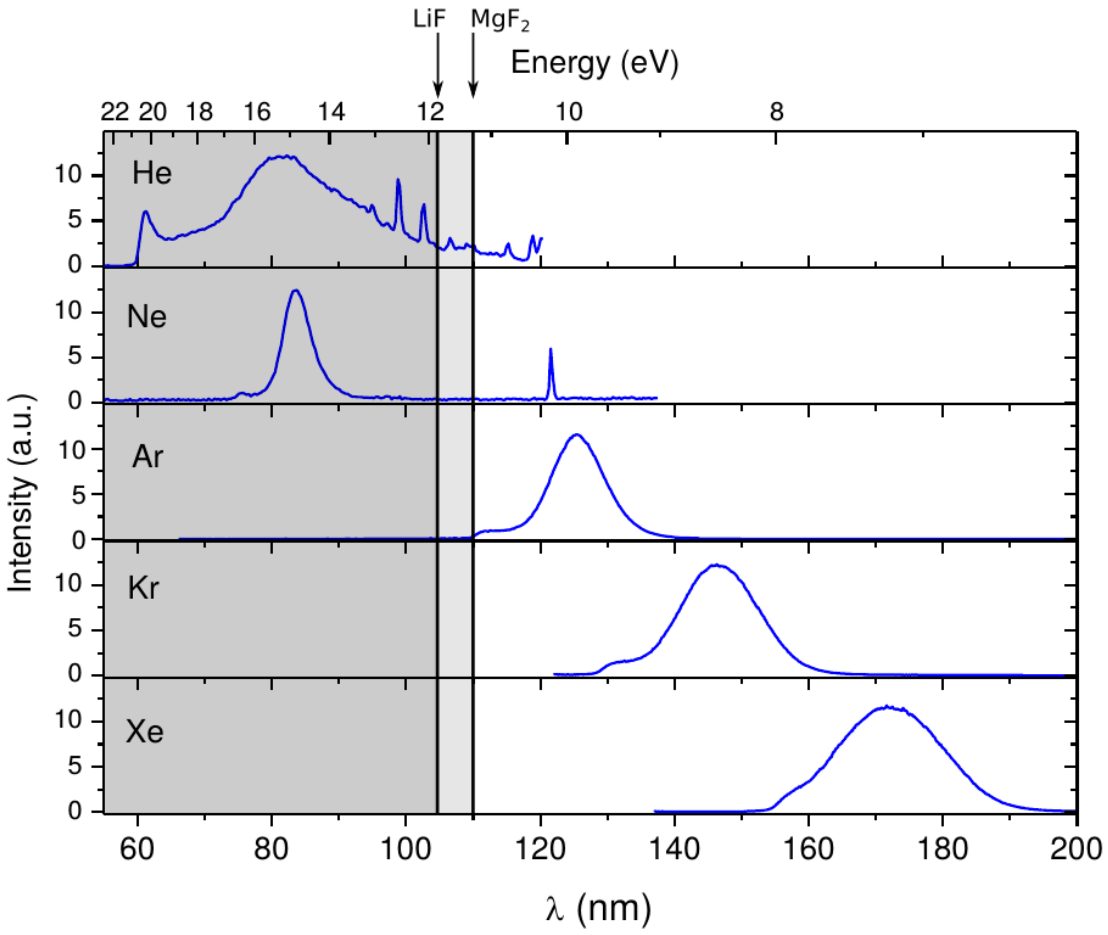


**Figure 1.1:** The emission spectra of the rare gases induced by electron beam excitation are shown. The scintillation is in the vacuum-ultraviolet wavelength region. The gray-shaded areas are opaque even for short-wavelength windows like $MgF_2$ and $LiF$. This figure is taken from [54].

The scintillation mechanism of pure rare gases is comparatively simple: After collisional excitation the rare gas atoms' orbitals change their character from repulsive to attractive, leading to the formation of excited dimers, the excimers. When returning to the ground state, preceded by vibrational relaxation within the attractive potential, the energy difference is released in terms of a photon in the vacuum-ultraviolet wavelength region. Further information on excimers can be gained from references [55, 56].

Emission spectra of rare gases – and several others – had been investigated for a period of over hundred years. In the 1970s Striganov and Sventitskii published detailed tables for emission lines from the extreme-ultraviolet (EUV $\sim 10\,nm$)

to the mid-infrared (MIR $\sim 30\,\mu m$) [57]. In these tables, wavelengths for neutral and ionized rare gas atoms can be found up to $\approx 26\,\mu m$. These infrared emissions have been one of the reasons for expanding spectral studies into longer wavelength regionsand they are of particular interest until today [58, 59, 60].

Significant changes happen to the known rare gas emissions if the excited rare gas is condensed into the liquid phase. Since the intensity of the emission features range over several orders of magnitude these changes are best seen by the use of a logarithmically scaled intensity axis.

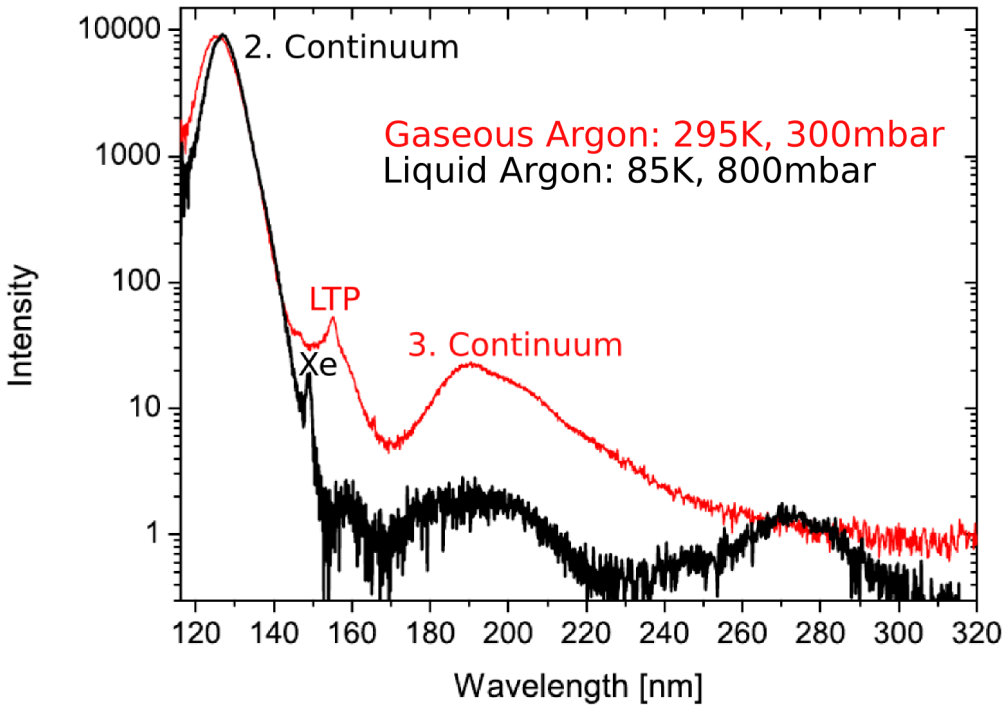


**Figure 1.2:** Electron-beam excited emissions of pure gaseous (red) and pure liquid (black) $Ar$. The intensity axis is logarithmic to depict all excimer related features: The 2. continuum, the classical left turning point (LTP), and the 3. continuum. Besides the 2. continuum, the other excimer features are decreased by the condensation of the rare gas. Here the liquid $Ar$ also shows a $Xe$ impurity at $149\,nm$. The measurements were performed by T. Heindl [51], the diagram is taken from [54].

Figure 1.2 shows the scintillation spectra for gaseous and liquid $Ar$ in the ultraviolet. These spectra were recorded using electron beam excitation by T. Heindl [51, 61]. The gas spectrum shows all excimer emission features very well in logarithmic scaling, such as the 3. continuum and the classical left turning point (LTP). The 2. continuum

is already prominent in the linearly scaled diagram in figure 1.1. The liquid spectrum shows a small shift of the center wavelength of the 2. continuum and the reduction of the other excimer features. It also demonstrates that purification is crucial for liquid rare gases. The $Xe$ impurity that can be seen here is one of the reasons that led to a study of the influence of impurities on the scintillation light in the liquid rare gas $Ar$.

The mixing of several rare gases had been already practiced in gas laser applications. $Ar$-$Xe$ mixtures, for example, can emit near-infrared light at $1.73\,\mu m$ in the gas phase ($600\,mbar$). The admixture of a second component helps the population inversion for the laser transition in the dense gas to occur and allows continuous mode operation [62, 63, 64]. On the other hand, admixtures of a second rare gas component have to be treated as an impurity in dark matter detectors.

Investigating small admixtures[3] of $Xe$ to liquid $Ar$ a NIR emission was found at $(1173 \pm 99)\,nm$. This study also used electron-beam excitation. In figure 1.3 the emission spectrum of an $Ar$-$Xe$ mixture with a fraction by volume[4] of $10^{-5}$ of $Xe$ can be seen [54, 53]. The first peak in the spectrum at $(127.0 \pm 7.4)\,nm$ is the $Ar_2^*$ excimer emission and is reduced with increasing $Xe$ content [54]. The excitation energy feeding this $Xe_2^*$ excimer emission is redirected from the $Ar_2^*$ excimer. This leads to the peak at $(174.0 \pm 8.6)\,nm$ with a measured scintillation efficiency of $(20\,000 \pm 6\,000)\ {}^{Photons}/_{MeV}$ [53]. The very small peak between the two VUV emission features is an overlap of two optical transitions and originates from the $Xe$ resonance line at $147\,nm$ and the hetero-nuclear $ArXe^*$ excimer [65] at $149\,nm$. The intensity of the latter is nearly an order of magnitude higher for $Xe$ concentrations lower than $10^{-5}$ (compare Fig. 3 in [53]). The NIR emission at $1173\,nm$ is a result of sufficient doping with $Xe$. It increases with the amount of $Xe$ until a fraction by volume of $10^{-5}$, i. e. $10\,ppm$, in $Ar$ is reached as can be seen in figure 1.4.

This specific mixture was afterwards called optimal, as the NIR light yield was at a maximum. Both the NIR emission at $1173\,nm$ and the VUV emission at $174\,nm$ are comparable in terms of the emitted photons per excitation energy, $(13\,000 \pm 4\,000)\ {}^{Photons}/_{MeV}$ and $(20\,000 \pm 6\,000)\ {}^{Photons}/_{MeV}$, respectively.

[3] Ratios from $10^{-7}$ to $10^{-3}$ of $Xe$ in $Ar$ were investigated by A. Neumeier by variations in factors of 10. [54]

[4] Since the mixing was done in the gas phase using a pressure gauge, the fraction of $Xe$ given refers to the partial pressure which is equal to the mole fraction and the volumetric fraction for ideal gases.

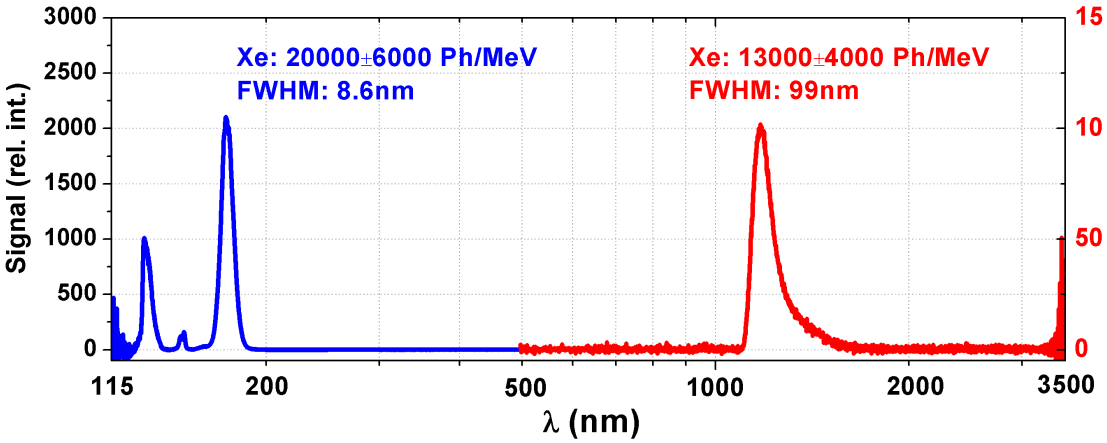


**Figure 1.3:** Wavelength-resolved emission spectrum of liquid $Ar$ containing a volumetric fraction of $10^{-5}$ $Xe$ excited by a $12\,keV$ electron beam. The scintillation signal is plotted against a logarithmic wavelength axis. The data was obtained by A. Neumeier [54]. The blue curve was recorded with a UV photomultiplier, the red curve using an infrared photodiode. The two most prominent peaks at $174\,nm$ and $1173\,nm$ are denoted with their integral scintillation efficiencies and can be assigned to states of the $Xe_2^*$ excimer and an $Ar$-$Xe$-Wannier-Mott state, respectively. At the very edges of the diagram the limitations of the detectors lead to reduced signal-to-noise ratios. This figure is from [53].

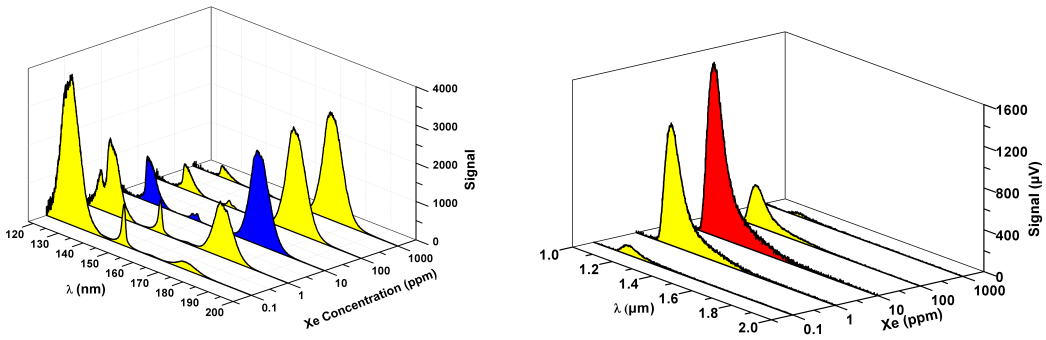


**Figure 1.4:** Emission spectra for different $Ar$-$Xe$ mixtures using electron-beam excitation. The signal intensities in the VUV (left) and NIR (right) regions are shown for varying $Xe$ admixtures. An "optimum" volumetric fraction of $10^{-5}$ $Xe$ in liquid $Ar$ is marked in blue and red, respectively. The figures are from [53] and [66].

### 1.4.2 Scintillation Mechanism

Using emission and absorption spectra as well as time-resolved scintillation measurements Neumeier et al. [67] proposed a possible scintillation mechanism for the newly discovered NIR emission, which is illustrated in figure 1.5.

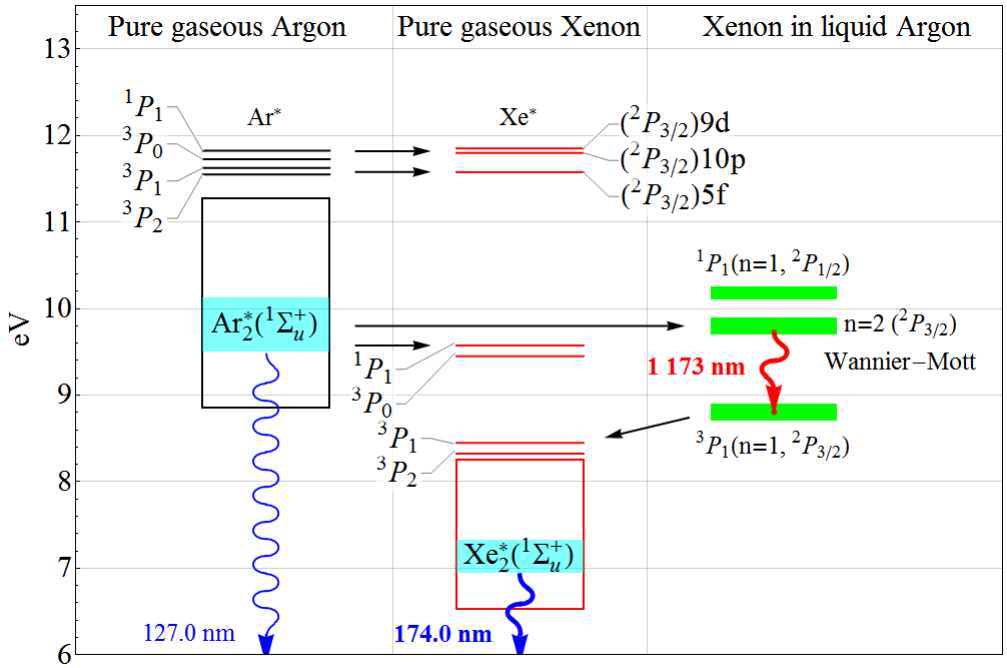


**Figure 1.5:** Excitation scheme with relevant energy levels in the liquid $Ar$-$Xe$ mixture compared to pure $Ar$ and pure $Xe$. The left column shows the singlet and the triplet states of the excited $Ar^*$ and the broad level band of the argon-excimer molecule $Ar_2^*\left(^1\Sigma_u^+\right)$. In contrast to the emission lines the broad emission of the excimer is represented by a rectangle containing a cyan-highlighted region, the full width at half maximum (FWHM) for this emission. The same representation is chosen for the pure gaseous $Xe$ (red, middle column). Additionally, doublet states participating in transitions from the $Ar$ singlet and triplet states are drawn. The right column presents perturbed states of $Xe$ (green). These states have been observed by B. Raz et al. [68]. The wavy blue and red arrows show the optical transitions of the observed wavelengths, the VUV transitions going all the way down to the ground states. This drawing is based on Fig. 4 in [67].

The excitation of pure argon is well known in the gas phase [56] and a direct excitation of $Xe$ can be neglected due to its low concentration. The corresponding[5] emissions in the liquid phase can still be seen for low $Xe$ contents [69, 51]. The energy levels presented here, exist solely in the liquid mixture: a perturbed $Xe$ $^3P_1$ ($n = 1$, $^2P_{3/2}$) state and a $n = 2$ ($^2P_{3/2}$) Wannier-Mott state [68], respectively. The energy gap between those states can explain the origin of the NIR emission and also the behavior with varying $Xe$ content (compare [70, Fig. 7]). For more details see [67].

## 1.5 Novel Particle Detector Concept

The detector concept investigated in this thesis is based on the emissions of the $Ar$-$Xe$ mixture, the previously known VUV emission and the newly found NIR emission. If these scintillations are behaving particle dependent in relation to each other, a new detector type can be promoted.

### 1.5.1 Two-Phase Time Projection Chamber & Single Phase Detector

Presently a modern kind of detector is the 2-phase time-projection chamber (TPC). These chambers, containing a large volume of liquid target material and a small volume of gaseous target material on top, work as follows: An incoming particle leads to excitation and ionization of the liquid target medium. The high electric field applied to the usually cylindrical chambers provides a charge separation. The first signal is the prompt light from the excitation detected by photomultipliers surrounding the liquid phase. The charges are separated by the electric fields whereby the electrons are drifting and hitting the phase boundary to the gaseous phase on the very upper part of the detector chamber. This is where the second signal, the ionization signal, is produced and again detected by photomultipliers on top of the detector volume. From these two signals valuable information[6] can be gained for discrimination of the incident particle. The problem comes with upsizing such detectors for getting more events in the same time period while providing the same electric fields for the ionization signal. Upsizing such detectors is a challenge due to the increase of the high voltages, reaching technical limits at the end [21, 10].

[5] There is a small shift in the wavelengths of a few nanometers at the transition to the liquid phase.

[6] Usually the relation of the prompt and the second signal is used for that purpose.

Another approach are single-phase detectors which use the different decay times[7] and intensities, for example of the liquid $Ar_2^*$ singlet and triplet excimer emissions that lead to different pulse shapes for different excitation particles [74]. If a pulse shape analysis is applied, the singlet-to-triplet ratio can be identified and serve for particle discrimination.

### 1.5.2 New Detector Concept

Alternatively to those mentioned above and other known particle detector concepts the liquid $Ar$-$Xe$ mixture offers the possibility to investigate the intensity ratios between the NIR and the VUV emissions and their ability for particle discrimination. In contrast to the pure-rare-gas detector the $Ar$-$Xe$ mixture could offer the possibility to do discrimination without pulse-shape analysis. Another advantage is the intrinsic shift from the $127\,nm$ $Ar_2^*$ to the $174\,nm$ $Xe_2^*$ of the excimer emission. This can be helpful by avoiding a wavelength shifter. Nevertheless, the use of quartz windows for the UV-light detectors would be necessary.

## 1.6 Proof of Principle of Particle Discrimination

The goal of this thesis is to study whether the newly found NIR emission in combination with the VUV light is suitable for a new kind of particle detectors. It is not an experiment to emulate a later detector situation in its entirety. For example the energies used are much higher than the expected recoil energies of WIMP-scattered particles of several $keV$. The experiment is performed to investigate the dependence of the light emission on different kinds of incident particles. This shall not be done by the detection of rare events by several distributed PMTs, but by the use of two specified PMTs, for the NIR and the VUV, respectively, and a large amount of fairly distributed single events. These single events are generated by continuous particle accelerator beams of different ions and energies. The use of a continuous beam instead of a pulsed-mode operation is primarily due to the statistics that can be gained within the limited measurement periods. Data acquisition using a pulsed beam would need significantly larger exposure times not only since the number of events per time is smaller, but also since the solid angles of the PMTs in the experimental setup is to small (compare chapter 2, figure 2.2 and table 2.1).

[7] Between $4.4\,ns$ to $6\,ns$ for the singlet and $1.1\,\mu s$ to $1.7\,\mu s$ for the triplet [71, 72, 73].

### 1.6.1 Separation of Particle Tracks

Using a particle accelerator in continuous-beam mode the question arises whether the observed scintillation light could be originating from overlapping particle tracks. This would be counter-productive to understand the light generating process because the basic idea is to consider single particles through the detector medium, i. e. the $Ar$-$Xe$ mixture. By hitting an argon atom – the most probable case using a volumetric fraction of $10^{-5}$ of $Xe$ – the projectile can generate secondary electrons by recoil, which in turn can excite other atoms of the detector material perpendicular to the ion path, forming a track in the liquid mixture. In comparison to the primary particle the range of the secondary electrons is strongly limited as discussed later in 3.1.1. As long as the paths of the secondary electrons from two different primary particles do not reach each other, the tracks of these particles can be called single particle tracks.

Going to higher ion-beam currents an interference between different particle tracks could be a major drawback, since an accelerator beam always consists of many ions parallel to each other. Therefore, a rough estimate was made regarding an upper limit for a single particle track diameter and the amount of particle tracks per unit area and time. To calculate these values a maximum electrical beam current $I_{ion}$ has to be set to get the particle current $\Phi_{ion}$ using the ion charge $Q_{ion}$:

$$\Phi_{ion} = \frac{I_{ion}}{Q_{ion}} \tag{1.1}$$

The next step is to assume that this particle current $\Phi_{ion}$ is flowing completely[8] through the smallest aperture used ($A_{apert} = (0.25\,mm)^2\,\pi$, compare 2.3.4) and taking an upper limit for a particle track to be present. This can be done by using the decay time of the time structure of the light emission [53] and setting a time threshold after which the particle track disappears. Five times the decay time leads to less than 1 % of the initial light emission and to a value of $\tau = 2\,\mu s$. The product of $\Phi_{ion}$ and $\tau$ can be seen as the number of tracks present in the liquid mixture at the same time. The average available area $\overline{A_{track}}$ for each particle track is then be derived by:

$$\overline{A_{track}} = \frac{A_{apert}}{\Phi_{ion}\tau} \tag{1.2}$$

[8] This is a generous assumption considering the reason why the apertures where installed: To cut off the parts of the beam usually hitting the walls. Typical beams of the tandem accelerator used are several millimeters in diameter.

From there a track radius can simply be calculated by assuming straight cylindrical tracks[9].

This average available track radius has to be compared with an estimate for maximum track dimensions. This is possible by using two formulas. The first one for the maximum energy $E_e^{max}$, the classical kinematic value that can be transferred from an ion with velocity $\beta_{ion} = \frac{v}{c_0}$ to a free electron [75, 76], which reads as follows:

$$E_e^{max} = \frac{2m_e c_0^2 \beta_{ion}^2}{1 - \beta_{ion}^2} \tag{1.3}$$

The ansatz for the relativistic energy $\frac{m_0 c_0^2}{\sqrt{1-\beta^2}} = m_0 c_0^2 + E_{kin}$ provides the relation of the ion energy per nuclei $^{E}/_{m}$ to $\beta$:

$$\beta = \sqrt{1 - \frac{1}{\left(\frac{E/m}{c_0^2} + 1\right)^2}} \tag{1.4}$$

The second one is an empirical formula taken from [77, 78] for the distance of the maximum energy deposition for electrons $r_e^{E_{max}}$ with energies in the range of about $10\,keV$:

$$r_e^{E_{max}} = 1.613 \cdot 10^{-8} m \cdot \left(\frac{E_e^{max}}{keV}\right)^{1.75} \tag{1.5}$$

The empirical numerical factor in this equation is adapted to the use of liquid $Ar$ in these experiments by scaling via the known densities (compare table A.1).

Both formulas (1.3) and (1.5) are monotonously increasing with electron energy and ion velocity[10], respectively. For the experimenter these formulas set limits to the ion beam currents for different ions and energies. The result of these calculations is shown in table 3.2 in subsection 3.1.1. It reveals that the **allowed** ion beam current is at least 11 times higher than the **actual** ion beam current used in the experiment.

As a result, the scintillation light detected can be assumed to come from many single particle tracks that are either spatially or temporally separated.

[9] Generally, the tracks are neither straight nor cylindrical. But the increase in angular straggling by the decelerating particle is accompanied by a reduced range of the secondary electrons.

[10] Ion velocities from $0.04 \cdot c_0$ to $0.20 \cdot c_0$ are covered by this experiment.

### 1.6.2 Energy Deposition Range

While equation (1.5) offers a possibility to estimate the **maximum range** of secondary electrons of a known energy, the calculation of a core radius of the particle track for the **energy deposition** due to these electrons is of particular interest. As it was shown by Waligorski et al. [79] a dose can be calculated for every cylindrical shell with thickness $dr$ at a distance $r$ from an ion path in a liquid. For a certain fraction of energy deposition this empirical formula can be used to derive a simple equation for the radius in dependence of the projectile's $E/m$-value. This is done by calculating the dose, i. e. the energy deposition, versus the radius for different velocities $\beta$ (see equation (1.4)) and projectiles and fitting the values for a fixed percentage of energy. Thus, the following equation results for 66 % of energy deposition within the cylindrical shell [80, 81]:

$$r_{E_{depo}} = 4.88\,nm \cdot \left(\frac{E/m}{MeV/u}\right)^{0.52} \tag{1.6}$$

The length factor had been scaled from liquid water to liquid argon by the densities.

An advantage of this equation is that the energy distribution of secondary electrons is already included in the empirical formula of Waligorski et al. Equation (1.6) will be important later on to calculate transverse dimensions of the heavy ion tracks and to estimate the energy deposition per atom.

### 1.6.3 Method: Various Projectiles from a Particle Accelerator

For demonstrating the feasibility of a particle discrimination by measuring the NIR-to-VUV ratio an adaptable and powerful tool is needed. The purpose is to test the emissions for many different particles with various energies with good statistics, reliability, and – what is most important – using the same setup to prevent unpredictable systematic errors.

A linear particle accelerator is seen as such a tool. While it offers the possibility to choose between a wide range of stable isotopes it is also capable of varying the beam current over several orders of magnitude. Besides that the experimenter is able to choose between a pulsed and a continuous operation mode.

While an experiment with a pulsed beam would be feasible and allow time-resolved measurements, the continuous beam operation has been chosen. This is due to the fact that a pulsed operation mode would require a complete single event analysis for each pulse and furthermore the light detection would be much more difficult for the given solid angles and a single set of light detectors. The continuous operation mode on the other hand has several advantages. It can be seen as non-separated pulses

for which the large particle current (i. e. an event rate) compared to a real dark matter experiment allows not only good statistics in a reasonable amount of time but also leading to an excellent signal-to-noise ratio by dominating the usual background particles by number, still using a tiny experimental cell. At the same time the detected light signals are just multiplied with respect to a single event, as long as each event triggers the same energy transfer processes.

Here the NIR and VUV emissions were not planned to be analyzed with spectral resolution. The only distinction made is between the infrared and the ultraviolet range[11] to generate two signals. Since the emission spectra are known (figure 1.3 subsection 1.4.1), the goal is to achieve a fast and reliable analysis of the two emission features by looking at the ratio of their signals and its dependence on the incident particles.

[11]The separation of IR and UV light is possible without any further experimental effort since detectors with non-overlapping wavelength sensitivities can be used. For details see subsection 2.3.1.

# Chapter 2

# Experimental Setup

The concept of this experiment (see subsection 1.5.2) is to excite liquid $Ar$ with a volumetric fraction of $10^{-5}$ of $Xe$ to generate two distinct scintillation signals, in the near-infrared (NIR) and in the vacuum-ultraviolet (VUV) wavelength range, respectively. The excitation is in such a way that single ion tracks do not overlap, so that only the basic processes are leading to the emissions. The operation of the photomultiplier tubes (PMT) in photon-counting mode in conjunction with a continuous ion beam current from the tandem accelerator make it possible to reach very good statistics in short time.

This chapter describes the technical aspects of the experimental setup, including the handling of the rare gases, the photomultipliers, and the data acquisition. The rare gases have to be mixed and impurities have to be removed. The rare gas mixture has to be kept at a constant temperature in the liquid phase while the purification continues and the mixing ratio has to be kept stable. The photomultipliers have to have an equal view on the excited volume with an optimal solid angle, depending on the possibilities given by the experimental setup. The PMTs have to be calibrated using a stable external light source. The position and the intensity of the particle beam have to be optimized concerning the target cell entrance and the volume behind the entrance foil. In addition, the position of the light emission in beam direction has to be considered with respect to the field of view of the PMTs. At last the data acquisition according to the operation modes is described.

## 2.1 Overview of the Experimental Setup

The target cell containing the liquid $Ar$-$Xe$ mixture is at the center of the experimental setup. A scheme of the target cell can be seen in figure 2.1. The ion beam

from the particle accelerator enters the target cell from the beam line vacuum via a titanium entrance foil and the light of the emission spectrum (compare subsection 1.4.1) can leave the cell through a $MgF_2$ window. The $Ti$ entrance foil for the projectiles could have been arranged perpendicularly to the particle beam but this would lead to an obstruction of the light paths to the PMTs. Thus, the foil was tilted towards the PMTs. An angle of 45° would be optimal if the $Ti$ foil would be rigid. However, due to deformation induced by the pressure difference between the target cell and the surrounding vacuum, an angle of 48.6° was chosen. The bulk of the cell is built from copper to assure good heat conductivity for cooling, with the exceptions of the entrance foil holder (stainless steel) and the Faraday plate (tantalum). The Faraday plate at the end of the cell allows for beam current test measurements when the cell is evacuated. For filling the cell and for circulation of the rare gas mixture the cell has two copper tubes for connection to the gas system. The target cell was already used successfully by M. Hofmann for his ion beam experiments using pure liquid $Ar$ [82, 74].

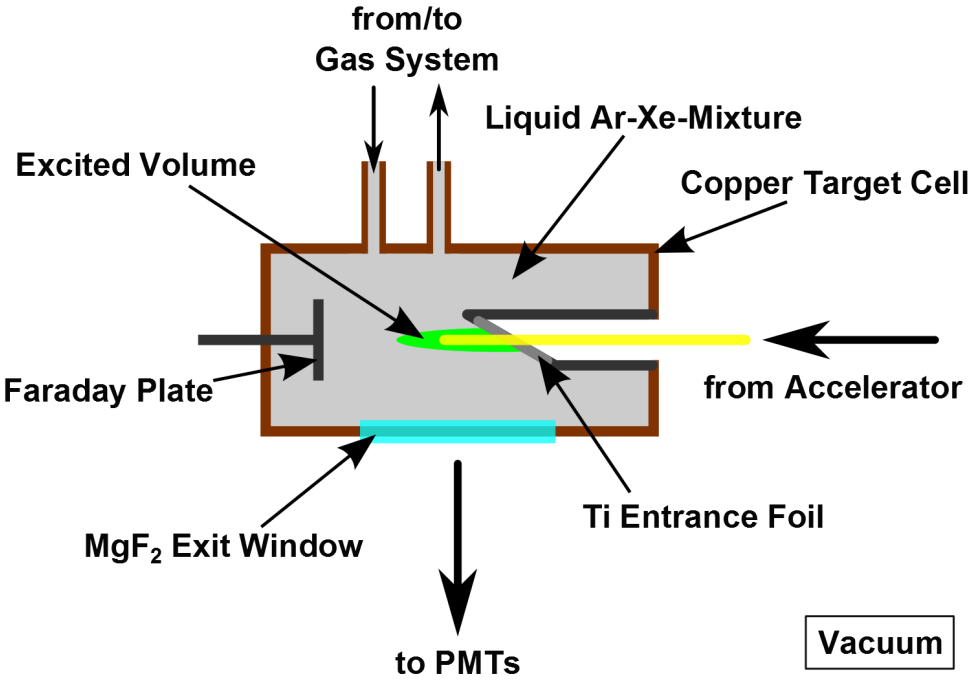


**Figure 2.1:** The target cell in the center of the experimental setup contains the liquid $Ar$-$Xe$ mixture (gray) with a part of it excited (green) by a particle beam (yellow). The light emitted by the excited volume exits the cell through a $MgF_2$ window towards the PMTs. The cell is connected to the gas system via two copper tubes.

For the main experiments the Tandem van de Graaff Accelerator of the Maier-Leibnitz-Laboratorium (MLL) at the research center in Garching near Munich was used. It is a linear accelerator, capable of acceleration voltages between 6 and 14 $MV$, however this upper limit was not used in this experiment due to stability reasons.

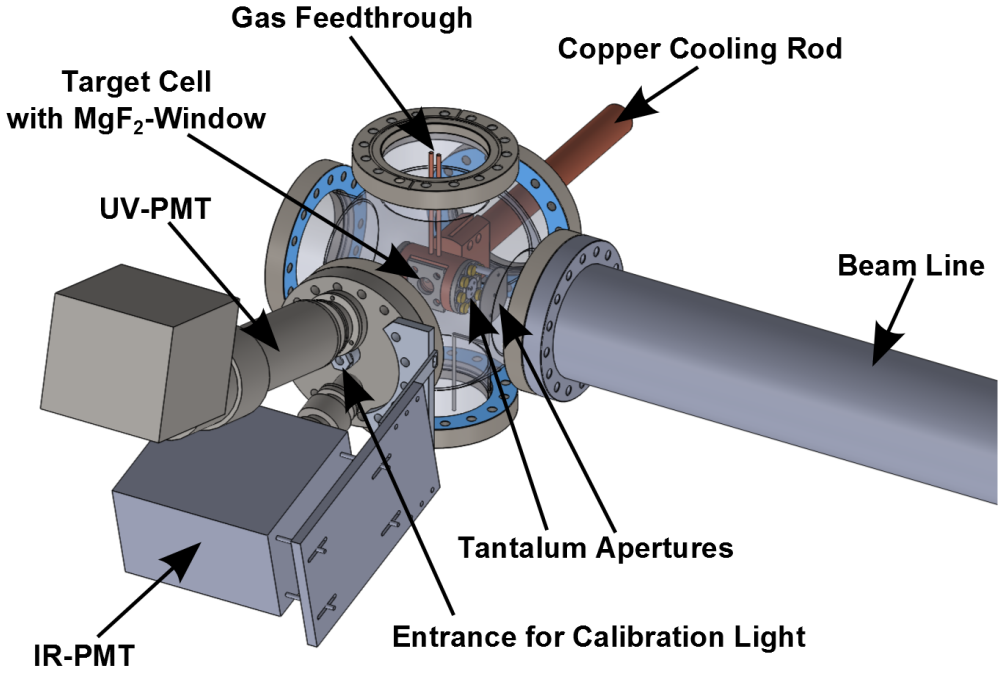


**Figure 2.2:** CAD drawing of the beam line setup showing the vacuum chamber (transparent) and its surrounding. The target cell is in the center of this chamber, attached to the copper cooling rod leading to a liquid nitrogen tank (not shown) on the outside. The cell also has two tubes for the connection to the gas system and a $MgF_2$-window for the scintillation light. The light is detected by the photomultipliers (PMTs) on the left side, perpendicular to the beam direction. Between the PMTs is a shutter with an entrance for the light from a calibration setup. Before the ion beam enters the target cell, it passes through a number of different tantalum apertures to prevent it from hitting other parts of the cell or the vacuum chamber. Cables, isolation, and end flanges are not shown in this drawing.

In figure 2.2 the experimental setup at the beam line target station is depicted. The target cell containing the liquid $Ar$-$Xe$ mixture is surrounded by a vacuum chamber. Not shown in the drawing are a tank for liquid nitrogen cooling, the gas system for mixing and purifying, the data acquisition for the readout of the photomultiplier tubes (PMTs), as well as their electronics, and the calibration setup. Most

components are controlled manually for highest flexibility of the experiments.

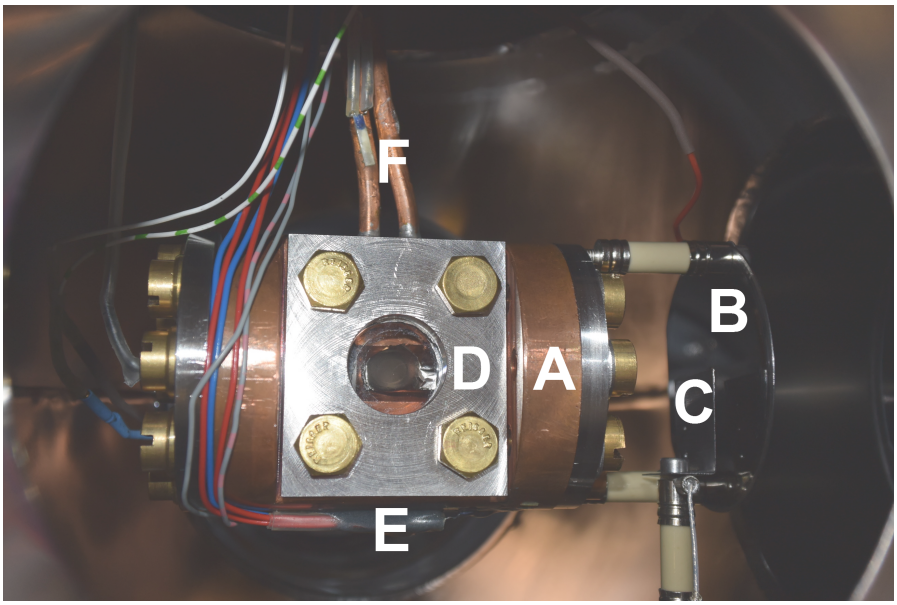


**Figure 2.3:** In this photograph the target cell (A) is shown, mounted inside the vacuum chamber with the viewing direction of the PMTs, beam line to the right. At the beam side two of the tantalum apertures and their mounting can be seen: A disk with an aperture of 3 $mm$ (B) and the rectangular movable aperture (C) with three different hole sizes. Both apertures are isolated against the copper target cell and connected to electrical ports on the outside of the vacuum chamber. On the side of the target cell is a metal plate (D) attached by four screws holding the $MgF_2$-window. Behind this window the titanium entrance foil in the very center of the cell is visible. This foil is tilted towards the PMTs for an enhanced view of the light emission in the liquid $Ar$-$Xe$ mixture. The cables on the left are connecting a heating resistor (E), a Pt100 sensor, and a Faraday cup at the end of the target cell. The tubing (F) atop the copper cell links it with the gas system on the outside. All components of the target cell are indium sealed and the thermal expansion of different metals was taken into account.

The photograph in figure 2.3 shows the target cell (as described in figure 2.1) within the vacuum chamber. The cell itself was already used in a very similar setup by M. Hofmann for his work with pure liquid $Ar$ [74]. It has a volume of 5.6 $cm^3$ for the liquid mixture, which is circulated through the cell via the gas feedthrough from above. An important technical detail is the orientation of the $Ti$ entrance foil. As already mentioned it is inclined towards the $MgF_2$-window to improve the visibility of the light emission for the PMTs. The angle for this inclination takes into account the diameter of the window and the bulge of the foil due to pressure differences.

## 2.2 Preparation of the Rare Gas Mixture

The gas system (figure 2.4) serves the following tasks: Providing a framework for filling the target cell, measuring the gas pressure, as well as circulating and purifying the mixture even when the experiment is running.

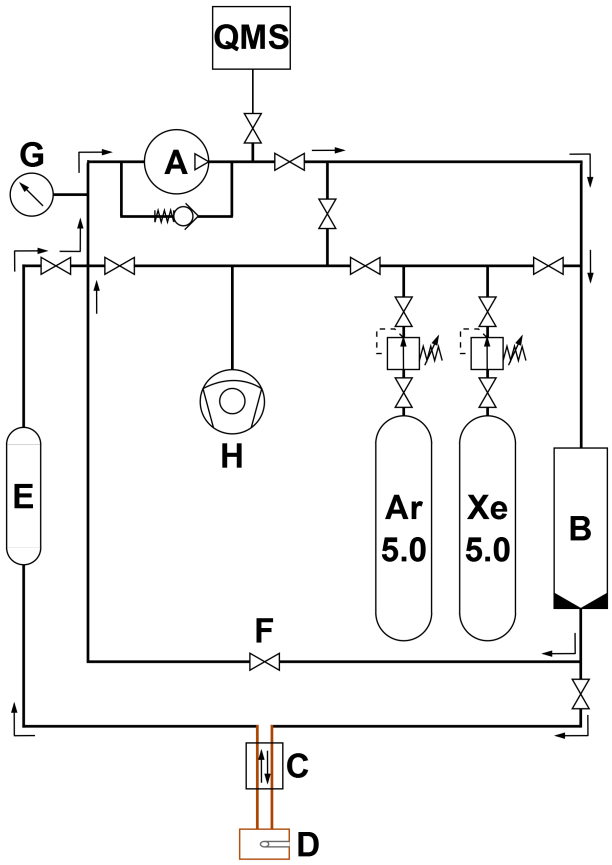


**Figure 2.4:** Schematic drawing of the gas system. The gas flow through the system during the experiment is indicated by arrows, starting at a metal bellows pump (A) and leading through a rare gas purifier (B), a heat exchanger (C), the target cell (D), and a buffer volume (E). Parallel to the experimental line is a bypass valve (F) to reduce the gas flow through the cell. Pressure is measured using a high precision pressure sensor (G). For evacuating a vacuum pumping station (H) is mounted. For a test experiment a quadrupole mass spectrometer (QMS) was connected temporarily.

During the experiment the rare gas mixture is circulated by a metal bellows pump (Senior Operations, Inc. Metal Bellows MB41E, bypassed by a spring-loaded check valve

to avoid damage). In a first stage all impurities (hydrocarbons, nitrogen, etc.) are removed from the mixture by a rare gas purifier (Monotorr PS4-MT3-R-2). After passing a heat exchanger the mixture is entering the target cell where it condenses. The re-evaporated gas passes the buffer volume ($\varnothing 100\,mm$ vacuum tube with $9\,dm^3$ volume) before returning to the circulation pump again. Because of the high gas flow a part of the mixture has to go through the bypass valve to allow condensation in the cell. When the circulation pump is shut off the pressure within the gas system can be measured using a high precision pressure sensor (MKS Baratron Type 390H-01000 with MKS Type 270 Signal Conditioner). This sensor is used to control the filling. Prior to that the gas system is evacuated by a vacuum pumping station (Pfeiffer Vacuum HiCube 80 Eco). In an early stage test experiment a temporarily attached quadrupole mass spectrometer (QMS) was used to investigate potential changes in the mixture. The result is described in the following subsection.

### 2.2.1 Gas Mixing

**Mixing Ratios** As in previous studies, like in the work by A. Neumeier [54], all specifications of the mixing ratio of $Xe$ in liquid $Ar$ refer to partial pressures[1] in the gas phase. This is due to the fact, that an exact determination of the true mixing ratio in the liquid is not easy to perform and a rough calculation (similar to [54, subsection 3.2, page 44]) concerning the worst case, i. e. condensing of all $Xe$ from the whole gas system in the cryogenic cell, leads to a maximum increase in the amount of $Xe$ by a factor of $\sim 3.4$. On the other hand the $Xe$ could theoretically freeze out to the walls of the cell, which would lead to a lower $Xe$ concentration in the liquid. However, both possibilities were already investigated by O. Cheshnovsky et al. revealing an enrichment factor of less than $\sim 2$ [69].

This implies that the volume fraction of $Xe$ in the gas and liquid phases can be assumed to be near the intended value of $\sim 10^{-5}$. Furthermore, the gas mixture in these experiments with different ion beams was not changed nor were the settings of the gas system, i. e. the pressure in the system above the liquid, the temperature given by a Pt100 sensor, and the configuration of the valves during the purification (see subsection 2.2.2). Therefore, the results are comparable among each other.

The filling of the target cell and the whole gas system was done in several steps to reach the wanted small fraction by volume of $10^{-5}$ of $Xe$ in $Ar$. As the gas system can contain approximately $10\,dm^3$ and starts at $1.3\,bar$ with a gas-filled cell, it also includes a buffer volume of $9\,dm^3$ to keep a sufficient rest pressure.

[1] For ideal gases the partial pressures are equal to the mole fractions and the volumetric fractions, respectively.

If the pressure above the liquid phase would drop below the triple point pressure[2] $p_{triple} = 0.687\,bar$, the valid kind of phase transition would be desublimation instead of condensation as the liquid phase does not exist under those conditions. Thus the target cell could not be filled with liquid any more. The necessary buffer volume was calculated using the known density of liquid $Ar$ of $1.4\,{}^{g}/_{cm^3}$ and the volume of the target cell of $5.6\,cm^3$.

Although a direct mixing of a volumetric fraction of $10^{-6}$ would be possible by the high precision pressure sensor in use, the mixture was prepared in several steps. A mixing procedure starts with evacuating the whole piping, including the target cell, buffer volume, and the rare gas purifier until an acceptable[3] vacuum is reached at the vacuum pump. In a second step, for a volumetric fraction of $10^{-2}$ of $Xe$ in $Ar$ , $13.000\,mbar$ $Xe$ are fed to the gas system. The difference to $1.3000\,bar$ is then filled up with $Ar$. After a sufficient time[4] of mixing using the metal bellows pump and purifying by the rare gas purifier in the gas system, an evacuation down to $1.300\,mbar$ follows. The $Ar$-$Xe$ mixture with a fraction by volume of $10^{-2}$ of $Xe$ is refilled with $Ar$ up to $1\,300.0\,mbar$ again and thereby diluted by a factor of 1 000. This leads to a final volumetric fraction of $10^{-5}$ of $Xe$, i. e. $10\,ppm$, which is – as already mentioned in subsection 1.4.1 – the mixing ratio with comparable scintillation intensities in the NIR and VUV.

**Long-Term Stability** For preparing the beam time a test of the stability of the mixing ratio was performed using a quadrupole mass spectrometer (QMS). For this test the gas system was operated in the same setting as during the beam time, including purification and liquefaction of the mixture. A very small part of the gas was continuously fed to the QMS through a capillary[5] that is attached to the gas system behind the circulation pump (compare figure 2.4).

[2] For simplicity and due to the small $Xe$ content the triple point of $Ar$ is used here.

[3] $< 10^{-5} mbar$

[4] Once, while the partial pressures were monitored with a quadrupole mass spectrometer, a mixing time of 10 to 15 $min$ for this specific gas system could be found.

[5] The capillary had an inner diameter of $50\,\mu m$ and a length of about $1\,m$.

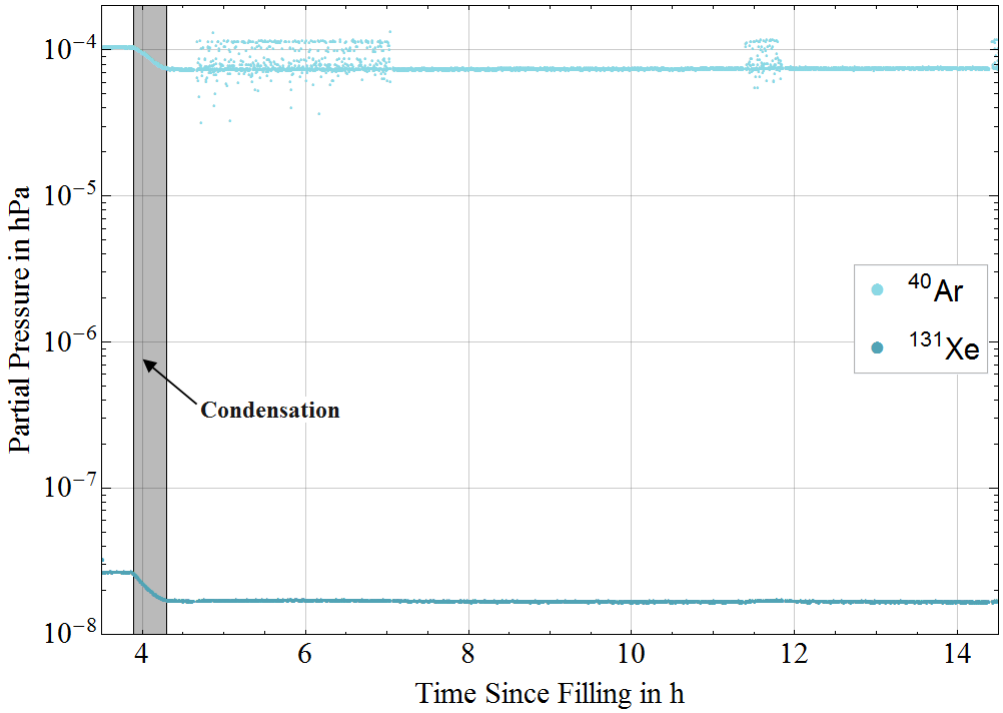


**Figure 2.5:** Partial pressures of $^{40}Ar$ and $^{131}Xe$, as measured with a quadrupole mass spectrometer (QMS) during the stability test, plotted against time. Recording was started with the filling of the gas system ($t = 0$), but data is only shown here from the beginning of the condensation in the target cell. After the condensation no significant changes in the partial pressures and, therefore, in the pressure ratios for a measurement time of about $10\,h$ could be detected. For several time periods distortions in the $Ar$ line can be seen. These distortions can be attributed to electronic disturbances of the QMS, but they do not affect the overall measurement.

As seen in figure 2.5 no change in the partial pressures over a time of $10\,h$ was visible. As no additional pressure regulation was installed for the mass spectrometer a change in overall pressure due to temperature change and liquefying also led to a change in the partial pressure signals. Therefore, the data of the mass spectrometer has to be interpreted taking this overall pressure changes into account. No data was recorded with the mass spectrometer during the beam time, but the measurement procedure was designed in a way to take into account concerns of significant accumulation of $Xe$ on walls or gaskets or separation of the mixture by aggregation of $Xe$ to clusters (see subsection 3.2).

It is also worth mentioning that the uncorrected partial pressures of two selected isotopes shown here are not sufficient for a direct measurement of the **absolute** $Xe$ amount. This is due to the fact that on the one hand $Xe$ has more stable

isotopes than $Ar$ and not all of them are measured here, and on the other hand $Xe$ is easier to ionize, leading to a larger signal for the QMS. Also double ionization of $Xe$ and crosstalk for different species had been observed. Finally it has to be noted that an increase of $Xe$ in the liquid phase would lead to a decreased value in the QMS measurement, since the gas phase is probed. Despite those measurement characteristics, a variation in the mixing ratio that would have led to a variation in the signals could not be detected.

A recent study by D. Akimov et al. shows an investigation of time spectra of the singlet and triplet emissions of two different $Xe$ admixtures in the discussed mixing ratio region. It includes also a long-term run for a period of $31\,h$. As a result they published the absence of significant changes[6] in the time spectra for volumetric fractions of $1.4 \cdot 10^{-5}$ and $2.4 \cdot 10^{-5}$ of $Xe$ in liquid $Ar$ for a $31\,h$ test run [83]. The beam time measurements of our experiment took 3 days. But the gas mixture was repeatedly vaporized and heated up to room temperature again on a daily basis, to ensure a remixing and that water vapor cannot cover the $MgF_2$-window completely[7].

Changes due to the implantation of the ions shot into the target cell can be ruled out simply by calculating the amount of material injected by the ion beam. Considering the maximum of all particle currents, the overall implantation time and a number of 25 individual measurements a total amount of $1.6 \cdot 10^{-11} mol$ of beam-implanted impurities compared to $5.3 \cdot 10^{-6} mol$ of $Xe$ in the gas system is derived. Therefore, and also taking the continuous circulation into account, implantation is not an issue.

### 2.2.2 Gas Purification

The purity of the scintillation gases is crucial, as any tiny content of impurities can alter the scintillation spectrum [71]. For proper purification the mixture was constantly circulated through a rare gas purifier (Monotorr PS4-MT3-R-2) from the beginning of mixing until the end of the experiment. The purifier is able to remove all impurities except rare gases by irreversible chemical bonding. Regarding other rare gases than $Ar$ (Westfalen $Ar$ 5.0) and $Xe$ (Linde $Xe$ 5.3), $Kr$ is mentioned by the manufacturer as a possible impurity of the delivered $Xe$ gas with a volumetric fraction $\leq 10^{-6}$, i. e. a possible volumetric fraction of $\leq 10^{-11}$ of $Kr$ in the final mixture.

[6] They measured a deviation of 1.3 % which they attribute to a PMT drift.

[7] For details of the fogging effect see 3.3.3.

### 2.2.3 Cooling & Condensing

The $Ar$-$Xe$ mixture was liquefied using liquid nitrogen for reaching cryogenic temperatures. To ensure a good heat conduction, most components of the target cell are made from copper and the cell was connected to a nitrogen reservoir via a copper rod. This rod holds and aligns the target cell inside the vacuum chamber (compare figure 2.2). For the alignment relative to the ion beam axis the displacement of the cell caused by the thermal expansion of copper was taken into account.

As mentioned in 2.2.2, the mixture was continuously circulated and purified. Only in the small volume of the cell the gas was kept liquid during the experiments. The temperature of the cell and gas pressure in the gas system are the relevant parameters for monitoring the status of the mixture. The buffer volume was installed to keep the pressure drop in the gas system within acceptable limits: While starting at $1.3\,bar$ a pressure of about $0.9\,bar$ was reached for the target cell filled with the liquid at a cell temperature of $90\,K$. These values were figured out using an inspection window instead of the photomultiplier tubes for the first cooling[8].

## 2.3 Handling of the Photomultiplier Tubes

The IR- and the UV-PMTs are operated in parallel in the photon counting mode for a fixed period of time to collect an appropriate number of counts: Enough counts to reach good statistics, but not too many to stay in the linear response regime. Beam current and measurement time are the adjustable parameters to ensure this.

The experimental setup in this thesis is not yet a detector prototype of the new kind but rather a proof-of-principle setup. Thus, e. g. position reconstruction is not performed here. Furthermore, the two photomultiplier tubes for the detection of light have to be positioned for an optimal utilization of the dynamic signal range. The continuous beam operation with relatively high particle currents of the accelerator and the absence of a monochromator for spectral resolution make it easy to collect enough light, i. e. to obtain enough pulses within a short time. A preferably large solid angle was ensured by mounting the PMTs as close as possible to the optical $MgF_2$-window of the target cell (values in table 2.1). The PMTs used are a Hamamatsu H10330B-45 SEL for the near-infrared and a Thorn EMI 9426 for the vacuum ultraviolet radiation. Both PMTs are mounted on a flange close to the

[8] There is only a narrow temperature range from $87.3\,K$ to $83.9\,K$ between condensing and freezing $Ar$ at standard pressure ($1013.25\,mbar$).

$MgF_2$ window on the left side of the target cell, with respect to the beam direction. The optical axes of both PMTs are tilted upwards and downwards, respectively, by 14° each, see figure 2.2.

### 2.3.1 Specifications

The IR-PMT is the same that was used to measure the NIR emission feature in the experiments by Neumeier et al. [53]. In contrast to the former studies no monochromator was used for spectral resolution in the present work. The wavelength range was only cut off at the lower edge by a transmission filter[9]. Thus, the observed wavelength range in the near infrared reaches from 1076 to 1400 $nm$. The NIR emission feature aimed at is at $(1173 \pm 99)$ $nm$ [53]. At this point it is worth mentioning that the IR-PMT is a selected one (compare "SEL" in the type designation, table 2.1) with an outstanding quantum efficiency for this wavelength region of up to 9.6%. To enhance the solid angle a collimation lens is used to focus the light onto the 1.6 $mm$ diameter cathode. In this way an effective light detection area of 18 $mm$ diameter is obtained.

The UV-PMT is equipped with a $MgF_2$-window for VUV measurements. The light path from the $MgF_2$-window of the target cell to the UV-PMT is evacuated for the detection of the VUV light emitted at $(127.0 \pm 7.4)$ $nm$ and at $(174.0 \pm 8.6)$ $nm$. In contrast to the IR-PMT, the UV-PMT range was not constrained in its spectral response. So the detectable range reaches from 110 to 630 $nm$, i. e. it includes part of the visible range.

Table 2.1 gives an overview of several specifications of both PMTs. The diagram in figure 2.6 illustrates the missing overlap of the PMT responsivities. Due to this gap, the IR and the UV values can be acquired independently. The flat regions of maximum efficiency are also important for the measurement concept: As long as wavelength shifts[10] within one of the wavelength regions stay within the flat maxima, the scintillation ratios are only influenced by the ratio of the IR and the UV emissions.

[9] LOT Quantum Design CH-E1070LP-25. Range from 1076 to 1500 $nm$ with transmission larger than 90%.

[10] For example from the $Ar_2^*$ $(127.0 \pm 7.4)$ $nm$ to the $Xe_2^*$ $(174.0 \pm 8.6)$ $nm$ emission.

| Manufacturer | Hamamatsu | Thorn EMI |
|---|---|---|
| Type | H10330B-45 SEL | 9426 |
| Spectral Response | 950 $nm$ to 1 400 $nm$ | 110 $nm$ to 630 $nm$ |
| Operating Voltage | $-760\,V$ | $-1.75\,kV$ |
| Maximal Quantum Efficiency | 9.6% | 26% |
| Effective Cathode Diameter | 18 $mm$ (focused onto 1.6 $mm$) | 25 $mm$ (cut out of 52 $mm$) |
| Effective Cathode Area | 2.5 $cm^2$ | 4.9 $cm^2$ |
| Effective Distance to Light Emission | 268 $mm$ | 194 $mm$ |
| Solid Angle | $4 \cdot 10^{-3} sr$ | $1.3 \cdot 10^{-2} sr$ |

**Table 2.1:** Specifications for both PMTs selected from the corresponding data sheets.

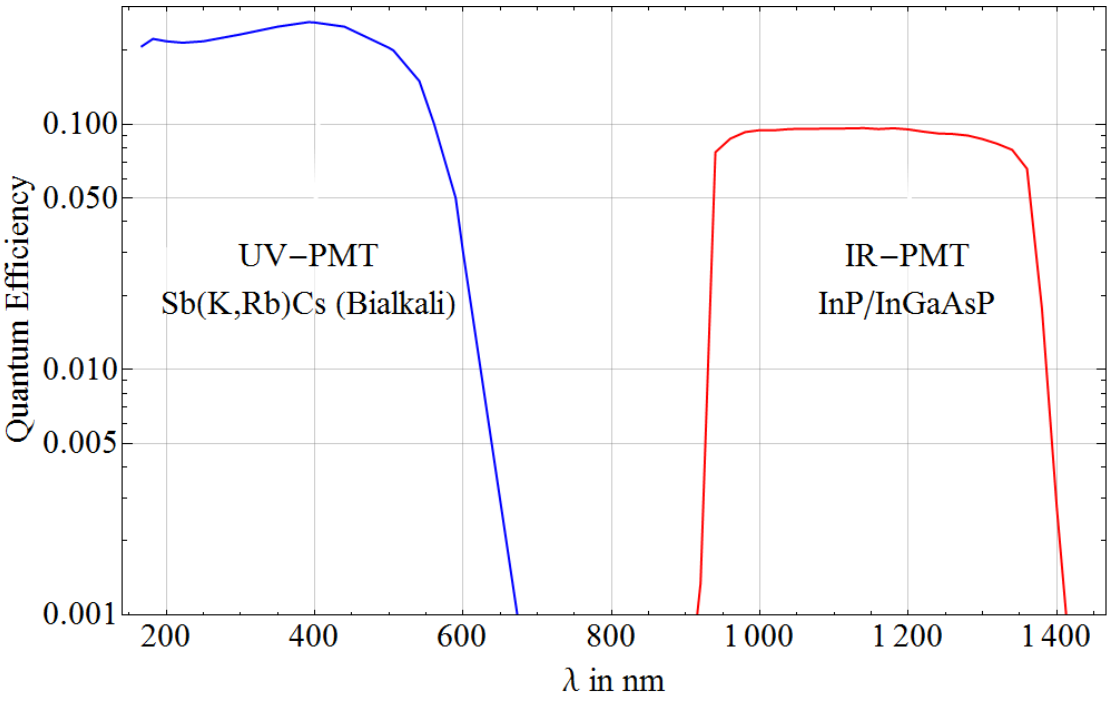


**Figure 2.6:** Sensitivity of the PMTs/photocathodes used. The diagram shows the quantum efficiencies on a logarithmic scale versus a linear wavelength axis. Note that these graphs are not taking any attenuation due to the setup into account (like fogging of windows, subsection 3.3.3). The data visualized in the curves is taken from [84, 85].

Since the vacuum gauge for the vacuum chamber surrounding the target cell is using hot-cathode ionization and thereby emitting visible and infrared light, it has to be switched off during PMT measurements.

### 2.3.2 Photon Counting Mode

Both photomultiplier tubes were used in photon counting mode. This sets a limit to the overall light flux, which has to be taken into account when choosing the beam current. The dead times to be considered to prevent the PMTs from running into a current mode operation are $8\,ns$ for the IR- and $25\,ns$ for the UV-PMT, respectively. The dead time given by the TTL pulse length of $80\,ns$ of the constant fraction discriminators (CFDs) is higher, allowing only count rates of maximal $12.5\,MHz$. However, the most restrictive factor is the highly sensitive IR-PMT with a restricted average output current of $1\,\mu A$. Depending on the selected gain[11] the maximum allowed count rate for the IR-PMT is about $2\,MHz$, corresponding to one single pulse per $500\,ns$. To keep the parameters in a save range, values in the experiment are kept an order of magnitude lower a maximal count rate of $200\,kHz$. Thus, the largest duty factor[12] for the (TTL-) pulses is equal to $1.6\,\%$. This restriction to the count rate could be easily met during the beam measurements since the ion beam current was already restricted to have well separated tracks (compare subsection 1.6.1).

Linearity in photon counting mode operation was proved using a LED calibration setup described in the next subsection.

### 2.3.3 PMT Sensitivity Calibration Method

The calibration of the PMTs regarding their sensitivity was performed using the attenuated light of LEDs in conjunction with photodiodes for crosschecking. Several integrating spheres are attenuating and evenly distributing the LED light before it is guided into the vacuum chamber to be detected by the PMTs.

Since several test runs showed drifts in the PMT sensitivities a suitable calibration method for the PMTs was required. As the ion beam from the accelerator runs in a continuous beam operation mode the calibration should also be done with continuous illumination by light. The calibration measurement should furthermore be possible during the beam time without changing the setup and lead to a comparable count rate at the PMTs.

[11] The final test sheet states a gain of $\approx 2.5 \cdot 10^6$ for a voltage of $-760\,V$ corresponding to a charge of $500\,fC$ per pulse [85].

[12] Pulse duration ($80\,ns$) divided by period duration ($10 \cdot 500\,ns$).

To achieve this goal, light from the LEDs[13] used for the sensitivity calibration had to be attenuated. Otherwise it would have been too intense for PMTs under normal operation. Therefore, three integrating spheres were coupled together. The LEDs are inserted in the first sphere and can be driven by their typical constant current. At the connection between the integrating spheres only a fraction of the light passes onto the next one. The last integrating sphere is coupled to the vacuum chamber with the PMTs via an optical fiber which is attached directly between the PMTs (figure 2.2, "Entrance for Calibration Light"). The adapter for the fiber contains a shutter that allows to keep the LEDs running at the chosen current values. In the vacuum chamber the test light is allowed to be spread and scattered onto the target cell and the walls of the chamber. The light emissions from both LEDs are monitored by photodiodes[14] within the spheres. The illumination by the LEDs was performed in a similar manner as the excitation of the $Ar$-$Xe$ mixture using the ion beam, regarding illumination time and intensity.

The linearity tests for the chosen thresholds of the CFDs are shown in figure 2.7. The different slopes are due to different sensitivities of the PMTs and photodiodes as well as a different flux of light from the LEDs to the photodiodes and PMTs.

While the LED illumination is carried out with a fixed setup during the beam time, the ions create light at different positions in the target cell due to different ranges for different ions and ion energies (compare table 3.1 in subsection 3.1.1). To rule out a potential position dependency in the light detection setup, calculations and a test experiment described in 2.3.6 were carried out.

### 2.3.4 Beam Handling

During the beam time measurements certain parameters should be kept constant and reproducible, respectively, while others had to be varied in a controlled manner.

The first requirement applies to the diameter and the angle of incidence of the ion beam. To achieve this, several apertures were added after the test runs (compare subsection 3.1.2) of the experiment. Two of them can be varied in size, a four-sector-aperture at the very beginning of the experiment and a movable pinhole aperture with different hole sizes[15] close to the beam entrance to the target cell. Optimal settings were also determined in the test runs.

[13] Thorlabs LED275W: $(275 \pm 5)\,nm$, FWHM $12\,nm$; Roithner LED1200: $(1200 \pm 50)\,nm$, FWHM $80\,nm$.

[14] Thorlabs GaP Photodiode FGAP71: $150\,nm$ to $550\,nm$; Thorlabs InGaAs Photodiode FGA10: $900\,nm$ to $1700\,nm$.

[15] Object C in figure 2.3. Aperture sizes: 0.5, 0.7, and $1.0\,mm$.

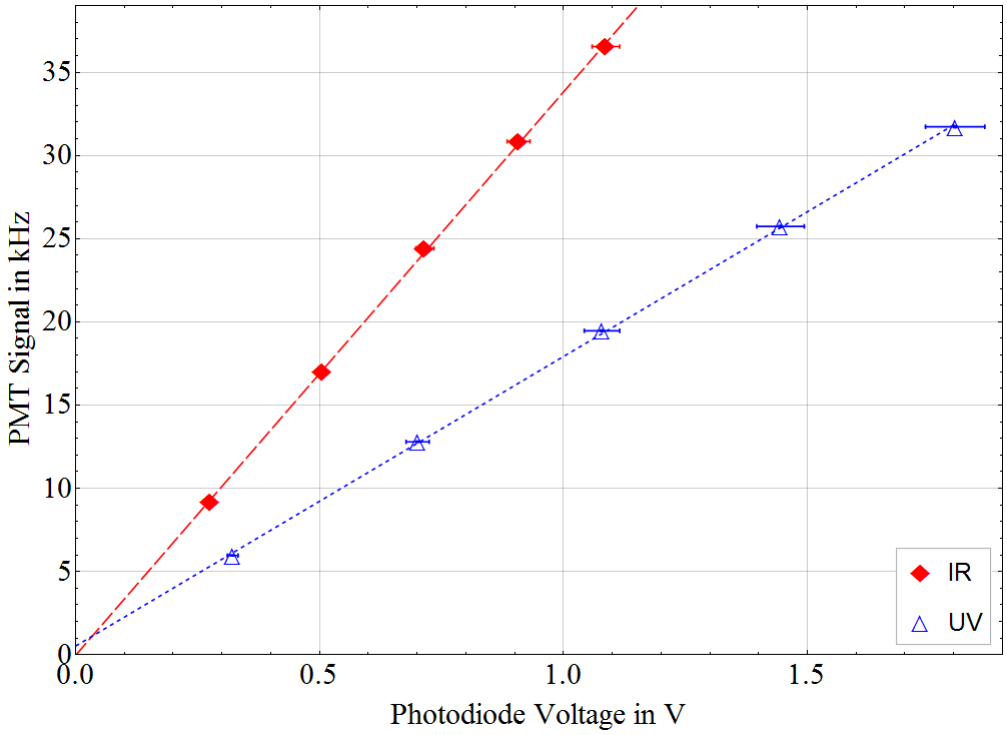


**Figure 2.7:** This diagram shows the results of the linearity tests for IR (red) and UV (blue) light. The signal of the PMTs is plotted versus the voltage of a photodiode circuit [86]. The lines are linear fits to the data points, the error bars of the PMT signals are smaller then the symbols. Both channels show a very good linear behavior.

The variable parameter of the ion beam is the ion beam current. For several particles and energies the experiment was repeated using similar as well as different beam currents.

To monitor the beam current at the end of the beam line a couple of apertures are electrically connected to current readouts. Also a Faraday cup is mounted for reference measurements in the beam line directly before the last apertures. The Faraday plate within the cell (compare figure 2.1) could only be used in the test runs as the target cell has to be evacuated. Otherwise gas or liquid in the cell alter the current measurement by ionization in the medium and stopping of the ion beam.

### 2.3.5 Entrance Foil

For entering the target medium in the cell the particle beam has to pass the entrance foil. It consists of titanium ($Ti$) with a thickness[16] of approximately $2.9\,\mu m$. The path for the ions is longer due to the tilting of the $Ti$ foil by 48.6°, resulting in approximately $4\,\mu m$. This $Ti$ foil is especially important for the calculations of energies and energy depositions, see subsection 3.1.1. This is due to the energy loss before reaching the liquid rare gas mixture. The titanium foil represents a possible x-ray source, too, and could, therefore, alter the PMT signals. Another issue regarding the entrance foil are potential surface effects between the $Ti$ and the $Ar$-$Xe$ mixture. To show that such effects, if they exist, are not significant, the penetration depths and the track radii for the different ions have to be considered. This is discussed in subsection 3.1.1.

### 2.3.6 Position of the Light Emission

The range of the ions in the liquid rare gas target varies over several orders of magnitude, see table 3.1. To account for this fact and to show that this has only negligible influence on the light detection efficiency the following test experiment was performed.

In figure 2.8 a substitute for the entrance foil holder can be seen in the target cell. It couples LED light (compare subsection 2.3.3) from an optical fiber into the cell and enables a motion of the light spot along the ion beam axis around the former position of the $Ti$ entrance foil. For this measurement, the vacuum chamber was opened and a part of the beam line vacuum piping was removed. A linear drive supporting a PTFE cylinder as a diffuse reflector was inserted and connected to a micrometer screw. By moving the linear drive in the target cell the position versus signal-intensity curve (figure 2.9) was obtained holding LED-currents and PMT voltages constant[17].

[16] Calculated from the known areal density of $1.3\,{}^{mg}/_{cm^2}$ and the volume density of $4.507\,{}^{g}/_{cm^3}$.

[17] Within the short measurement time of $40\,min$ the light emission of the LEDs and the basic sensitivity of the PMTs are assumed to be constant.

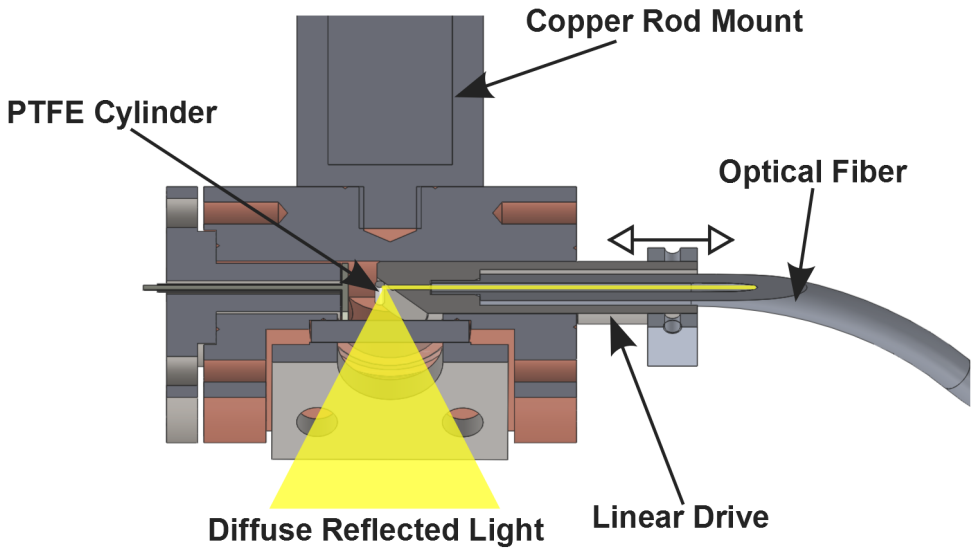


**Figure 2.8:** Position sensitivity test experiment. This drawing shows the modified target cell. The titanium foil and its mounting is replaced by a linear drive which holds an optical fiber. Light from the PMT calibration setup is directly guided into the cell, hitting a polytetrafluorethylene (PTFE) cylinder at the very end of the linear drive. The light gets scattered through the $MgF_2$-window towards the PMTs. The linear drive can be moved in the indicated direction by a micrometer screw (not shown) from the outside of the vacuum chamber.

The normalized PMT signals from $1\,mm$ before the $Ti$ entrance foil to the end of the target cell is shown in figure 2.9. As the LED intensities were not changed, this diagram demonstrates that there is no variation in the detection sensitivity due to the position of the light emission on the level of accuracy until approximately $2.4\,mm$ behind the $Ti$ foil position. However, also afterwards both signal curves are decreasing nearly the same way. This means the NIR-to-VUV ratio measured is not influenced. Only at the very end of the cell the measured signals are drifting apart. This could lead to a decrease in the scintillation ratio solely for the wide-ranged high-energy $^1H$ ions and only at the very end of their tracks, whereas light is detected from the excited volume of the whole track.

This test experiment revealed that a light detection setup should be tested on a possible position sensitivity for absolute as well as for relative measurements, especially at the edges of the target chamber. For the present thesis, the sensitivity on the scintillation ratios is not dependent on the positions in the range of the different projectiles. Only the very end of one of the $^1H$ tracks has to be excluded.

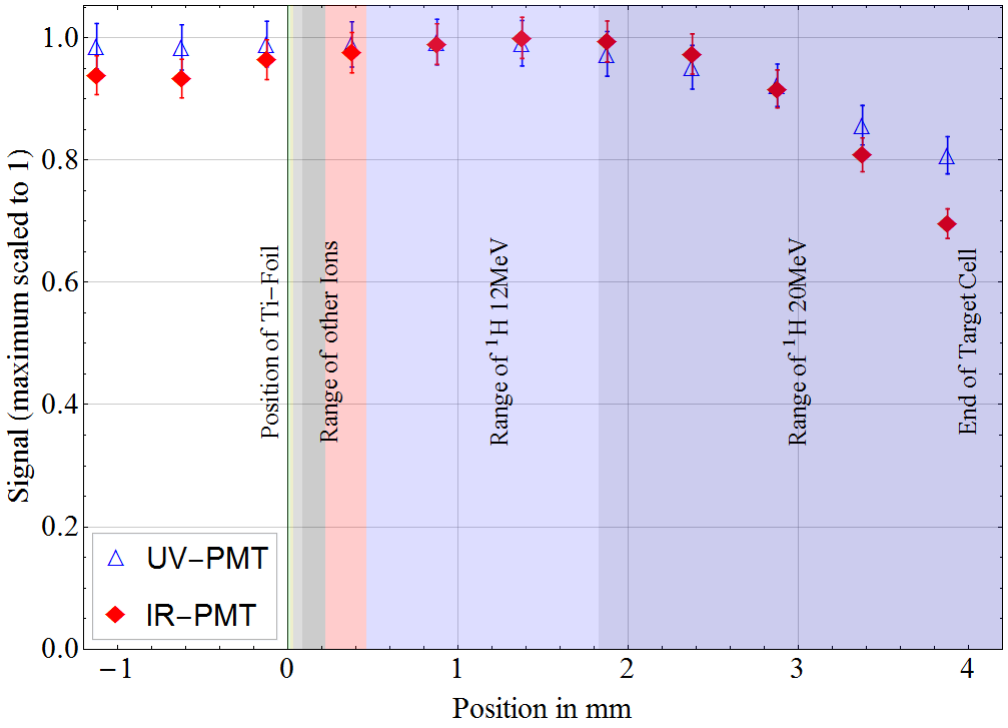


**Figure 2.9:** Signal intensity versus position of the light spot. The x-axis in this plot marks the position of the light spot relative to the $Ti$-foil at $0\,mm$ and the end of the target cell at about $4\,mm$. For both PMTs, the signal intensities (maxima scaled to 1) plotted with their uncertainties are lying on top of each other for a long range after the $Ti$ entrance foil. The ranges of the $^1H$ ions and of the other ions which were used in the experiment are color marked.

## 2.4 Data Acquisition

For photon counting the negative current pulses from the electron avalanches of the PMTs are sent to constant fraction discriminators (CFDs). Their thresholds are set to achieve linearity of the signal and a maximum signal-to-noise ratio using the calibration setup described in 2.3.3. For this purpose, different thresholds were tested and the PMTs were illuminated by the LEDs. The settings with best sensitivity and linearity were maintained for the beam time measurements.

The data acquisition is completed by two counters which are connected to a common timer. The application of this assembly is described in section 3.2.

# Chapter 3

# Ion Beam Experiment

The goal of this thesis is to investigate a possible particle or energy dependence of the NIR-to-VUV scintillation ratio of a liquid $Ar$-$Xe$ mixture. The basic concept for the experiment is to excite the liquid $Ar$ containing a volumetric fraction of $10^{-5}$ of $Xe$ by different ions from a particle accelerator. In contrast to the usual setting in rare event physics not only one single event is observed by a bunch of light detectors but two distinct photomultipliers are detecting many single events from a continuous particle beam. If the single events, i. e. the tracks of the projectiles, are separated well enough, this method provides a high signal-to-noise ratio and good statistics, even for small solid angles and a target cell of a few $cm^3$. The selection of the ions was done in such way that a huge range of parameters like ion mass, atomic number, particle energy, and average linear energy transfer (LET[1]) could be covered.

## 3.1 Selection of Ions & Energies

The Tandem van de Graaff Accelerator at the Maier-Leibnitz-Laboratorium (MLL) can provide ions of nearly every element in the periodic table. The usable acceleration voltage ranges from 6 to 11 $MV$. Depending on the charge and the mass of the ions values of 0.85 to 20 $^{MeV}/_{u}$ can be reached [82, chapter 10 ]. This section explains the selection of the ions and their energies as well as the efforts to plan and to carry out the experiments for obtaining reliable results.

[1] In this work, LET is used for the total energy loss of the projectile per unit length.

### 3.1.1 Calculations & Estimations of Energy Deposition

To cover a wide parameter space in the experiment, different ions and energies have to be selected. Attention is paid especially to the LET, the value of energy deposited per unit length along a particle path. Other parameters are the energy per nucleus when entering the liquid, corresponding to the projectile's velocity, and the penetration depth, i. e. the length of the ion path. The energy deposition in the titanium ($Ti$) entrance foil has to be taken into account, too. Below a certain threshold energy, which depends on the particle mass and the foil thickness as well as its tilting angle[2] with respect to the particle beam, the particle gets stuck in the titanium foil and can not enter the liquid rare gas target. However, already before this happens, the energy dissipation in the $Ti$ foil can get high, especially for larger particle currents, leading to the risk of breaking the foil and flooding the accelerator beam line.

| *Ion* | $E_0$ | $E_{depo}$ | $E_{depo}/m$ | $\Delta x$ | $E_{depo}/\Delta x$ | $E_{Bragg}$ | $\frac{dE}{dx}\mid_{Bragg}$ |
|---|---|---|---|---|---|---|---|
| | $MeV$ | $MeV$ | $MeV/u$ | $mm$ | $MeV/mm$ | $MeV$ | $MeV/mm$ |
| ${}^{1}_{1}H^{+1}$ | 12.00 | 11.95 | 11.95 | 1.824 | 6.55 | 0.2016 | 53.7 |
| ${}^{1}_{1}H^{+1}$ | 20.00 | 19.97 | **19.97** | **4.492** | **4.44** | 0.2016 | 53.7 |
| ${}^{7}_{3}Li^{+3}$ | 44.0 | 43.3 | 6.18 | 0.463 | 93.4 | 1.7540 | 311 |
| ${}^{12}_{6}C^{+6}$ | 42.0 | **37.7** | 3.14 | 0.0849 | 444 | 3.480 | 719.0 |
| ${}^{12}_{6}C^{+6}$ | 77.0 | 74.2 | 6.18 | 0.2235 | 332 | 3.480 | 719.0 |
| ${}^{32}_{16}S^{+10}$ | 79.8 | 54.7 | 1.710 | 0.0315 | 1 737 | 19.183 | 2 105.5 |
| ${}^{127}_{53}I^{+14}$ | 108.0 | 40.3 | **0.317** | 0.017 58 | 2 291 | 406.08 | 6 815.7 |
| ${}^{127}_{53}I^{+17}$ | 198.1 | **109.7** | 0.864 | 0.0315 | **3 481** | 406.08 | 6 815.7 |
| | | [87] | | | | [88] | |

**Table 3.1:** Energies, ranges, and energy depositions for all tested ions. The ions are designated by their symbol, mass number, atomic number, and the charge state until they reached the entrance foil. $E_0$ is the initial energy after leaving the accelerator. $E_{depo}$ is the energy after the entrance foil, i. e. the particle energy deposited in the rare gas mixture. $E_{depo}/m$ is the energy per mass and nucleons, respectively. $\Delta x$ is the range of the ions within the target cell. $E_{depo}/\Delta x$ is the **average** energy deposited per unit path length. $E_{Bragg}$ is the energy where the stopping process has its Bragg peak with the specific **differential** energy deposition $\frac{dE}{dx}\mid_{Bragg}$. Note that the iodine ions have already an energy lower than $E_{Bragg}$ when entering the target cell. Values from [87, 88].

[2] As mentioned in the previous chapter, the angle between the beam axis and the $Ti$ foil surface-normal is 48.6°. Thus the effective thickness is increased by $1/\cos(48.6°)$ to approximately $4\,\mu m$.

Based on calculations using the program ATIMA [87] and the experience gained in different test runs (see subsection 3.1.2) the ions which are summarized in table 3.1 were chosen. In the second column the initial energies $E_0$ of the particles when leaving the accelerator are listed. $E_0$ gave the working name for a specific ion beam, e. g. ${}^{12}_{6}C^{+6}$ with $E_0 = 77.0\,MeV$ is denoted as $C77$.

For all ions appearing pairwise in table 3.1 the highest and the lowest stable acceleration voltages of the tandem accelerator were used. For ${}^{32}S$ the energy was selected such that the penetration depth is the same as for one of the iodine projectiles. For ${}^{7}Li$, the acceleration voltage could be set to match the velocity with one of the carbon projectiles. This was done to keep the velocity of the projectile fixed while changing only the particle type.

The third column ($E_{depo}$) of table 3.1 shows that the entrance foil is a significant barrier for heavier ions. While protons are entering the target medium with a loss $< 1\,\%$ of its initial energy, iodine is losing up to 63% of $E_0$. For physical considerations concerning the scintillation, only $E_{depo}$ is relevant.

The values for the energy per nuclei ${}^{E_{depo}}/_{m}$ show the range that can be covered by the tandem accelerator: From $19.97\,{}^{MeV}/_{u}$ for ${}^{1}H$ to $0.317\,{}^{MeV}/_{u}$ for ${}^{127}I$, leading to velocities from 20% to 2.6% of the speed of light. This is one of the main reasons for choosing a tandem accelerator.

The penetration depths $\Delta x$ are covering three orders of magnitude: $4.470\,mm$ for the higher energetic ${}^{1}H$-ion down to $17.50\,\mu m$ for one of the ${}^{127}I$-ions. Although the range $\Delta x$ is increasing with higher energy per nuclei ${}^{E_{depo}}/_{m}$, the LET values, i. e. the average energy deposited per unit path length, are also covering a wide range because the overall ion energy has to be taken into account.

For a more detailed consideration not only the average but also the differential energy deposition per path length ${}^{dE}/_{dx}$ are important and thus the maximal values, which occur at the Bragg peak for each accelerated ion, are summarized in the last column of table 3.1. It is worth mentioning that this quantity does not depend on the initial energy. All ions are stopped within the target cell and, therefore, are reaching this value just once along the path, if they have started with an energy high enough. Additionally, it has to be mentioned that the light detectors monitor the entire particle tracks from the $Ti$ entrance foil to the end of the target cell.

**Separation of Particle Tracks** Using the values from table 3.1, it is now possible to calculate also the maximally allowed electrical currents to prevent overlapping of the tracks as mentioned in subsection 1.6.1. With well separated tracks the observed light can be taken as originating from undisturbed scintillation processes. To perform the experiment in such a way a knowledge of the upper

limit of particle currents is necessary. To calculate the maximal track diameter the formulas (1.5), (1.3) and (1.4) are used. The allowed current $I_{ion}$ is then derived by use of the equations (1.1) and (1.2). Table 3.2 shows the results of the calculations and the actual electrical currents measured in the experiment.

| Ion Beam | Track Diameter | Allowed Current | Measured Current |
|---|---|---|---|
| $^{1}H\ 12\,MeV$ | $9.92\,\mu m$ | $203.9\,pA$ | $15\,pA$ |
| $^{1}H\ 20\,MeV$ | $24.52\,\mu m$ | $33.3\,pA$ | $3\,pA$ |
| $^{7}Li\ 44\,MeV$ | $3.108\,\mu m$ | $6.22\,nA$ | $4\,pA$ |
| $^{12}C\ 42\,MeV$ | $950\,nm$ | $133.4\,nA$ | $550\,pA$ |
| $^{12}C\ 77\,MeV$ | $3.108\,\mu m$ | $12.43\,nA$ | $400\,pA$ |
| $^{32}S\ 80\,MeV$ | $327\,nm$ | $1.875\,\mu A$ | $160\,pA$ |
| $^{127}I\ 108\,MeV$ | $17.10\,nm$ | $959\,\mu A$ | $450\,pA$ |
| $^{127}I\ 198\,MeV$ | $98.8\,nm$ | $34.9\,\mu A$ | $390\,pA$ |

**Table 3.2:** Calculated and measured maximal electrical ion beam currents and maximal track diameters directly behind the entrance foil. This table summarizes the results of the calculations from subsection 1.6.1 for comparison, whereby the second and third columns are representing the values given by the use of the ion beams of the first column. The last column is showing the actual electrical currents measured. Note the use of different units within the columns.

Table 3.2 indicates that all electrical beam currents used were kept at least one order of magnitude lower than the allowed settings. Though the calculations are derived adopting uniformly distributed particle tracks there is still a large margin due to the fact that only a small fraction of the measured beam current can enter the target cell. This is because the smallest aperture in front of the target cell and behind the last Faraday cup in the beam line has a diameter of $0.5\,mm$ whereas typical particle beams of the tandem accelerator are several millimeters in diameter and the currents increase by the squares of these values. In addition, the calculations were performed assuming that the whole electrical current measured by the Faraday cup passes through the smallest aperture, which, however, is not the case, since typical beam diameters are in the range of several millimeters.

**Potential Surface Effects** As addressed in subsection 2.3.5, the penetration depths $\Delta x$ (table 3.1) have to be compared with the track diameters (table 3.2) to make sure that the excitation happens in the bulk medium and that the $Ti$-foil is not of major influence.

| Ion Beam | Reduced Energy $E_{depo}$ | Penetration Depth $\Delta x$ | Maximal Track Diameter |
|---|---|---|---|
| $^{1}H$ 12 $MeV$ | 11.95 $MeV$ | 1.816 $mm$ | 34 $nm$ |
| $^{1}H$ 20 $MeV$ | 19.97 $MeV$ | 4.470 $mm$ | 45 $nm$ |
| $^{7}Li$ 44 $MeV$ | 43.3 $MeV$ | 461 $\mu m$ | 24.6 $nm$ |
| $^{12}C$ 42 $MeV$ | 37.7 $MeV$ | 84.6 $\mu m$ | 17.4 $nm$ |
| $^{12}C$ 77 $MeV$ | 74.2 $MeV$ | 222.6 $\mu m$ | 24.6 $nm$ |
| $^{32}S$ 80 $MeV$ | 54.7 $MeV$ | 31.4 $\mu m$ | 12.8 $nm$ |
| $^{127}I$ 108 $MeV$ | 40.3 $MeV$ | 17.50 $\mu m$ | 5.4 $nm$ |
| $^{127}I$ 198 $MeV$ | 109.7 $MeV$ | 31.4 $\mu m$ | 9.0 $nm$ |

**Table 3.3:** This table compares the penetration depth $\Delta x$ with the maximal diameter of the track at the reduced particle energy behind the entrance foil. This table is a compilation of the values from tables 3.1 and 3.2.

It can be seen in table 3.3 that the penetration depths are at least one thousand times larger than the corresponding maximum track diameters for all projectiles used. Thus, the excited volume is a cylinder[3] rather than a disk. Furthermore, the maximal energy deposition, i. e. the Bragg peak, is known to be at the far end of the track for most of the ions[4]. Thus, a negligible impact of surface effects is assumed for the light emission processes in the bulk.

### 3.1.2 Experiences from the Test Runs

When using hydrogen ions as projectiles an induced radioactivity was detectable as the count rates decayed too slowly after the beam was shut off. After installing a movable pinhole aperture with different hole sizes, no "afterglow" was seen anymore: The pinhole aperture prevents the ion beam from hitting walls visible by the PMTs. Parts of the target cell are made of copper and stainless steel and can be activated to a certain amount by particles with energies above the Coulomb barrier.

A setup modification was made to vary the particle energy within minutes instead of changing the acceleration voltage. This voltage change should be avoided, because changing the settings of the tandem accelerator – with exception of the beam current – usually takes several hours. In the setup modification a ladder with

[3]The next closer look in subsection 5.2.1 will reveal it as a cone.

[4]The exception is $I$. It has a higher Bragg peak energy $E_{Bragg}$ than the energy which can be reached by the Munich tandem accelerator for this experiment.

gold foils of different thicknesses was placed in front of the target cell. Thus, the ions had to pass through the gold foil as well as the titanium foil and their energy was reduced by specific amounts. However, it was found, that the angular straggling of the ion beam by the gold foils leads to an uncontrollable behavior which could not be overcome by the use of additional apertures. As the data with and without using gold foils could not be compared and some of the ions at certain energies could not pass a gold foil and also the titanium foil, the gold foil ladder was removed. Nevertheless, a large amount of data could be collected within a single beam time, thanks to the dedicated work of the technical staff of the MLL who repeatedly changed the acceleration voltage and the type of ions.

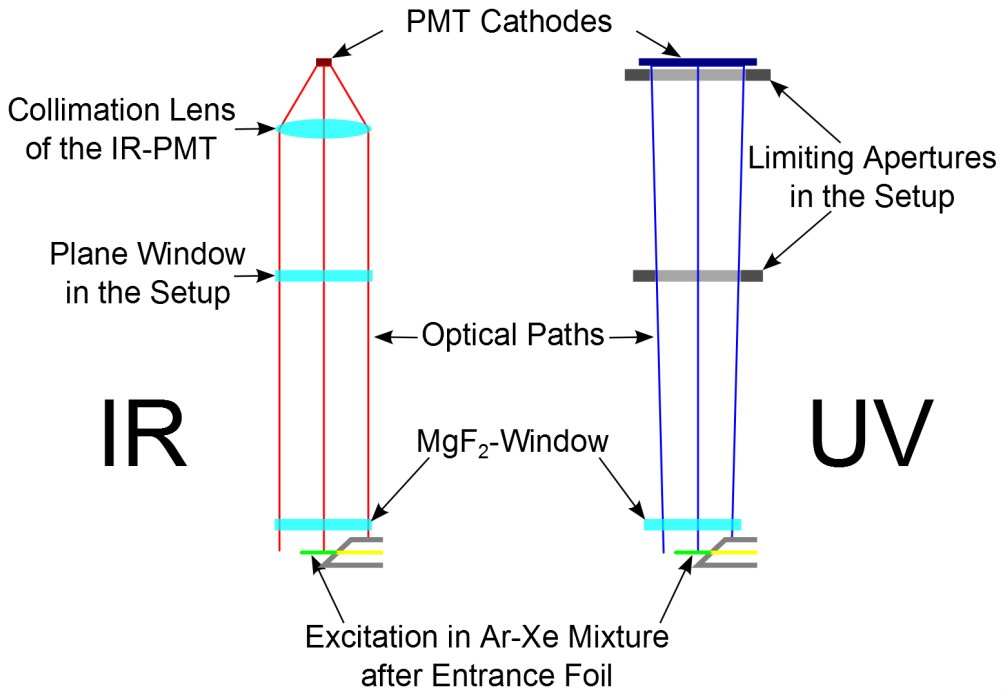


**Figure 3.1:** Schematic drawing of the optical paths from the cathodes of the IR- and the UV-PMT to the excited volume in the *Ar-Xe* mixture. The differences in the paths are due to the collimation lens implemented in the IR-PMT, while the UV-PMT has no restricting optics except some apertures that arise from the mounting itself. At the bottom the excited volume (green) and the entrance foil holder are shown (beam from the right).

The IR-PMT is designed for the detection of incident parallel light which is internally focused onto the cathode (see subsection 2.3.1). In the beginning of the test runs a second lens was used to focus onto the light emitting region, not to lose solid angle due to its collimation lens. However, because of the different ranges of the ions and the mounting of the PMT it was found that a widened view by the use of a

plane $MgF_2$-window in the setup is more important. Both optical paths finally used, for the IR and the UV, respectively, are depicted schematically in figure 3.1. In subsection 2.3.6 is shown that light from all positions along the beam axis in the target cell is equally registered on the IR-PMT cathode in the final experiment.

## 3.2 Beam Time Measurement Procedure

Based on the experience with data taking during the test runs a measurement procedure was set up for obtaining reliable data. There are four different count rates recorded for both data channels, the NIR and the VUV, respectively:

- The **dark count rate** without any light at the PMTs but fixed voltage applied.
- The **LED rate** with light from the calibration setup (2.3.3) using a fixed current for the LEDs[5] and reading the photodiode voltages at the same time.
- The **background rate** with the ion beam shot onto the movable aperture at its blocking position.
- The **beam-induced rate** with the particle beam hitting the mixture and driving the NIR-VUV scintillation.

Each count rate was recorded for a specific integration time from 10 to 100 $s$ and at fixed times in the measurement procedure. In particular, the beam-induced rates are recorded at the start of the particle beam with 10 $s$ and thereafter with 1, 5, and 10 $min$ of continuous beam exposure with 100 $s$ integration time (see figure 3.2).

This was done considering changes in the gas on the minute-scale. The time structure of the measurement procedure was chosen to get insight into potential changes of the mixture – as mentioned in paragraph 2.2.1 – but still long enough to obtain good statistics.

[5] A shutter was used to be able to keep the LEDs running during all measurements.

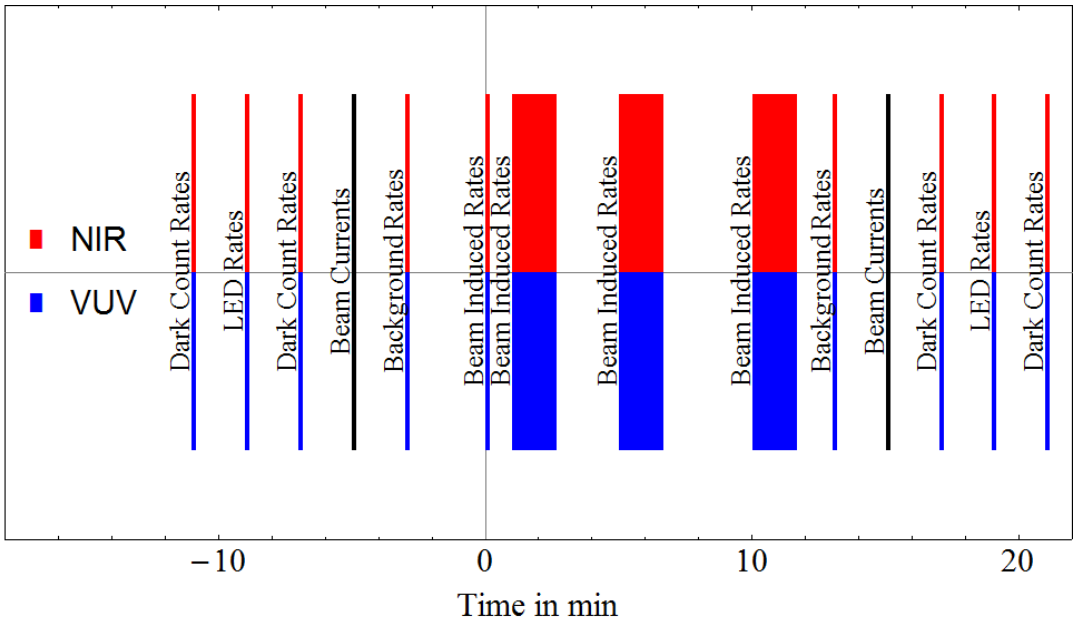


**Figure 3.2:** Visualization of the beam-time measurement procedure, showing a timeline for the different count rates recorded for each ion-beam measurement. Red and blue are the colors for the PMT measurements in the NIR and the VUV, respectively. The beam-current measurements are in black. The zero point of the time line is set as the first hit of the particle beam on the target.

## 3.3 Data Analysis

Due to wanted and unwanted variations in beam current, the absolute values of the count rates cannot be used as a quantity for particle discrimination. On the other hand the scintillation mechanism itself (see 1.4.2) should be affected by the variation of particle type and energy. Thus, both light emission processes could be altered with respect to each other and, therefore, the focus in this analysis is on the **ratio of the NIR emission to the VUV emission**. As shown in subsection 3.1.1 each excitation of the $Ar$-$Xe$ mixture acts as a single event and all the light emission processes in the NIR and VUV, respectively, are summed up separately in the detected count rates. In the following the processing of the raw data is described.

Figure 3.3 shows an example of data obtained for one individual measurement (projectile setting) as explained in section 3.2. There are two sensitivity calibration measurements, one at the beginning and one at the end. Both consist of one LED rate and two dark count readings, each. In between the calibration runs the beam-induced rates were recorded at four different times with 10 and 100 $s$

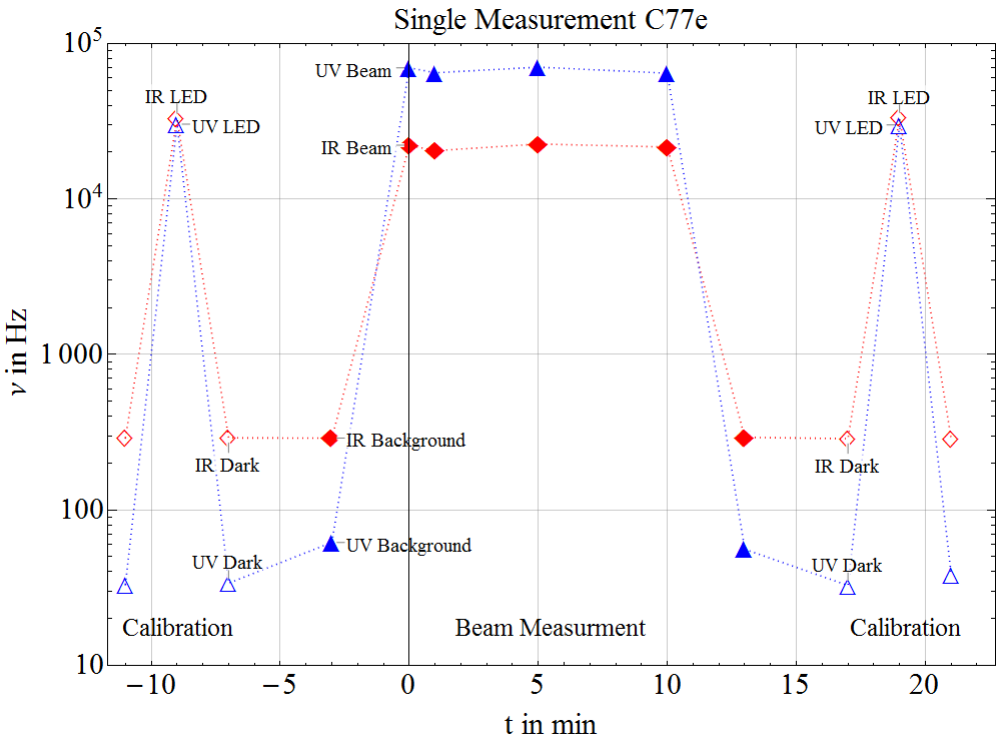


**Figure 3.3:** This diagram shows all measured count rates $\nu$ of both PMTs obtained in one individual measurement with $C$ ions of 77 $MeV$ initial energy. It consists of two calibrations and one beam measurement. Before and after each LED-induced signal, dark count rates were taken, and before and after the beam-induced signal, the background rates were taken. It can be seen that LED-induced count rates are in the same order as the beam-induced count rates and that the UV background is slightly higher than the UV dark count rate.

integration time. Immediately before and after the ion beam irradiation of the mixture the background rate was recorded with the beam stopped in a metal plate directly in front of the target cell.

It is visible in figure 3.3 that the UV cathode is indeed sensitive to the radiation occurring from the beam hitting the metal of the target cell and it's apertures, respectively. However, as the background rates stay at the same level before and after the irradiation of the $Ar$-$Xe$ mixture an activation of material in the target cell can be excluded.

The raw data of the beam measurements always show small variations in intensity over time. As the directions of these variations are randomly changing and no external parameter can be associated, these fluctuations enter the error calculations by summing up all corresponding counts for one wavelength region. The uncertainty

is then derived by the square root of the counts.

Figure 3.4 is a flow chart depicting an overview of the handling for all measured quantities for calculating the final NIR-to-VUV ratio.

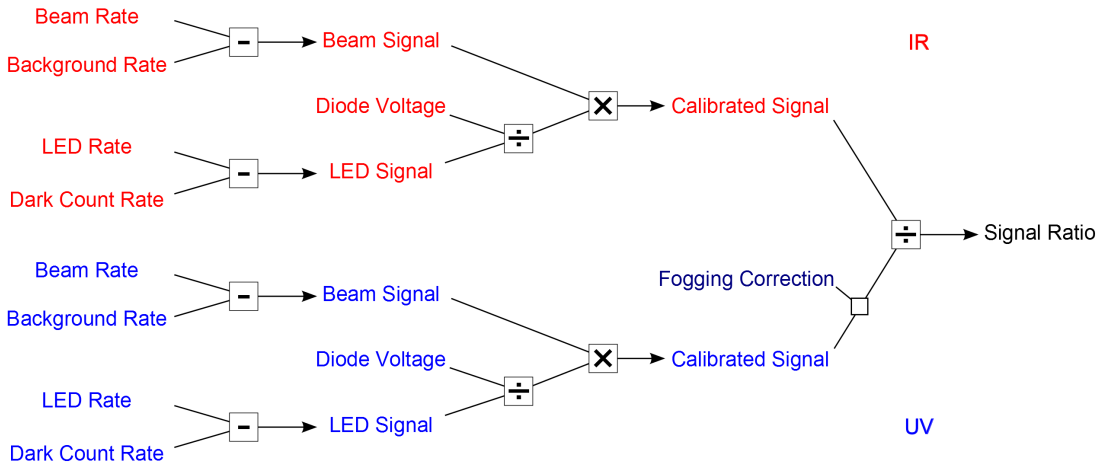


**Figure 3.4:** Flow chart of the data analysis procedure. Starting with four different kinds of count rates the signals are derived by subtracting the background and the dark count rate from the beam-induced and the LED-induced rates, respectively. The sensitivity calibration is done by scaling the beam signal using the diode-voltage-to-LED-signal-ratio. All these steps are done for the IR and the UV branch, where the UV branch needs a time dependent fogging correction in addition. Finally the NIR-to-VUV ratio is calculated by division.

After processing each beam-induced rate[6] from the example in figure 3.3 the signal ratios shown in figure 3.5 can be derived. As for every individual measurement no distinct overall trend of the four signal ratios could be determined, all data from one measurement is combined, leading to one signal ratio value (compare results in subsection 3.3.4).

[6]The beam-induced data points are taken separately for this example, while the surrounding background, LED, and dark count rates are combined.

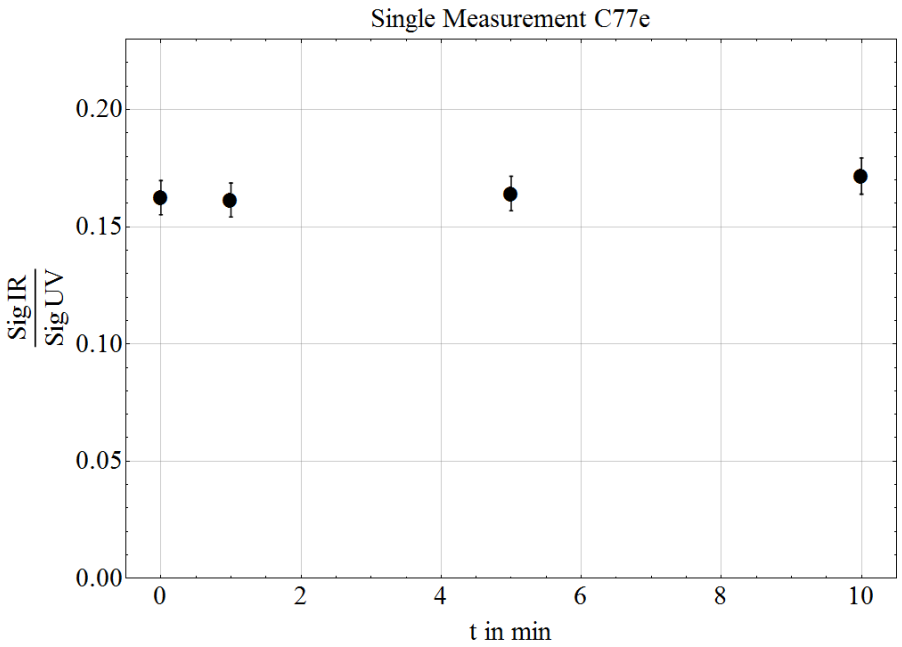


**Figure 3.5:** This diagram shows the results using the described data analysis procedure for each of the four beam-induced rates in a individual measurement.

Figure 3.5 shows exemplarily processed data from one of the individual measurements. In this case, one measurement using a $^{12}C$ beam at an initial energy $E_0$ of $77\,MeV$ is depicted, the fifth ("e") measurement, as denoted in the header ("C77e"). The first data point is from the $10\,s$ interval while the others are from the $100\,s$ intervals of the measurements of the beam-induced rates illustrated in figure 3.2. As none of the individual measurements show a significant trend in its signal ratios, the four values and their errors are combined to one for each particular ion beam setting (e. g. $^{12}C$, $77\,MeV$).

### 3.3.1 Handling of Background

As seen in the test runs, activation of non-target material is possible with some of the ion-beams. To detect and account false signals from beam exposure of material near the target cell, the background rates were recorded and afterwards subtracted from the beam-induced count rates (beam rates in figure 3.4). This provides the true signal of each PMT.

$$(Beam\,Rate) - (Background\,Rate) = Beam\,Signal \tag{3.1}$$

### 3.3.2 Correcting for PMT Sensitivity

As already mentioned in subsection 2.3.3 the calibration of the PMTs depends on the LED-induced signals, derived from the LED-induced PMT count rates (LED rate in figure 3.4) and the dark count rates, as well as on the corresponding photodiode reference signals (diode voltage in figure 3.4). The beam-induced signals are thus scaled by the ratios of the corresponding calibration measurements, the calibration factor in equation (3.2):

$$\frac{Diode\,Voltage}{(LED\,Rate) - (Dark\,Count\,Rate)} = \frac{1}{PMT\,Sensitivity} = Calibration\,Factor \tag{3.2}$$

For example, a smaller LED rate due to a temporary lower sensitivity of the PMT leads to an increased calibration factor and to a correction towards higher signal values in the final formula. Consequently, the ratio given by equation (3.2) is the inverted PMT sensitivity. To give an impression of the impact of the calibration, figure 3.6 shows the variation of the calibration factor calculated by equation (3.2) throughout the whole beam time.

The calibrated signal is then derived by the beam signal from equation (3.1) and the calibration factor by the following formula:

$$(Beam\,Signal) \cdot (Calibration\,Factor) = Calibrated\,Signal \tag{3.3}$$

### 3.3.3 Consideration of Fogging

It is known from the experiments performed by M. Hofmann [74] and A. Neumeier [89, 52] that an insufficient vacuum[7], containing residual gases and especially water vapor, can lead to "fogging" of optical windows for UV light in the form of an

[7] Pressure $> 10^{-7} mbar$.

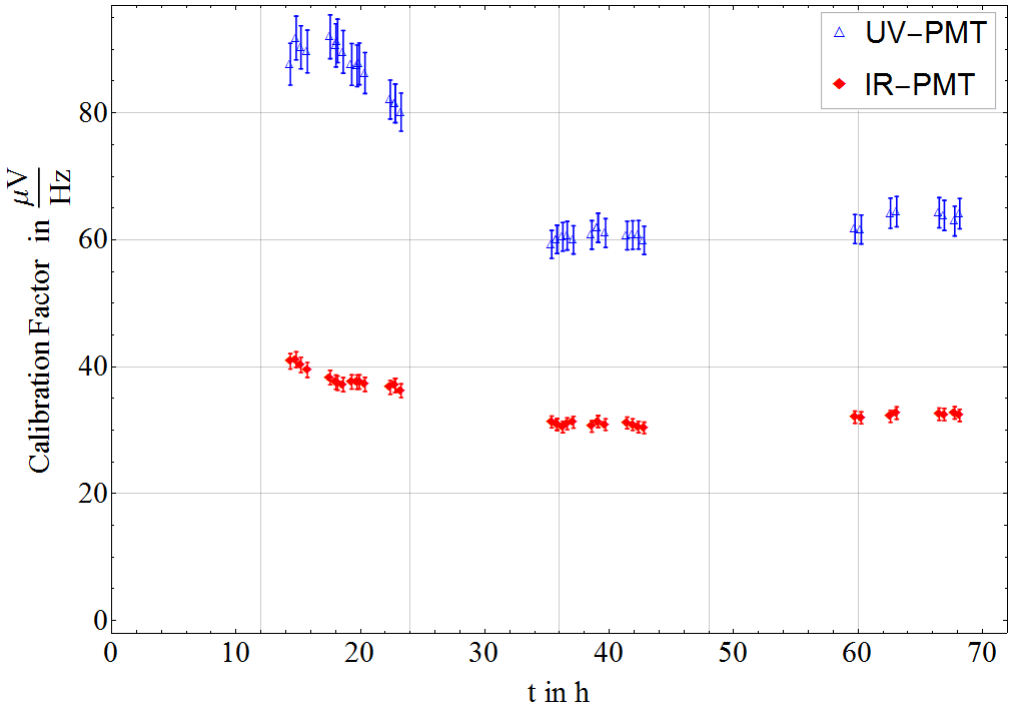


**Figure 3.6:** Variation of the calibration factor (inverted PMT sensitivity) during the beam time. The ratio of the measured values of photodiode voltages and LED-induced signals for the IR and the UV are plotted linearly against a 3-day timeline ($72\,h$). Note the large variation in the sensitivity on the first day where the PMTs still seem to be warming up.

absorbing layer. The vacuum of the beam line and also around the target cell is of such a kind. Luckily, a fogging correction exists for the cell window, as a similar setup was used before [82, subsection 11.1.4][54, subsection 4.2.3][67]. In contrast to the earlier experiments wavelength-resolved data is not necessary for the correction in this place. However, the known emission spectrum of the VUV has to be convoluted with the wavelength-resolved attenuation curve.

Figure 3.7 shows the initial VUV emission feature of the liquid $Ar$-$Xe$ mixture and the form of the emission, damped after $10\,h$ of cooling[8]. It can be seen that the damping is relatively small for the highest peak in the VUV compared to the emission at shorter wavelengths. The damping effects for all wavelengths are summed up and weighted before application.

[8]The attenuation was calculated, using fit data of a transmission experiment from A. Neumeier [90].

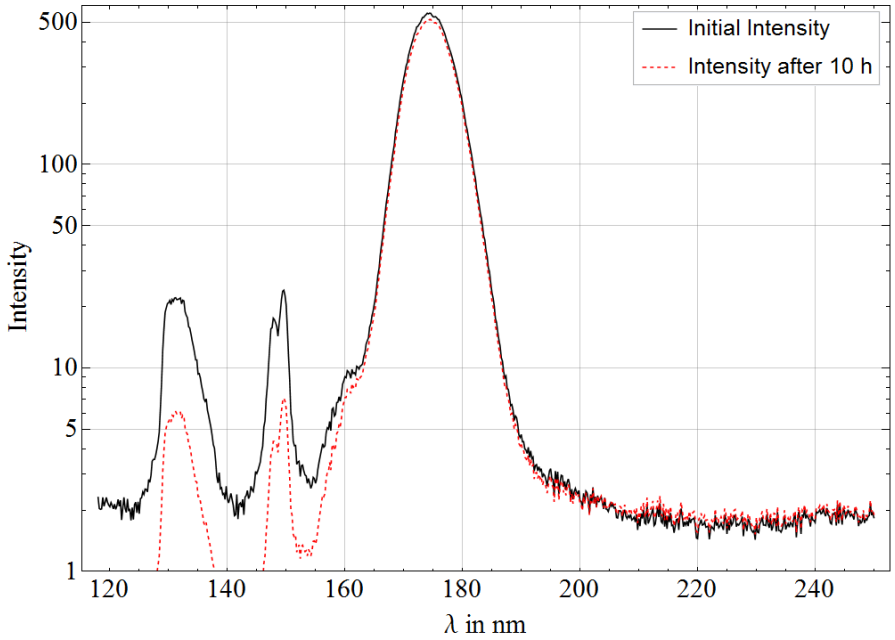


**Figure 3.7:** Attenuation of the VUV part of the liquid argon-xenon emission spectrum due to the fogging effect. This diagram shows the emission features as recorded and corrected by A. Neumeier (black, [90]) and the calculated damped intensity curve after $10\,h$ of cooling (red, dashed). By the use of a logarithmic intensity axis it can be seen that the relative attenuation is much larger for the shorter wavelength of the $Ar_2^*$ excimer at $127\,nm$ than for the $Xe_2^*$ excimer at $174\,nm$.

The resulting correction function can be seen in figure 3.8. For each data set of VUV signals the time interval between the condensing of the mixture and each measurement has to be known before a correction factor can be applied.

Besides the VUV attenuation of the scintillation spectrum an influence on the NIR emission is also conceivable. However, in contrast to the VUV, an enhancement could be possible, too, if the water ice layer works as an anti-reflection coating for certain wavelengths.

### 3.3.4 Discussion of Errors

In this thesis two possible approaches to the statistical uncertainties of the NIR-to-VUV ratios are used, a 'bottom-up' and a 'top-down' concept.

For the bottom-up concept all measurement errors that are known are taken into account for the error propagation to calculate the errors of the data points for

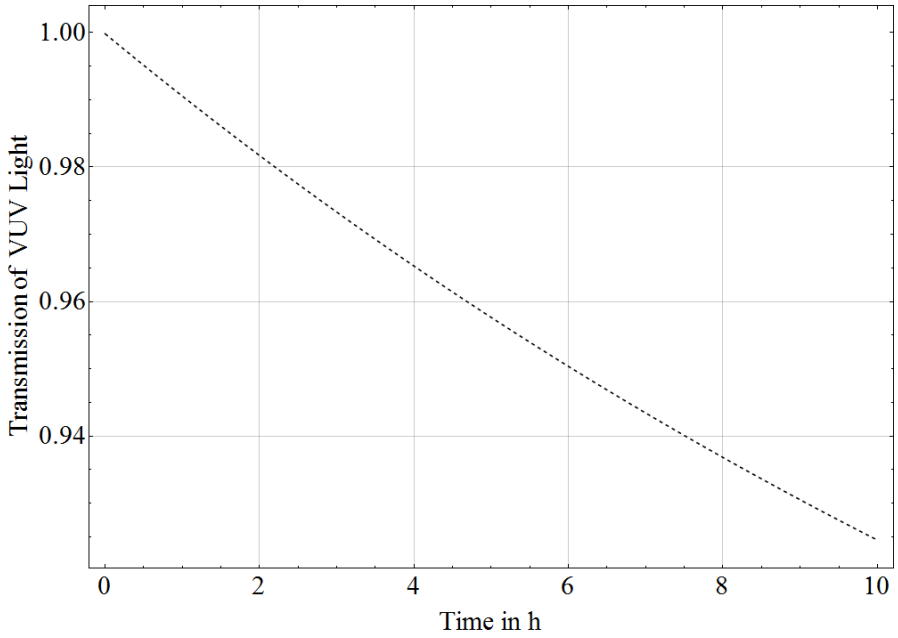


**Figure 3.8:** Attenuation with time of the VUV light due to the fogging effect. This diagram shows the effect of water vapor on a cooled $MgF_2$-window in insufficient vacuum versus time. For the calculation of this curve the fit values of a wavelength-resolved measurement by A. Neumeier [90] were taken and convoluted with the VUV-emission spectrum of the $Ar$-$Xe$ mixture from 120 $nm$ to 240 $nm$. As the measurement was performed in a transmission setup the values have to be corrected from two windows to one window by $e^{\frac{1}{2}}$. As a time dependent factor a correction of beam time data is only possible if the time interval between the liquefaction and the measurement has been recorded.

each individual measurement (like the one shown in figures 3.3 and 3.5). As will be seen soon, an unexpectedly large scatter of the measurement results for the reference particle[9] occurs, especially at higher beam currents, that can not be covered by the error bars generated by the bottom-up concept.

Including the unidentified (systematic) errors, all errors are treated by a top-down concept. The error bars of the mean of all corresponding individual measurements are then calculated assuming that the variations are of statistical nature by use of the standard deviation.

For the bottom-up concept the error propagation is considered as follows. Basically the statistical uncertainty for counting $n$ events depends on its square root. Thus, the relative error of a count rate is $\frac{\sqrt{n}}{n} = \frac{1}{\sqrt{n}}$, if a negligible uncertainty of the

[9] $C$ ion of 77 $MeV$ initial energy with 8 individual measurements.

timer is assumed[10]. This error determination is valid for all recorded count rates, from the dark count rate to the beam-induced rate (see section 3.2). All corresponding count rates from a individual measurement, which did not show any significant trends, were, therefore, taken as one data point by summing up counts and time. The other source of uncertainties are the photodiodes which can be included with estimated systematic errors of about 3% each. An error due to the different positions of the light emissions for different particle beams was excluded (compare subsection 2.3.6). Also dependencies on motions of the optical fiber (see subsection 2.3.3) or the movable pinhole aperture (see subsection 2.3.4) were not seen in test experiments.

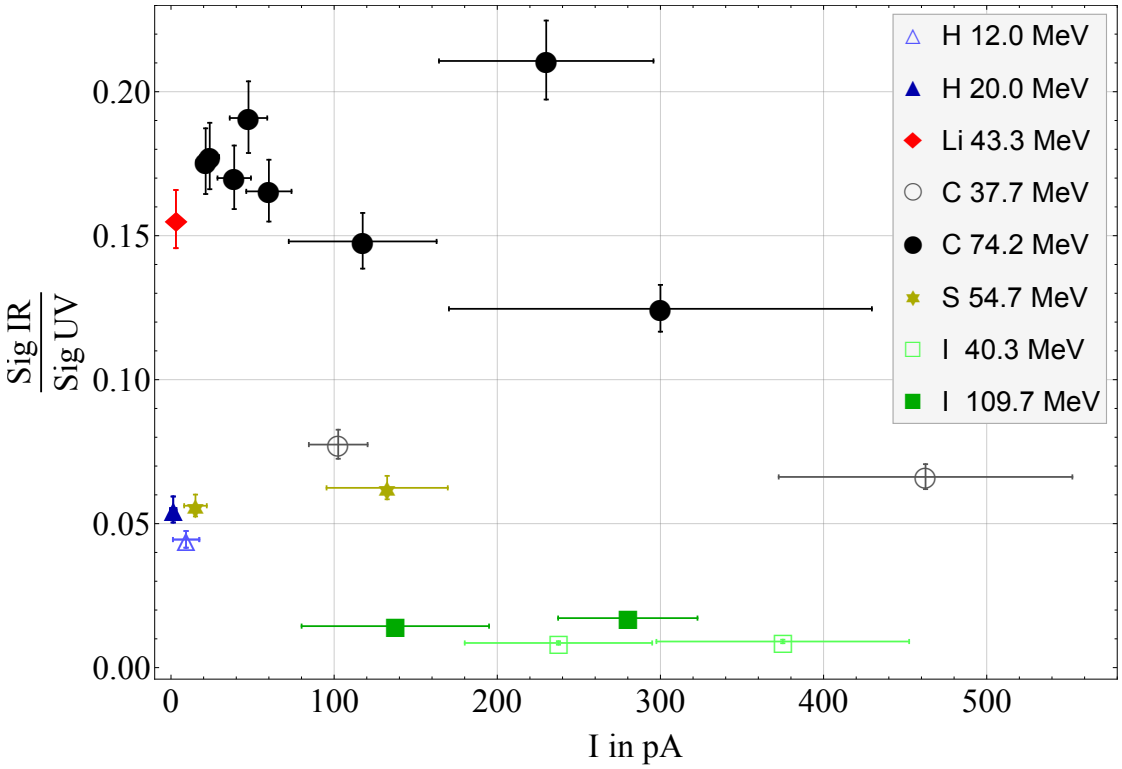


**Figure 3.9:** NIR-to-VUV ratios of all ion beams plotted against the measured beam current. The data points of the reference ion beam (black) of $^{12}C$ with $74.2\,MeV$ are of particular interest. As all the other data points they show no significant trend depending on the beam current in the tested range, but they do show statistical fluctuations on a relatively large scale. These fluctuations are the starting point for the 'top-down' approach for error estimations.

[10]Common quartz clocks are working with a precision of the order $10^{-5}$ to $10^{-6}$. An error which is significantly smaller than the other errors involved.

In figure 3.9 the (vertical) error bars of the calculated error sources are shown. This plot includes the used electrical beam currents (with horizontal error bars) in the different measurements as the abscissa. This allows to check for a potential current dependence. A significant trend of the intensity ratio with beam current can not be found, but the plot reveals fluctuations on an unexpectedly large scale, not covered by the error bars calculated. These fluctuations had been studied in more detail for the reference ion beam C77, the $^{12}C$ ion beam with $E_0 \approx 77\,MeV$ and $E_{depo} \approx 74.2\,MeV$, for which 8 data points were generated. However, no systematic dependence on beam current, cooling time, or aging time of the mixture could be found.

A possible explanation of the fluctuations at higher beam currents could be the setting of the tandem accelerator: For each change of particle type or particle energy the beam has to be steered to the target cell through the whole beam line again. If the beam is slightly misaligned the generation of x-rays near the target cell might be possible, even though a number of apertures were used to avoid this. As the $^{12}C$ ion beam was set up repeatedly from the beginning, there is a finite probability for misalignments in the measurement series. The disturbing influence of a misalignment on the light detection would be higher for higher beam intensities, i. e. beam currents. This would make the values of the scintillation ratios gained at lower beam currents more reliable. However, this is only an assumption. As a consequence another approach for the error calculation – the top-down concept – was made to take the fluctuations into account.

The top-down concept takes the variations that can be seen in a measurement series and uses them for the standard deviation of the mean value[11] for the different ion beam measurements. A measurement series consists of NIR and VUV data of one kind of ion beam in conjunction with a particular initial energy $E_0$ of the ions. Within these series the beam current was varied and some of the data was recorded on different days with new adjustments of the accelerator. While the current variations show no significant trend, as predicted in subsection 3.1.1, the accelerator settings – due to the complexity of the beam steering[12] – and the homogeneity of the liquid rare gas mixture, which has not been tested in this present thesis, are by far the biggest uncertainties for these estimations.

As obviously not all error sources could be unraveled, the decision has been made to use the top-down approach in the final analysis to cover unknown systematic errors. In the case of $^1H$ 12.0 $MeV$, $^1H$ 20.0 $MeV$, and $^3Li$ 43.3 $MeV$ only one measurement

[11] As only a few (maximum of 8) measurements are made with the same parameter settings the Student-t-distribution for small sample sizes was applied to the standard deviation.

[12] For each new ion beam many steering magnets and quadrupole lenses have to be readjusted manually. Usually beam times run with a single kind of ion and one energy only.

per projectile was performed, thus, no standard deviation can be calculated. As an alternative, the maximal relative error[13] from the other ion beams was taken and weighted by the Student-t-distribution for a data set of one.

[13] 15% for the C77 beams. Other ion beam series differ between 7% and 12% standard deviation.

# Chapter 4

# Results: Scintillation Ratios for Different Ions & Energies

The subject of this thesis is to investigate the scintillation of a liquid $Ar$-$Xe$ mixture, in particular the scintillation dependence on the incident particle type and on different particle energies. The scintillation parameter studied is the intensity ratio of the NIR and the VUV emissions under particle excitation. The liquid irradiated with different particle beams of a tandem accelerator is $Ar$ with a volumetric fraction of $10^{-5}$ of $Xe$. This mixture was initially studied by Neumeier et al. using electron beam excitation [53].

If an assignment of the scintillation ratio to the particle type can be made one-to-one, this could be used as a purely optical discrimination parameter in rare event physics. If the assignment is not one-to-one and several particle types or particle energies can be assigned to a specific NIR-to-VUV ratio, data on the dependence of this ratio could still be a useful additional parameter for background suppression.

## 4.1 Scintillation Ratios & Linear Energy Transfer

The NIR-to-VUV ratios are plotted against the calculated averaged linear energy transfer (LET) in figure 4.1. The LET is the energy deposition along the path of the projectile. The averaged values are calculated as the ratio of the total deposited energy $E_{depo}$ and the total ion range $\Delta x$. The LET is taken into consideration because the energy deposition by the projectile is assumed to have an influence on the Wannier-Mott states in the liquid $Ar$-$Xe$ mixture (compare subsection 1.4.2). If the Wannier-Mott states are modified or even destroyed, the infrared emission and the energy transfer mechanism would be strongly affected,

and so would be the scintillation ratios measured. Thus it is expected that the observed NIR-to-VUV scintillation ratio is decreasing with increasing LET. The **averaged** LET values are chosen due to the fact that neither the experimental setup used in this thesis nor the experiments performed in large rare event detectors can make a detailed assignment of $^{dE}/_{dx}$ values along particle tracks. The LET was also considered by Hitachi et al. developing a theoretical model to explain the relative scintillation yield in pure liquid argon for different projectiles [91].

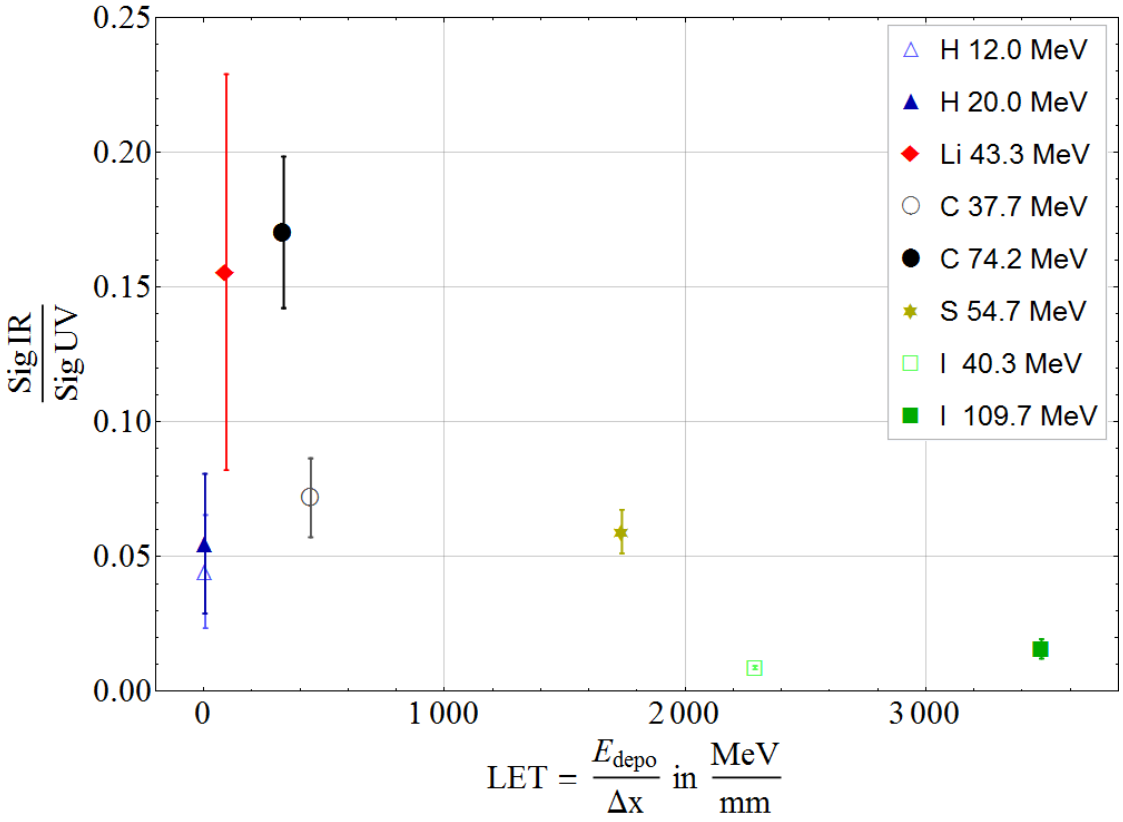


**Figure 4.1:** NIR-to-VUV intensity ratios for all measured ions and energies. This diagram shows the sensitivity- and fogging-corrected average NIR-to-VUV ratios with error bars plotted versus the average LET value, i. e. $^{E_{depo}}/_{\Delta x}$, which is obtained from calculated values of table 3.1. It can be seen that the overall trend is towards less NIR signal for higher LETs with the exception of the hydrogen beam, i. e. the protons. Very prominent is the drop in the ratio from the 74.2 to the 37.7 $MeV$ carbon ions. Note that the values of the scintillation signals from each PMT are not calibrated absolutely. Thus the numerical values of the ratios apply only to the experimental setup described in the present thesis.

The results in figure 4.1 are promising. The NIR-to-VUV scintillation ratios for the various projectiles used show a significant variation in their signal ratios between 0.01 and 0.17 in this particular setup. They depend on the particle type as well as on the particle energy. Note that it can be excluded that a variation of the NIR-to-VUV ratios is an effect of the beam current (see figure 3.9 and subsection 1.6.1).

With increasing mean LET value the NIR-to-VUV ratio is decreasing from the $^{7}Li$ to the $^{127}I$ ions. The $^{1}H$ ions, which have the lowest average LET, are not following this trend: They have a much lower scintillation ratio than $^{7}Li$ and the high-energy $^{12}C$. Considering the error bars it is not absolutely clear if $^{7}Li$ 43.3 $MeV$ or $^{12}C$ 74.2 $MeV$ has the highest scintillation ratio, i. e. the highest NIR fraction.

An increasing particle energy is leading to a higher NIR-to-VUV ratio as can be seen for the $^{1}H$, $^{12}C$, and $^{127}I$ ion pairs. The LET dependence on the particle energy is twofold: For the $^{1}H$ ions and $^{12}C$ ions $E_{depo}/\Delta x$ – the average LET – is decreasing with particle energy[1]. For $^{127}I$ the dependence is the other way round. This is due to the position of the Bragg peak for the heaviest ion used: For the lighter ions the $dE/dx$ values at the entrance foil are decreasing if the particle energy is increased, because the Bragg peak is already in the target volume. For the heavier particles an energy increase is increasing the $dE/dx$ value at the entrance, because the Bragg peak is moved from the outside into the target volume.

Following the average LET values there is a rise on the signal ratios from about 0.05 for the $^{1}H$ ions to above 0.15 for the $^{7}Li$ ion.

The large error bar for $^{7}Li$ originates from the weighting of the standard deviation (see subsection 3.3.4). Within these errors the $^{7}Li$ ion can not be distinguished from $^{12}C$ with 74.2 $MeV$, which follows with the next higher LET and a maximum value of 0.17 for the NIR-to-VUV ratio.

The LET value of the $^{12}C$ ion entering with 37.7 $MeV$ is larger than the value for the $^{12}C$ ion with 77.0 $MeV$ because the former is closer to its Bragg peak energy of 3.48 $MeV$, thus depositing more energy per unit length on its path in the mixture. Between those two $^{12}C$ ions a large drop is found in the NIR-to-VUV ratio just by reducing the ion energy by approximately a factor 2. Similar drops can also be seen by comparing each of the ion pairs of $^{127}I$ and $^{1}H$. For both pairs the corresponding low-energy projectile has a lower NIR-to-VUV ratio although for $^{1}H$ the ratios agree within the error bars.

The change in the signal ratio from the low-energy $^{12}C$ to the $^{32}S$ ion is small compared to the drop between the different $^{12}C$ ions and compared to the error bars. On the other hand the calculated variation in LET is surprisingly high.

[1] The decrease for $^{1}H$ can hardly be seen in diagram 4.1, but it can be read from table 3.1.

The further decrease in signal ratio from the $^{32}S$ to the $^{127}I$ ions is again significant, while the LET is increased by a factor of 1.3. The small error bars for the $^{127}I$ ions indicate a very good reproducibility of the data for both of their energies.

A small rise of the signal ratio between the $^{127}I$ ions – still about a factor of 2 – can be seen going from $40.3\,MeV$ to $109.7\,MeV$. These ions show the same trend as the other ion pairs regarding their deposited energy $E_{depo}$: Higher particle energy leads to higher NIR-to-VUV scintillation ratio. However, in the case of $^{127}I$ the LET values (abscissa) are arranged in the opposite direction. This is due to the fact that $^{127}I$ enters the liquid $Ar$-$Xe$ mixture far below its Bragg peak energy, as explained earlier. Thus, the scintillation ratio is increasing for increasing average LET for these projectiles.

It has to be mentioned that parameters of some projectiles were chosen to match, with the aim that the results can be interpreted regarding these parameters. One kind of parameters matched are the penetration depth of $54.7\,MeV$ $^{32}S$ with that of $109.7\,MeV$ $^{127}I$: $31.4\,\mu m$. This matching of the penetration depth does not show any clear relation to the plotted mean LET ($E_{depo}/\Delta x$) and the scintillation ratio.

## 4.2 Scintillation Ratios & Initial Velocity

The other ion parameter chosen to match is the initial energy per mass $E_{depo}/m$ which corresponds to an initial velocity $v_0$ of the projectiles[2] with $\beta_0 = v_0/c_0$ (equation (1.4)). For this parameter the energy for $^{7}Li$ was adapted to fit the $^{12}C$ $74.2\,MeV$ value of $E_{depo}/m = 6.18\,MeV/u$. This corresponds to $\beta_0 = 0.11$. The resulting similar NIR-to-VUV scintillation ratios (compare figure 4.2) raise the question if $E_{depo}/m$, or rather $\beta_0$, is a relevant variable. For example, the Bethe-Bloch stopping formula for particles contains this variable $\beta_0$.

In figure 4.2 the relation of the signal ratios to the initial velocity $\beta_0$ and, therefore, to $E_{depo}/m$ is investigated. The intentionally selected energy for $^{7}Li$ shows indeed an overlap with the $74.2\,MeV$ $^{12}C$ ion. Comparing with the other projectiles a dependence on the initial velocity $\beta_0$ for all heavy ions regardless of the particle type might be assumed, although the signal ratios of the $^{1}H$ ions do not follow the trend. The average trend seems to be a monotonously increasing NIR-to-VUV scintillation ratio with rising initial projectile velocity. Possible reasons for this behavior will be discussed in the next chapter.

Finally it can be argued that the conducted experiments probably revealed a new parameter for distinction of particles unique for the studied mixture of liquid

[2] This is the velocity of the ions after passing the entrance foil, entering the liquid $Ar$-$Xe$ mixture.

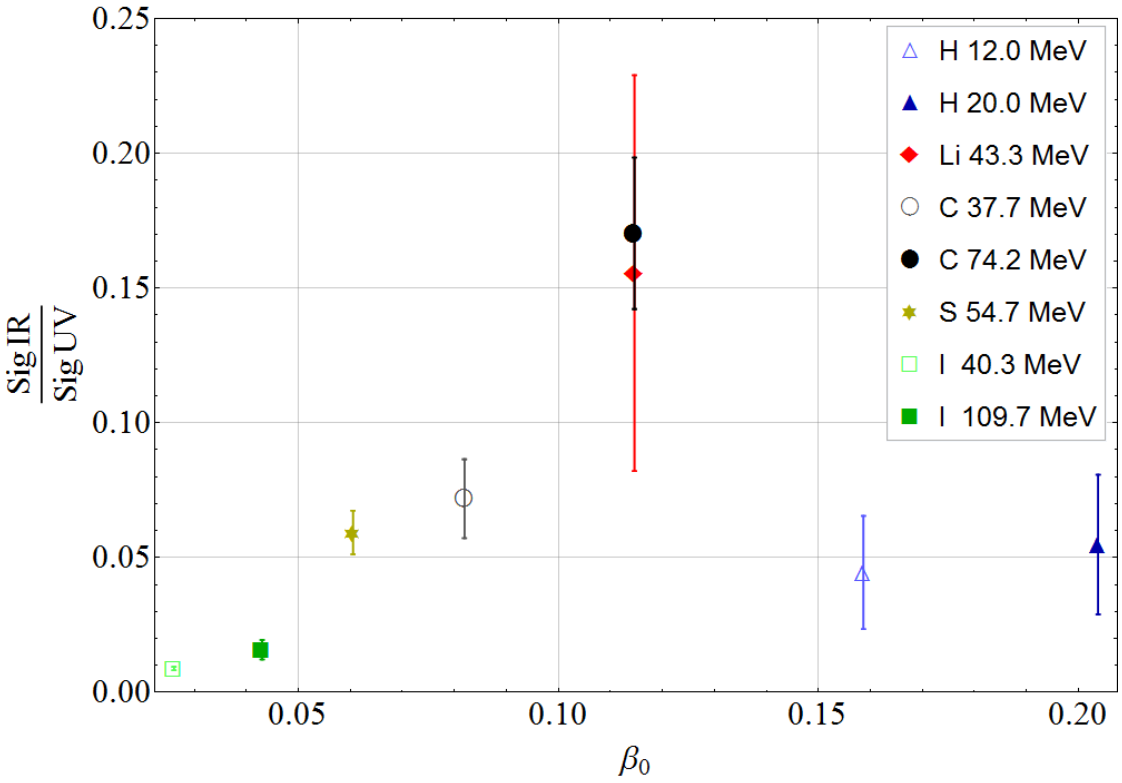


**Figure 4.2:** NIR-to-VUV intensity ratios plotted against the initial velocity $\beta_0 = v_0/c_0$ for all projectiles. The signal ratios grow with increasing velocity up to values for $^7Li$ and the high-energy $^{12}C$ ion at $\beta_0 = 0.11$.

argon and xenon: The NIR-to-VUV scintillation ratio $^{SigIR}/_{SigUV}$. Significant variations of this parameter could be seen, depending on the particle type as well as the particle energy. The scintillation ratio could be used additionally to other parameters like the scintillation decay times or the prompt-to-total light ratio (double phase detector). The missing one-to-one correspondence makes it necessary to use at least one additional parameter. However, if the energy dependence for projectiles of one kind is quantitatively understood, the scintillation ratio could be used as a measure for quantities like the particle energy or velocity.

# Chapter 5

# Discussion of the Results

There are several issues to discuss: The role of the secondary electrons, the excited volume and the energy deposited within it, thermodynamic reactions following the excitation, and the time scales as well as the sequence of all gas-kinetic processes.

The important aspect about the secondary electrons and the excited volume is the energy deposition perpendicular to the projectile path, since the $^{dE}/_{dx}$-values are just revealing the linear energy transfer (LET) to the secondary electrons along the propagation of the projectile.

Using the proposed near-infrared/vacuum-ultraviolet (NIR/VUV) scintillation mechanism discussed by Neumeier et al. [67], energy transfers between different energy levels can be assigned.

Figure 5.1 shows the previously known VUV emission from the $Ar_2^*$ excimer at 127.0 $nm$ (compare figure 2 in [53]) as well as the cascade that is considered for the observed NIR-VUV emission. The time structure and the wavelength spectrum have indicated that the NIR emission (1 173 $nm$) from the Wannier-Mott state is followed by the VUV emission from the $Xe_2^*$-excimer at 174.0 $nm$ [53, 67]. The first assumption then is that both $Xe$ emissions should be in a constant ratio, 1:1 if the transition probability between the Wannier-Mott state and the $Xe_2^*$-excimer is 100 %. For the present setup, however, an 1:1 ratio can not be seen directly as the $Ar_2^*$ excimer emission contributes also to the VUV wavelength range.

The results of the experiment (chapter 4) have shown that the scintillation ratio of NIR to VUV is not constant. It depends on the particle type as well as on the particle energy. Thus, there have to be either other paths for energy transfers to other levels or the Wannier-Mott state can not be occupied under certain conditions. Regarding the interpretation of the data, the latter is assumed. As known from the previous study [54], the Wannier-Mott state is only formed in the

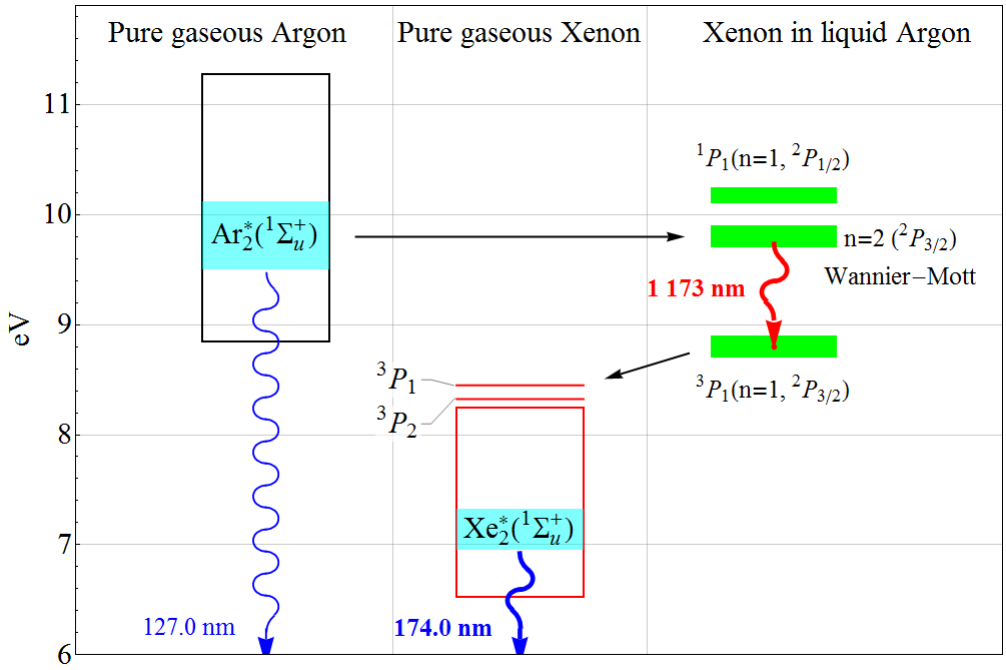


**Figure 5.1:** Excitation scheme showing only the proposed cascade relevant for the NIR emission. This Grotrian diagram is part of figure 1.5 in subsection 1.4.2 but not including the higher energy levels. The focus is on the cascade assumed as necessary for the observed NIR (1 173 $nm$) and VUV (174.0 $nm$) emissions in the liquid $Ar$-$Xe$ mixture. The VUV emission at 127.0 $nm$ represents an alternative emission.

liquid $Ar$-$Xe$ mixture. It is likely that the heavy ion irradiation of the liquid leads to perturbations, preventing the formation of the necessary energy levels.

A key point is the response of the detector medium to the surprisingly high amount of energy deposited in absolutely small volumes. The power densities generated by a single particle on its path through the liquid $Ar$-$Xe$ mixture are of the same order as high-power laser applications, leading to heating, superheating, and vaporization of the liquid within the core of an ion track.

## 5.1 Projectile Path & Track

For the approach of understanding the excitation processes, a distinction have to be made between a particle path and a particle track. The first corresponds to a line that follows the projectile through the medium, depositing its energy at

each point in average by its current $^{dE}/_{dx}$-value. The track, on the other hand, is 3-dimensional, considering the transversal dimensions due to recoiling particles.

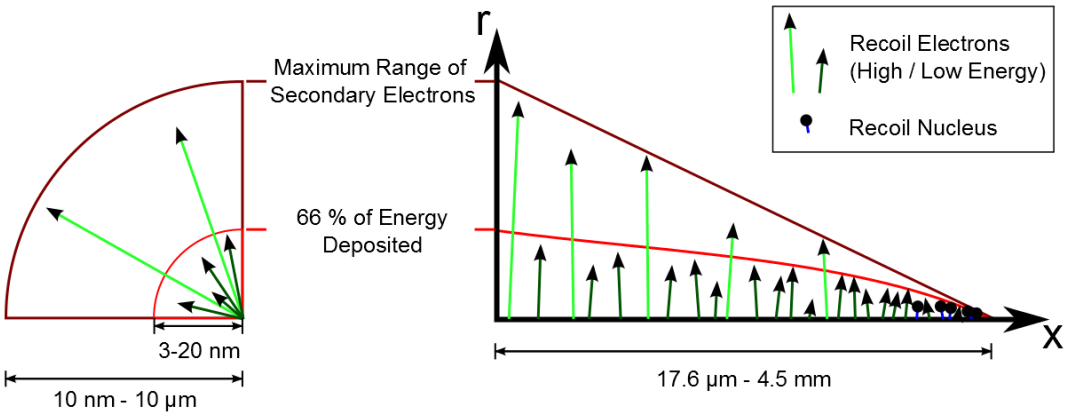


**Figure 5.2:** Scheme of energy deposition perpendicular and along an ion path, denoted as the x-axis. With decreasing energy of the primary particle the maximum range of energy deposition (outer dark red line) is reduced nearly linearly. This range is determined by a moderate number of high-energy secondary electrons (light green arrows). However, the majority of the electrons are low energetic (dark green arrows), leading to a much smaller (down to 500 times) radius for the main region of energy deposition (66 %, inner red line). Both red lines show what is called the track of a projectile, consisting of a so-called core and a halo. Note that the dimensions at the transverse section (left side) apply for the radii at $x = 0$.

To get an idea of the processes involved, figure 5.2 illustrates the electron recoils in the liquid $Ar$-$Xe$ mixture. The particle beam of the tandem accelerator consists of many well separated ions (subsection 3.1.1) and each of them flies its path through the medium, along the $x$-axis shown in the schematic drawing. For all projectiles the major part of the stopping happens via electron recoils. Only at the very end of each path nuclear recoil processes play a significant role[1]. The secondary electrons generated during the stopping process have different energies and, therefore, different ranges in the medium and the volume they reach is called the track of the projectile. The maximum ranges of the energy deposition of the highest-energy electrons are in the order of $10\,nm$ to $10\,\mu m$ (compare track diameter in table 3.2), depending on the projectile and the range is decreasing to zero with decreasing velocity at the end of the path. However, the volume of the main energy deposition is much

[1] A TRIM calculation reveals a maximal fraction of 6.4 % of the total energy for the transfer to phonons for the low-energy $^{127}I$ ion. All other projectiles have less nuclear stopping power.

smaller, generated by the larger amount of secondary electrons with medium and low energies. For the projectiles used here, the so-called core [92, 93, 94] has radii between 3 and 20 $nm$ at the beginning of the projectile path in the medium. In the present thesis, the term "core" is defined by the energy deposition: For each penetration depth $x$ along the path, the border between core and halo is the radius $r$ for 66 % of energy deposited within the core and 34 % in the halo.

## 5.2 Linear Energy Transfer

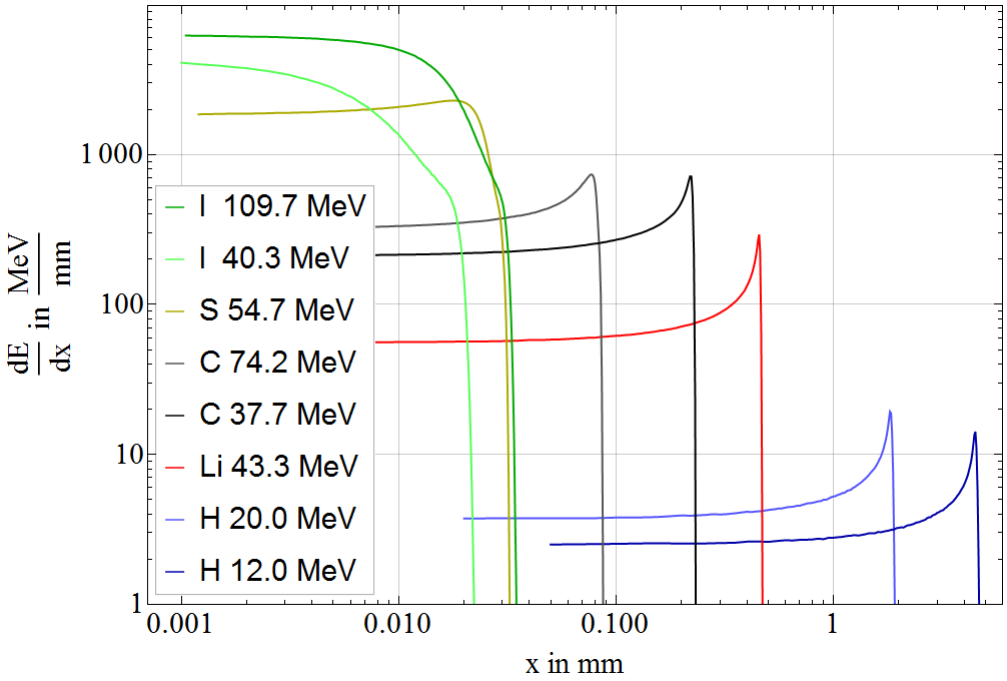


**Figure 5.3:** Total stopping power versus penetration depth for the different ions used as projectiles. The double-logarithmic diagram points out the similarities and differences between the ion beams over four orders of magnitude in range $x$ as well as in energy deposition $^{dE}/_{dx}$. For nearly all ions a prominent Bragg peak can be seen near the end of the path. Considering the logarithmic scale, the impact of the stopping power on the light emission regarding intensity becomes clear, especially for the lighter ions. The reason for the exceptional behavior of iodine (green) is that its energy is well below its Bragg peak energy ($\approx 400\,MeV$). Thus, the energy deposition is only decreasing and the ion is short-ranged. The energy of sulfur (yellow) was chosen to match the range of iodine (dark green), however sulfur has its non-prominent Bragg peak behind the entrance foil, i. e. just within the liquid $Ar$-$Xe$ mixture. Values calculated using SRIM [95].

The well known and often considered LET values lead to a promising arrangement of the signal ratios in diagram 4.1 at first glance, although the hydrogen ions clearly do not follow the trend of the other ions. By looking at the energy deposited along the path, i. e. the stopping power (figure 5.3), which is dominated by electronic rather than nuclear stopping[2], it is obvious that all ions stopped in matter have their maximum energy deposition near the end of their paths, the Bragg peak[3]. This peak is not too prominent, i. e. it does not range over more than one order of magnitude. However, to explain a more powerful influence on the surrounding of the ion path, the argumentation has to go further.

### 5.2.1 Secondary Electrons

Electronic stopping leads to electron recoils with maximal energies from 2 to 50 $keV$ (equation (1.3)) depending on the ion's velocity $\beta$ which can be derived from its energy per mass $E/m$ (compare equation (1.4)). The transferred energies in turn result in different ranges of these secondary electrons, the main carrier of the energy deposited by the high-energy projectile according to SRIM calculations[4] [95]. For a first-order consideration, a perpendicular recoil of the electrons away from the ion path is assumed. The range of these electrons can then be taken as the radius of a cylinder with its axis in $dx$ direction.

Figure 5.4 shows the radii $r_{E_{depo}}$ for the core of the track for the different projectiles used. The values were calculated by the use of equation (1.6). This formula, derived by Toulemonde et al. [80, 81], is based on the work of Waligorski et al. [79]. The radius obtained by this formula is the edge of the core, within which 66 % of the total stopping power is deposited. The input parameter is the energy per mass. As the $E/m$ values are well known [88, 95, 87] along the path the diagram in figure 5.4 can be generated. It shows mainly the fact, that the range of the secondary electrons is decreasing towards the end of the path. Thus, the track is not a cylinder but rather a **cone**.

The concept of looking at the energy distribution along *and* perpendicular to the path is not new [93] and several studies have made a distinction between an inner and an outer volume [93, 91, 96, 94] around the path of the incident projectile (compare figure 5.2). This distinction is made because of the different effects that can appear in volumes that differ in their energy density. As long as

[2] The sum of both stopping powers is depicted in the figure.

[3] For iodine, the Bragg peak can not be seen since these ions do not reach the Bragg-peak energy in these experiments.

[4] Only $^{127}I$ has a significant fraction of nuclear stopping power when its energy has fallen below 70 $MeV$.

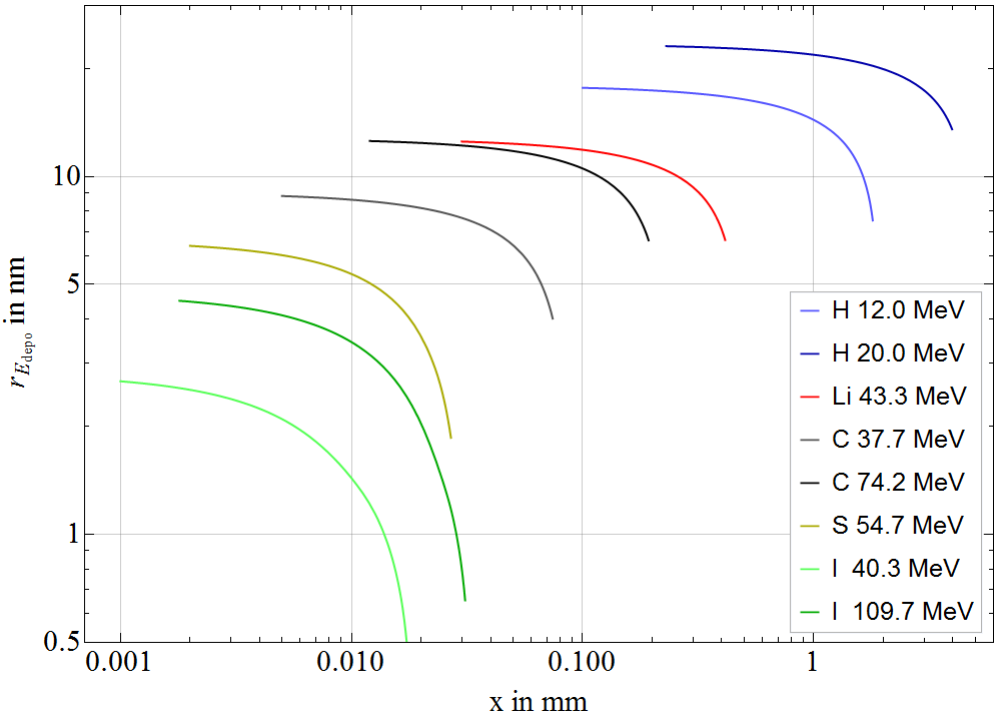


**Figure 5.4:** Range of the energy deposited (66 %) by secondary electrons. This diagram shows on a double-logarithmic scale the results of the empirical formula (1.6) for all projectiles along their path $x$. The track radii $r_{E_{depo}}$ are not as large as the maximal ranges of the secondary electrons and do not differ more than a factor of 10 between all ions used. However, the shape of the curves has to be considered as important, due to the fact that the Bragg peak lies at the end of the path for most projectiles. This leads to a high energy deposition per volume in that region.

secondary electrons play a major role in excitation of target media, the volume they affect has to be considered (see section 5.3).

### 5.2.2 Time Scales

The time periods of various processes involved in the experiment are visualized in figure 5.5. The experiment starts with the injection of the projectiles into the target medium. The time until the accelerated ions are stopped – the time of flight of the projectiles – can be calculated using ATIMA [87]. $^{32}S$ ions are stopped within the shortest period of time of $2.3 \cdot 10^{-12}\,s$ and $1.0 \cdot 10^{-10}\,s$ are needed by the long-ranged $^{1}H$ ions.

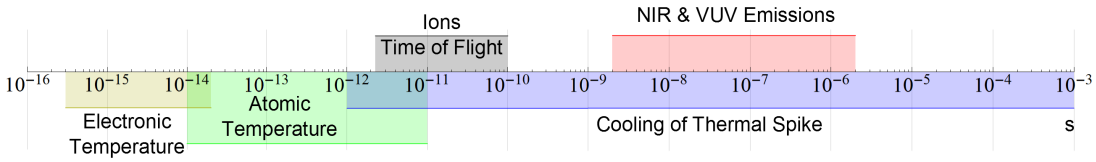


**Figure 5.5:** The timeline shows the time scales for selected processes involved in the experiment. The upper part denotes the processes 'controlled' by the experiment, the lower part shows internal processes in the target medium. Note that there are also emission features of lower intensities with decay times of $3 \cdot 10^{-5} s$ (not indicated). The time of flight of the ions was calculated using ATIMA [87]. The relaxation times of the scintillation processes were experimentally determined in a time structure measurement by Neumeier et al. [53]. Data below the time axis is taken from [94].

This is fast compared to the decay times of the VUV and NIR emissions[5] which occur between $\sim 10^{-9}$ and $\sim 10^{-6}\, s$ [53]. Even faster are the energy deposition and distribution processes in the target medium. Electronic and atomic temperatures rise during the flyby of the ions. The maximum of the electronic temperatures can be reached within $\sim 10^{-14}\, s$. This is the time when the energy is already stored in the volume of the target material. The next step is the increase of the atomic temperature and, therefore, the temperature of the bulk medium. This can take up to $\sim 10^{-11}\, s$, which is interesting, because only the quickly stopped ions[6] have their time of flight within this time scale. This means that for most of the projectiles the track forms during their flyby and is completed before they are stopped.

The widest time scale range is finally used by the cooling processes which start right after the atomic temperature rise ends at $\sim 10^{-12}\, s$, but they can take up to $\sim 10^{-3}\, s$ [94].

As a result not all of the processes occurring during the experiment can be considered independently. As soon as the projectile enters the liquid mixture, energy is deposited and temperature and pressure will begin to rise. Furthermore, the short time scales of the energy deposition indicate that one has to deal with high power deposition, too.

[5] The decay times are of some hundred $ns$ up to a few $\mu s$ but the light emitting processes need about one order of magnitude longer, since the decay is exponential. As a consequence, $5 \cdot \tau_{decay}$ that lead to less than 1 % of intensity is used.

[6] Sulfur is the ion which is stopped within the shortest time: $2.3 \cdot 10^{-12}\, s$.

## 5.3 Average Energy Deposition per Atom

Using the data plotted in diagram 5.4 ($r_{E_{depo}}$ vs. $x$) in combination with the SRIM calculations of the linear energy transfer in figure 5.3 an energy deposition per volume can be calculated. For the infinitesimal volume $dV$ cylinders with their axes in $dx$-direction are used:

$$dV = r_{E_{depo}}^2 \cdot \pi \cdot dx \tag{5.1}$$

With the known density of the liquid mixture the volume $dV$ can be converted into a number of atoms $dN$. The density can be assumed to be constant for these calculations since the time scales for the cooling process (relaxation of temperature and pressure) are much longer than those for creating the excited volume (electron temperature) as explained in the last subsection 5.2.2.

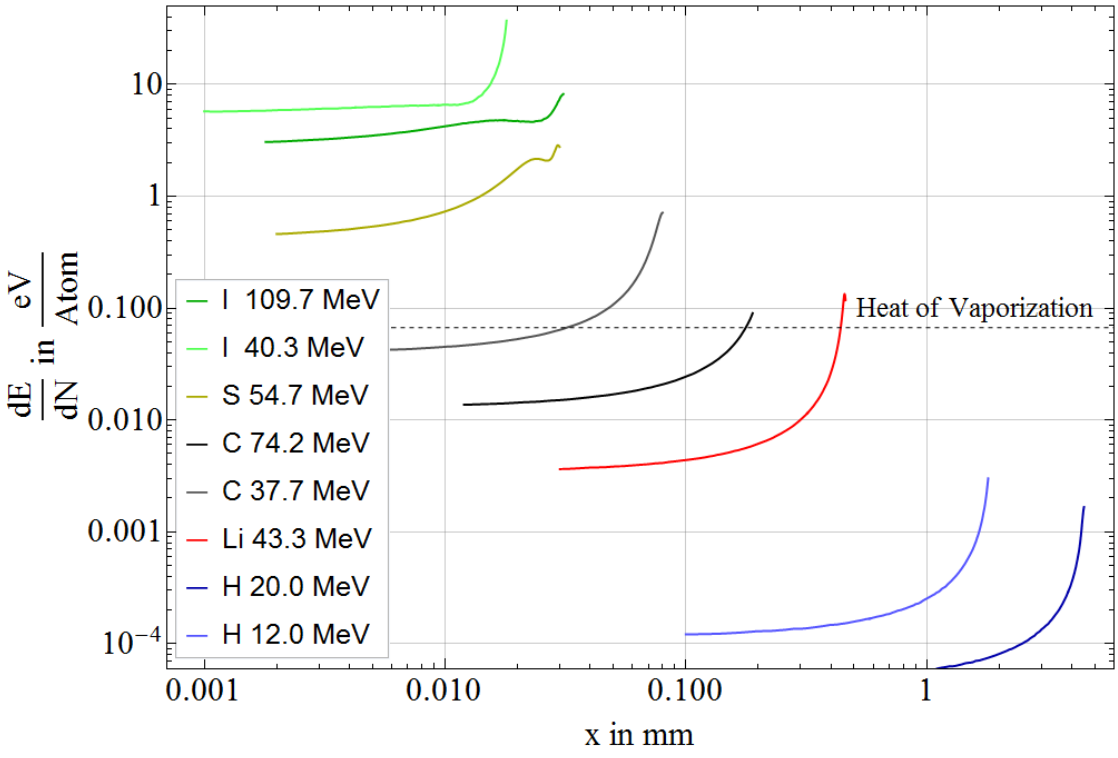


**Figure 5.6:** This diagram presents the calculated average energy deposition per target atom in the core, plotted against the penetration depth $x$. It can be seen that the $^{dE}/_{dN}$ values vary over nearly six orders of magnitude for the projectiles used. Already along the path of one ion the change is at least a factor of 10 with the steepest increase at the end (Bragg peak and cone tip).

Figure 5.6 depicts the deposited energy per atom $^{dE}/_{dN}$ along the ion path $x$ in the liquid $Ar$-$Xe$ mixture for all projectiles used. It can clearly be seen how the energy transfers to the target atoms vary with projectile and penetration depth. The $^{dE}/_{dN}$-values of the different projectiles cover nearly six orders of magnitude. Each particle curve has its steepest increase at the end of its penetration depth. That is where the Bragg peak in the LET meets the cone tip of the shrinking spatial expansion. The more pronounced the Bragg peaks are, the higher the end values for $^{dE}/_{dV}$.

At this point it has to be noted that the values in diagram 5.6 as well as the $^{dE}/_{dx}$ values calculated using SRIM, TRIM, or ATIMA are originating from Monte Carlo simulations with high statistics. Thus, these values are average values for the volume of the track large enough or for the line of the path long enough[7], respectively. The results of the calculations can be used to determine the energy deposition in the medium but they can *not* be used to establish the energy transfer from one projectile in a single collision. Single collisions are statistically distributed along the path and each collision process can transfer enough energy for the excitations that lead to scintillation processes. Such an excitation energy can be found for the $Ar$ I resonance lines with their lowest energy at $\approx 11.6\,eV$ [97, 98]. Starting at this energy or at higher energies the scintillation mechanisms are taking place until the ground state is reached and only thermal dissipation is possible.

The diagram in figure 5.6 allows to compare the deposited energy per atom with certain thresholds in the bulk medium. In the case of liquid $Ar$, the vaporization energy is the interesting one: $66.7\,meV$ per atom are needed to power a phase transition. With this in mind, it is clear that a thermodynamic quantity like temperature is raised under such conditions depicted in figure 5.6. However, it should be emphasized that this increasing temperature is limited to the small volume of the particle track. Additionally, it would be necessary to model the time evolution in the medium, since the time scales of the involved processes are overlapping (see subsection 5.2.2).

### 5.3.1 Power Density

As mentioned in subsection 5.2.2 the power deposited in the target around the path of the projectiles is very high due to the short time scales. Using the projectiles

[7] If only very short ranges have to be considered, it might not be useful to calculate with averaged values due to the distribution of the statistical processes.

time of flight[8] $t_{tof}$ the average power deposition $P_{depo}$ can be calculated:

$$P_{depo} = \frac{E_{depo}}{t_{tof}} \tag{5.2}$$

With the knowledge of the core volume $V_{core}$ of the particle track, derived from the values in table 3.3, an estimate of the mean power density can be made by dividing 66 % of the total power deposition $P_{depo}$ by the corresponding volume, as seen in equation (5.3):

$$\frac{\Delta P}{\Delta V}|_{core} = \frac{0.66 \cdot P_{depo}}{V_{core}} \tag{5.3}$$

| Projectile | $t_{tof}/s$ | $\frac{P_{depo}}{W}$ | $\frac{\Delta P}{\Delta V}\|_{core}/\frac{W}{m^3}$ | $\frac{\Delta P/\Delta V\|_{core}^{heat}}{W/m^3}$ |
|---|---|---|---|---|
| $^{1}H$ 12.0 $MeV$ | $5.41 \cdot 10^{-11}$ | 0.035 | $2.60 \cdot 10^{16}$ | $2.20 \cdot 10^{16}$ |
| $^{1}H$ 20.0 $MeV$ | $1.027 \cdot 10^{-10}$ | 0.031 | $5.5 \cdot 10^{15}$ | $4.6 \cdot 10^{15}$ |
| $^{7}Li$ 43.3 $MeV$ | $1.891 \cdot 10^{-11}$ | 0.37 | $2.11 \cdot 10^{18}$ | $1.78 \cdot 10^{18}$ |
| $^{12}C$ 37.7 $MeV$ | $6.65 \cdot 10^{-12}$ | 0.91 | $5.8 \cdot 10^{19}$ | $4.9 \cdot 10^{19}$ |
| $^{12}C$ 74.2 $MeV$ | $1.128 \cdot 10^{-11}$ | 1.05 | $1.25 \cdot 10^{19}$ | $1.06 \cdot 10^{19}$ |
| $^{32}S$ 54.7 $MeV$ | $2.33 \cdot 10^{-12}$ | 3.8 | $1.21 \cdot 10^{21}$ | $1.02 \cdot 10^{21}$ |
| $^{127}I$ 40.3 $MeV$ | $4.14 \cdot 10^{-12}$ | 1.56 | $5,2 \cdot 10^{21}$ | $4.4 \cdot 10^{21}$ |
| $^{127}I$ 109.7 $MeV$ | $5.32 \cdot 10^{-12}$ | 3.3 | $2.16 \cdot 10^{21}$ | $1.83 \cdot 10^{21}$ |

**Table 5.1:** Average power densities for the different particle tracks. For the calculations the deposited energies $E_{depo}$ and the track dimensions from table 3.3 are used. The time-of-flight values in the second column are from ATIMA calculations [87]. For the power densities in the fourth column just 66 % of $P_{depo}$ enters the calculation because the core radii of the tracks are used. To consider the light conversion efficiency of $(15.3 \pm 4.4)$ % [53], in the last column the power density remaining for thermalization is listed.

Table 5.1 shows the time of flight, the overall deposited power, and the average power density in the particle tracks of the different projectiles. For the power density calculation the core volume of the particle track was assumed to be conical (see figure 5.2).

These calculations reveal power densities extending towards the regime of high-

[8] Values from ATIMA calculations [87].

power laser applications[9]. It can be assumed that the center of the high-energy heavy-ion tracks are reaching those values [94][99, subsection 2.2.2]. The distinction between core and halo of a track is just the first step to describe the power density as a function of the distance to the ion path. Such functions were already modeled for the dose[10] to study the structure of heavy-ion tracks [76]. Consequently, the power deposited closer to the track center will be even higher than the calculated average.

In relation to power deposition, the Bragg peak region is ambivalent. On the one hand, the energy deposition is significantly higher and the volume is smaller. On the other hand, however, the projectile is already slowed down by a certain amount, allowing the energy to be deposited over a longer period of time.

### 5.3.2 Heating & Boiling

Irradiation of solids with high-energy ions is usually accompanied by phenomena of thermodynamics on the **nanometer scale** within the particle tracks [94]. This has not to be confused with the boiling that occurs, if the overall beam power is high enough to vaporize a **macroscopic amount** of the material, if the particle tracks overlap. This would be the case if the ion-beam current would have been to high (compare table 3.2). The next heavy ion would then have probably hit an old track from a previous ion. Thus, the track diameter is defining the macroscopic scale in this case: Above $\sim 17\,nm$ for the heavy $^{127}I$ at $40.3\,MeV$ up to $\sim 25\,\mu m$ for $^{1}H$ at $20.0\,MeV$.

**Macroscopic Heating** Already during investigations by excitation with electrons, T. Heindl observed macroscopic heating of his target material, pure liquid argon. He encountered the emission of the atomic $4p - 4s$ $Ar$I-line, only observable in gaseous $Ar$, at a maximum power density of $6.0 \cdot 10^{10}\,{}^{W}/_{m^3}$ [51, 61]. However, this volumetric power is calculated for the whole electron beam[11] containing many primary electrons per unit area and time. If the beam current was increased further also the formation of bubbles was observed.

The same macroscopic heating was also observed by M. Hofmann in his work on ion beam excitation of liquid argon. The mean power density had to be kept $< 10^{9}\,{}^{W}/_{m^3}$ for the whole excited volume. The $Ar$ I resonance-lines were not visible for

[9] Typical femtosecond laser pulses can reach about $10^{24}{}^{W}/_{m^3}$, considering a depth of the light absorption of $\sim 10\,nm$ [94].

[10] The dose is the energy deposited per mass. It is measured in $Gy = {}^{J}/_{kg}$ and can be converted to an energy density by the density of the medium.

[11] In contrast, the values in table 5.1 are calculated for single particle tracks.

a 120 $MeV$ $^{32}S$ beam (about 104 $MeV$ behind a $Ti$ entrance foil) at a beam current $\lesssim 10\,nA$. However, they would have been visible in the gas phase [74, 82]. For comparison, the beam parameters for the present experiment are 54.7 $MeV$ and $\sim 160\,pA$, respectively. Using these values as well as the penetration depth and the track radius from the tables 3.1 and 3.2, an average power density of $\sim 1.4 \cdot 10^8\,{}^W/_{m^3}$ can be calculated. The highest average power density is found for the high-energy $^{127}I$: $\sim 4 \cdot 10^8\,{}^W/_{m^3}$. Thus, the threshold for macroscopic boiling was not reached.

**Microscopic Heating** A wide field of research is the microscopic heating and melting of solids in the vicinity of the ion paths, e. g. in condensed matter [94] and biophysics [80]. Achievements in these research fields are used in the present thesis for determining the energy deposition transverse to the ion path, generating a superheated track for various projectiles. As this study focuses on the events in single particle tracks, they are interesting for detector physics, too.

A very promising theoretical description turns out to be the inelastic thermal spike (i-TS) model. It describes the effects of the energy transfer to the medium by numerically solving the heat diffusion equations [100]. Calculations using this model reveal an overheating and boiling of the liquid $Ar$-$Xe$ mixture for all projectiles heavier than $^1H$ in a region of several $nm$ around the ion path [81]. The breakover point for boiling appears along the path of $^7Li$ when it decelerates below a certain energy per mass ratio. The superheating temperatures in the centers of the tracks calculated by this model start with 160 $K$ for $^7Li$ when the $Ar$-$Xe$ mixture is still in the liquid phase and reach more than 10 000 $K$ at the center of the $^{127}I$ track. This high temperature is assumed to lead – with certainty – to boiling in the next time step.

These enormous temperature values can simply be reproduced by converting the values for the average energy per atom in figure 5.6 to temperature values using the Boltzmann constant. Then the values span a range from minimal 1 $K$ at the lower $^1H$ curve up to more than 10 000 $K$ for the upper $^{127}I$ curve. These calculations do not allow us to neglect effects based on their thermodynamic conclusions, despite the fact that they were made without subtractions of energy that goes into scintillation. Thus, the data points for the scintillation ratios of the different ions and energies from chapter 4 are rearranged in section 5.4.

It has to be noted that excitation does not simultaneously mean heating. The excitation happens by lifting electrons into higher orbitals of the $Ar$ atoms or into the continuum (ionization). However, secondary electrons from ionization can not only excite the neighboring atoms, but their energy distribution also defines the electronic temperature in the bulk. The next step (compare subsection 5.2.2) is then the atomic temperature increase.

## 5.4 Rearrangement of the Results

Information from figure 5.6 can be used to arrange the experimental results in such a way that the effect on the NIR scintillation and thus the NIR-to-VUV ratio become clearly visible. To achieve this, the average values $\langle {}^{E}/_{N} \rangle$ are calculated from the ${}^{dE}/_{dN}$-curves versus position along the track and are used for the abscissa of the following plot 5.7.

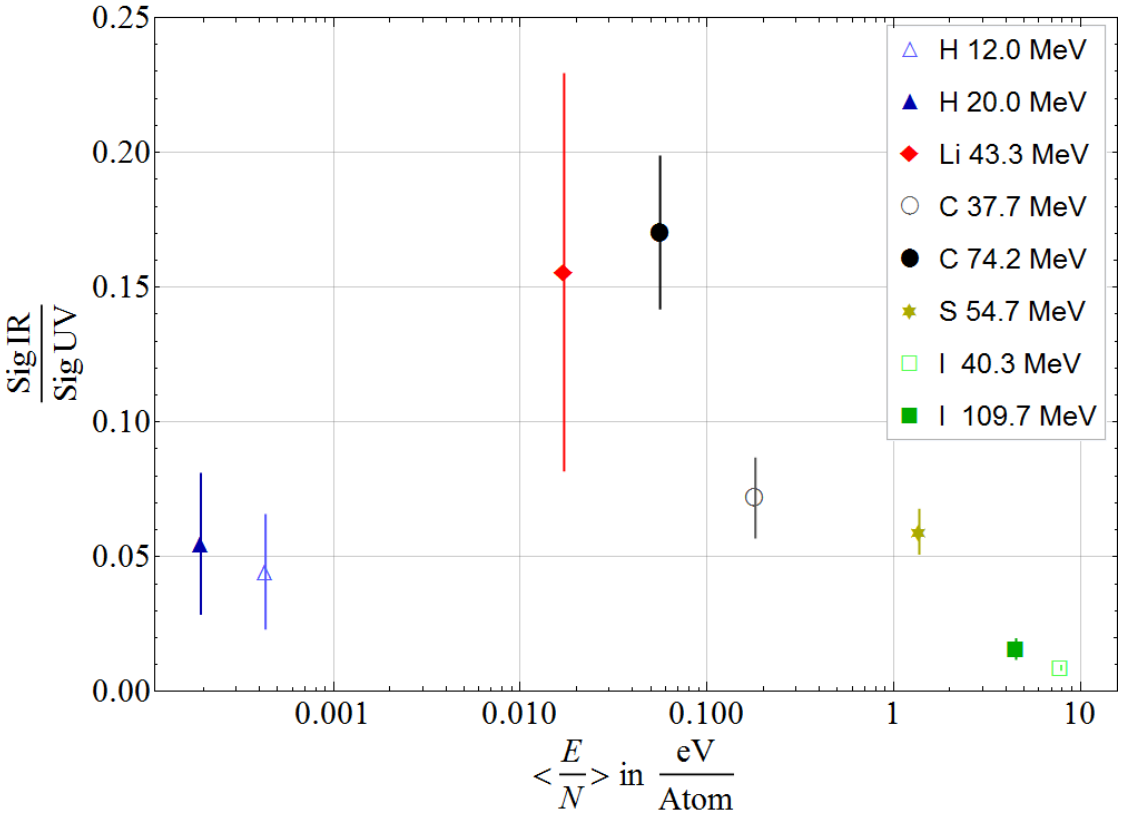


**Figure 5.7:** In this diagram the experimental results of the NIR-to-VUV ratios are plotted against the average of ${}^{dE}/_{dN}$ along the ion paths, the $\langle {}^{E}/_{N} \rangle$ values.

If the results for hydrogen are excluded (compare figures 4.1 and 4.2), the resulting diagram in figure 5.7 shows a linear decrease of the signal ratios with an exponentially increased average energy per atom $\langle {}^{E}/_{N} \rangle$.

The reason for the NIR-to-VUV ratios of both ${}^{1}H$ ions not to fit into the picture have not yet been clarified. It is possible that the excitation process in the medium might be different or the consideration of only the ${}^{dE}/_{dV}$-values is not enough. Regarding the protons themselves, they can be seen on one hand as ionized hydrogen atoms, not carrying a negatively-charged electron cloud. On the other hand they can be

described as single nuclear particles with positive unit charge. Then the difference to electrons is just their polarity and mass.

For the investigation of the protons' behavior, the next subsection compares the data of the ion-beam experiment with experiments performed with electron-beam excitation.

## 5.5 Comparison with Electron Excitation

The investigation of our group on the scintillation of liquid *Ar-Xe* mixtures started with electron-beam excitation. Since this kind of excitation is performed at low energies ($< 15\,keV$) these primary projectiles can be considered to have similar effects as the secondary electrons from heavier high-energy particles[12].

A NIR-to-VUV scintillation ratio for electrons can be calculated using the data of the absolute scintillation efficiencies in photons per $MeV$ from reference [53]. Whereas all signal ratios shown beforehand are bound to the conditions in the present experimental setup a correction[13] can be estimated for comparing ion data with electron data.

Figure 5.8 repeats the plot from figure 4.2, but includes a data point for electrons and uses an estimate of the absolute signal ratios for the ions, as data taken in the present thesis was not absolutely calibrated. The electrons do not continue the increase of the signal ratio of the heavier ions. Instead they are found at a similar value as those for the $^{7}Li$ and the high-energy $^{12}C$. It has to be stated that the NIR-to-VUV signal ratio for electrons was calculated by using the two absolute values for the scintillation efficiency of the NIR and VUV emissions in the liquid *Ar-Xe* mixture [53].

In the scope of the present thesis an energy-dependence test of the NIR-to-VUV scintillation ratio for electron-beam excitation had been carried out. Using a slightly different setup and a cathode ray tube for electron beam excitation[14] the scintillation ratios have to be corrected, too. The correction of the electron data could be made by adapting the data point that has the same parameters[15] as in the absolutely calibrated measurement in reference [53]. All electron energies denoted here are energies after the $SiO_2/Si_3N_4$ entrance foil, used for low-energy electron-beam experiments.

[12] The energy of secondary electrons reaches from below $1.8\,keV$ for the low-energetic $^{127}I$ ion to a maximum of $44\,keV$ for the high-energetic $^{1}H$ ion (see equation (1.3)).

[13] The correction takes into account the solid angles and detector sensitivities

[14] The same setup was used in the previous study by A. Neumeier [54].

[15] Electron energy and beam current of approximately $10.1\,keV$ and $1.3\,\mu A$, respectively.

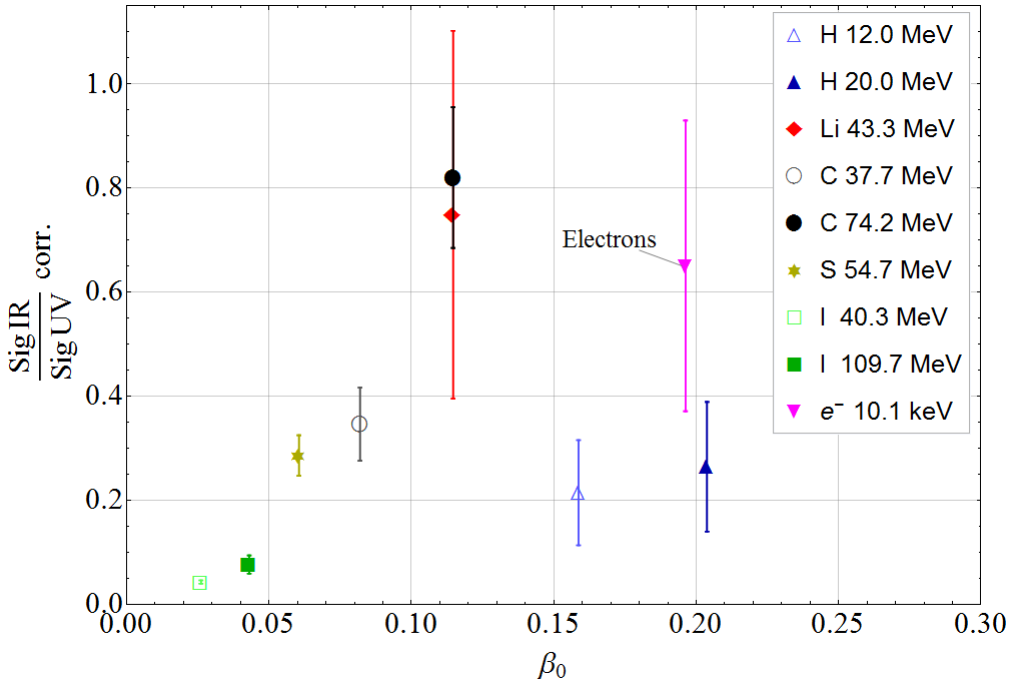


**Figure 5.8:** Corrected NIR-to-VUV ratio plotted against the initial projectile velocity, including a value for electrons from the work of A. Neumeier [53]. It can be seen that the electron value is taking its position at a higher NIR-to-VUV ratio than that for $^{1}H$ at similar $\beta_0$, but slightly lower than the ratio for $^{12}C$ with $74.2\,MeV$. For this comparison the signal ratios from the present experiment are corrected for solid angle and quantum efficiency of the PMTs. The error bar for electrons is derived from the uncertainties of their absolute scintillation efficiencies. The error bars for the ions represent the same relative uncertainties as in the previous diagrams. Additional errors due to the correction of the signal ratio of the ion data are not considered.

The NIR-to-VUV ratios in figure 5.9 show an increase with electron energy which is consistent with the trend that can be seen for the ion pairs with different energies. Note that the error bar of the value from A. Neumeier [53] derives from the errors of the absolute scintillation efficiencies as the statistical errors plotted for the data points in the electron measurment series are significantly smaller. To compare this variation with that of the ion values, the signal ratios are plotted against initial velocity $\beta_0$ again in figure 5.10.

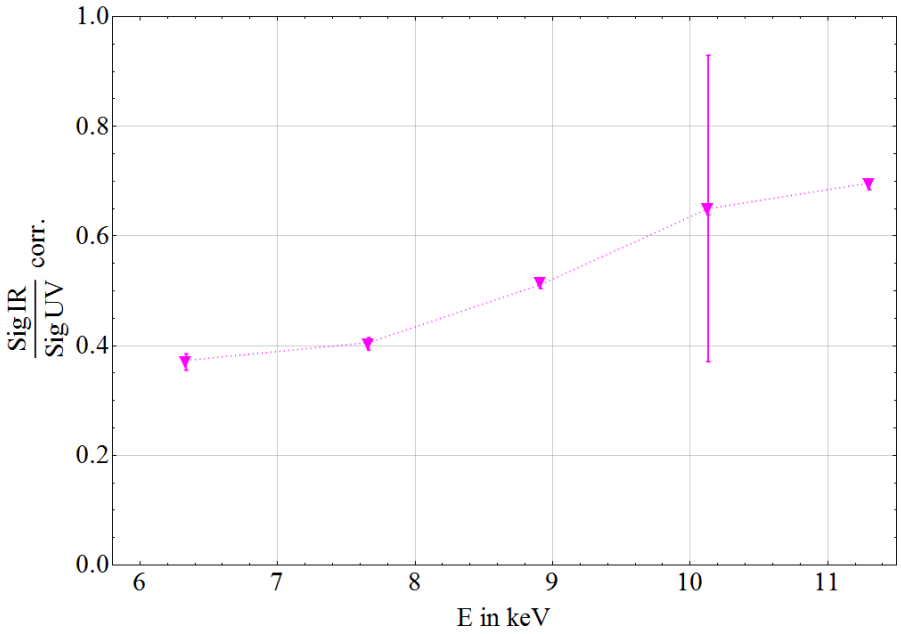


**Figure 5.9:** Corrected signal ratios of electrons for different electron energies in the liquid mixture. The correction is done by adapting the data points to agree with the absolutely calibrated value in [53] (data point with large error bar). Within the electron measurement series the error bars are in the size of the symbols. The dotted line is for guiding the eye. Note that the energy axis starts at 6 $keV$ electron energy behind the entrance foil.

The inserted electron data series in figure 5.10 shows a significant dependence of the scintillation ratio on initial velocity. The data points align in a similar way as the $^{12}C$ ions (37.7 and 74.2 $MeV$) and also the other heavy ions do. However, it should be noted that this is only a phenomenological consideration since the excitation mechanism of electrons is different to that of the ions, mainly because of the mass difference. On the other hand, secondary electrons generated by heavy ions in the $MeV$ scale and the directly injected electrons in this study have a very similar energy range on the $keV$ scale. Nevertheless, electrons do not form a track structure as heavy ions do, since the energy and momentum transfer happens at collisions of equal particles (scattering from valence electrons) or with significantly heavier nuclei (elastic scattering from atomic potentials) [77].

Finally it can be emphasized that a significant dependence of the NIR-to-VUV scintillation ratio on the incident particle type and particle energy could be determined. Both dependencies superimpose each other. This means that a one-to-one assignment of particle types solely using the scintillation ratio, as had been assumed up to now, is not possible. However, future studies including detector-relevant

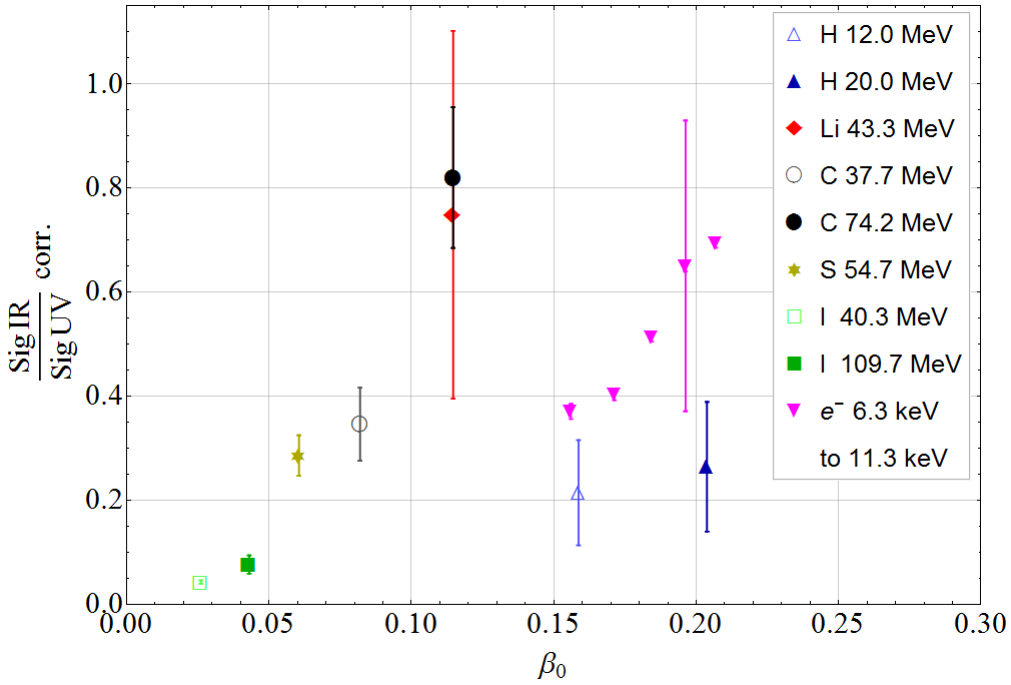


**Figure 5.10:** Corrected NIR-to-VUV signal ratios for all ions and electron data plotted against the initial velocity of the respective projectile. All electron data points can be assumed to have similar uncertainties. The electron data point at $\beta_0 \approx 0.20$ has its large error bar due to the transfer of the data from the experiment of A. Neumeier. The statistical errors plotted for the complete electron measurement series are of the size of the symbols.

particles — gammas, neutrons, muons, etc. — can lead to the use of the investigated scintillation ratio as an additional discrimination parameter.

Furthermore an important influence of heavy particle tracks on the target material was found. For liquid rare gas particle detectors at least, but also for other dense detector materials, it must be assumed that single heavy particles can cause significant heating as well as phase transitions and thus affecting the scintillation processes. This is especially true for high LET values (Bragg peak) at the end of the particle path. At that point the ranges of the secondary electrons and, therefore, the volume in which the energy is deposited are drastically decreased. Thus a very small amount of target material has to deal with large energy transfers.

# Chapter 6

# Aspects Concerning Detector Physics on the *keV*-Scale

As explained in the discussion in chapter 5, thermodynamic processes have to be taken into account for the scintillation induced by high-energy heavy ions. The next step towards a particle detector is to use low-energy projectiles. Such projectiles would be expected to appear after nuclear collisions with dark matter candidates, e. g. WIMPs. However, the energies of the projectiles are supposed to be much lower, in the range of 10 to 100 $keV$ [101, 18].

The shift from high to low-energy recoil particles can be demostrated by the calculation of the energy deposition along the path for recoil particles in the liquid $Ar$-$Xe$ mixture.

## 6.1 From Electronic to Nuclear Stopping

For low-energy particles the electronic stopping $^{dE}/_{dx}|_{el}$ is low compared to nuclear stopping $^{dE}/_{dx}|_{nuc}$ induced by nuclear recoils. In figure 5.3 the linear energy transfer (LET) of the investigated (heavy) ions was shown as the total stopping power $^{dE}/_{dx}|_{total}$ only, since the electronic stopping dominates above certain energies for the high-energy particles[1].

[1]The fraction of the nuclear stopping component is crossing the 1 % threshold for $^{32}S$ when the projectile energy is decreasing below 5.50 $MeV$. For the $^{1}H$ ion crossing occurs at 13.0 $keV$ according to SRIM calculations. Only for the injected heavy $^{127}I$ the threshold is already crossed at 70.0 $MeV$.

In the present chapter SRIM-calculations are performed for the expected $Ar$ recoil particle as it was done before for the high-energy ions ($MeV$). Since the energies are assumed to be in the order of $100\,keV$, this energy is used. In contrast to the high-energy particles, the $100\,keV$ energy range is dominated by nuclear stopping rather than electronic stopping. Therefore, in figure 6.1 both stopping powers and their sum are plotted against the range of the particle. It has to be noted that the use of the term LET could be misleading[2] when it comes to discrimination between different kinds of stopping processes. Thus, in this chapter, the energy dissipation will explicitly be designated by the values in the following formula:

$$\left.\frac{dE}{dx}\right|_{el} + \left.\frac{dE}{dx}\right|_{nuc} = \left.\frac{dE}{dx}\right|_{total} \tag{6.1}$$

The total stopping power ${}^{dE}/_{dx}|_{total}$ consists of the electronic component ${}^{dE}/_{dx}|_{el}$, which is dominated by electron recoils leading directly to excitation and ionization, and of the nuclear component ${}^{dE}/_{dx}|_{nuc}$, which is due to nuclear collisions. Radiative stopping power and a stopping component due to nuclear reactions are neglected.

Figure 6.1 shows a nearly constant value of the total stopping power over a long range and a fast drop in the last $50\,nm$. The electronic stopping starts at approximately 30 % of the total value and is nearly linearly decreasing. Nuclear stopping, on the other hand, is increasing until it reaches its late peak about $50\,nm$ before the projectile is stopped on average. This peak corresponds to an energy of $25\,keV$ for the $Ar$ recoil particle. The mean range for $100\,keV$ $Ar$ atoms is $243\,nm$ and the minimum of the electronic stopping fraction can be extracted from the data to be $\sim 6\,\%$ at $\sim 150\,eV$. Below this energy the electronic stopping fraction is rising again due to the fast decrease of the nuclear stopping power but not above $\sim 7\,\%$.

Another aspect of low-energy recoil particles is their charge state. The effective charge $ze$ of an ion traveling through a medium can be expressed as a function of its velocity $\beta = {}^{v}/_{c_0}$ and charge number $Z$ [103, 75]:

$$ze = Z \cdot e\left(1 - \exp\frac{-125\beta}{\sqrt[3]{Z^2}}\right). \tag{6.2}$$

The calculation reveals a value below one elementary charge ($e$) for $100\,keV$ $Ar$. Thus, it has to be treated as a neutral atom.

[2] A term that is used analogously as LET for ionization events, is “non-ionizing energy loss” (NIEL) [102].

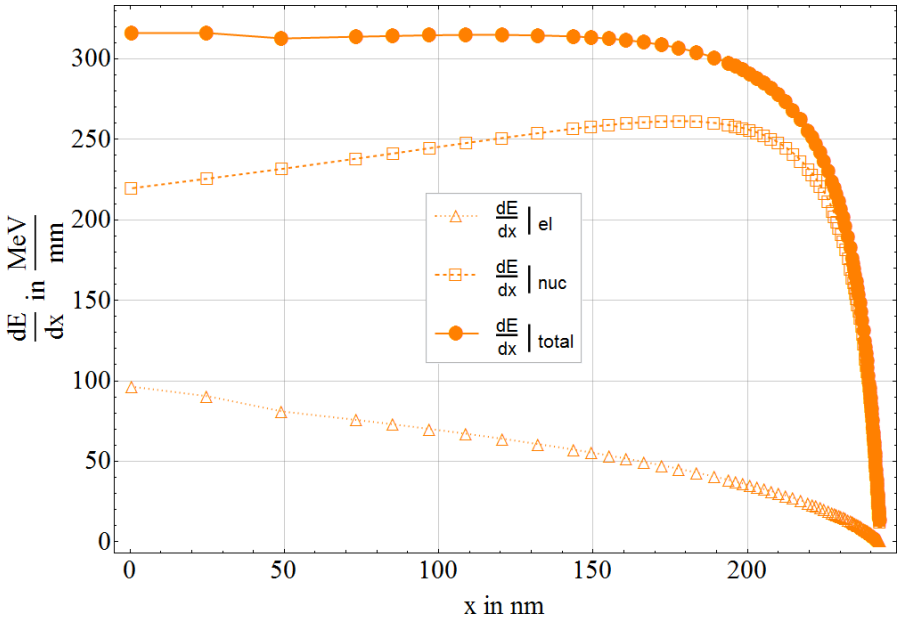


**Figure 6.1:** In this diagram the stopping power values for 100 $keV$ $Ar$ atoms can be seen for both the electronic and nuclear stopping, respectively, as well as their sum. These SRIM simulation values are plotted against the range of such a recoil particle in the liquid $Ar$-$Xe$ mixture. Data points are connected to guide the eye.

## 6.2 Electronic Stopping and Its Limits

Using the same calculations as for high-energy particles the applied concept is certainly reaching a limit if it comes to track dimensions. Formula (1.6) makes a statement on the transverse energy range of the secondary electrons. Its results depend only on the $E/m$ value of the projectile. One major drawback here is that the decreasing ratio of electronic stopping is **not** taken into account. The outcome of the calculation is summarized in figure 6.2.

Figure 6.2 has to be interpreted carefully. The formula[3] (1.6) does neither take the different stopping processes into account nor the discrete distances of the $Ar$ atoms[4]. As seen in figure 6.2, the transverse dimensions of the core of the particle track calculated are completely below the average atomic distance.

[3]The formula was derived for projectiles between 0.1 and 100 $MeV/u$ and is now used for input values of 0.0025 $MeV/u$ and below. This means an extrapolation of about 2 orders of magnitude below the ensured valid range.

[4]Using the density of liquid $Ar$ a mean distance of $\sim 360\,pm$ between the atoms can be calculated.

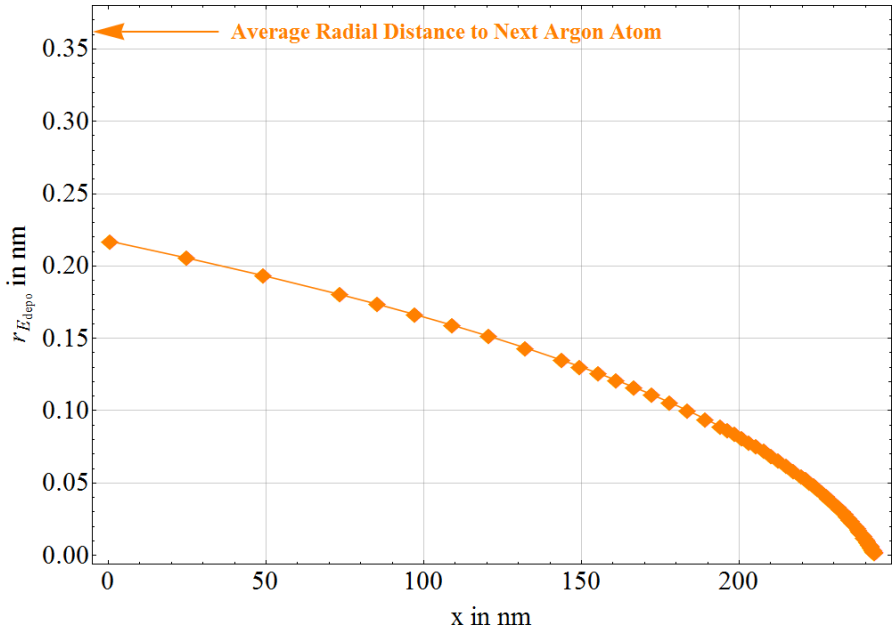


**Figure 6.2:** The calculated range $r_{E_{depo}}$ of energy deposition ($66\,\% E_{depo}$) transversal to the projectile path $x$. The average distance to the next $Ar$ atom is marked by the arrow. Note that both axes use the same unit but have different scales. Data points are connected to guide the eye.

However, the energy range due to secondary electrons could be even more restricted due to the small fraction of $^{dE}/_{dx}|_{el}$ not considered in the formula. In addition, it has to be considered if the small amount of atoms[5]require a different kind of calculations. In the case of a highly scintillating rare gas also the missing consideration of the energy that goes into light emission has to be mentioned.

Even the formula (1.3) for the maximum energy of the secondary electrons is reaching its limit. This formula states "the classical kinematic value for the maximum energy that an ion can transfer to a *free* electron" [76]. For high-energy ions the results are in $keV$ range and the binding of the electrons is negligible. However, at low projectile energies, at least $\sim 400\,keV$ would be needed to reach the $W$ value[6] for liquid $Ar$: $W = 23.6\,eV$ [104]. The large energy difference originates in the mass difference between an electron and an $Ar$ projectile nucleus, since the velocity is the significant quantity. From kinematics emerges that an $400\,keV$ $Ar$ atom has a velocity of $\sim 5 \cdot 10^{-3}$ the speed of light whereas the electron – if in rest before – has a final velocity of twice the atom velocity after a collision

[5] On a path of $243\,nm$ length $\approx 672$ $Ar$ atoms can be considered.

[6] The $W$ value is the average energy necessary to produce an electron-ion pair, in contrast to the theoretical value of the ionization energy for an atom.

with a maximal energy transfer. However, at low energies the motion of electrons in their orbitals can play a significant role for the collision processes and their energy straggling.

The transverse dimensions of the track can obviously no longer be calculated using a continuous energy deposition: Due to the *discrete* distances between the atoms, the energy range $r_{E_{depo}}$ of the secondary electrons may no longer be expressed by a *continuous* function of the $E/m$ value of the projectile. A more probability-related function might be used to take into account the stochastic nature of the single electron recoils, leading to two possible results for a single collision: For higher energy the next atoms can be reached by the electrons, for less energy the electrons may return to their initial atom on the projectile path.

Nevertheless, using the known values, a zero-order calculation of the energy deposition per atom can be made. Therefore, the projectile energy of $100\,keV$ is distributed evenly over the $\sim$ 700 atoms on the path. If the fraction of scintillation energy is subtracted – 15.3 % for a liquid $Ar$-$Xe$ mixture [53] – an energy dissipation of $\langle E/N \rangle \sim 130\,eV/Atom$ can be found. Compared with the data in figure 5.7 this $\langle E/N \rangle$ value is significantly larger than the $\sim 10\,eV/Atom$ of the $^{127}I$ ions. Thus, a much lower NIR-to-VUV scintillation ratio would be expected, if the $100\,keV$ $Ar$ atoms would follow the trend of the other heavy ions in figure 5.7. Another way to perform the calculations would be to include the average fraction (of roughly 17.5 %) of the electronic stopping $dE/dx|_{el}$ along the path. This leads to only $\sim 22\,eV/Atom$ of ionizing energy, still above the value for $^{127}I$, however it would raise the question, how the rest of 82.5 % of nuclear stopping power is deposited in the medium.

Since the electronic stopping $dE/dx|_{el}$ is weak and the secondary electrons can not contribute any more to a transverse energy distribution, the next question introduced is about the effects of nuclear stopping $dE/dx|_{nuc}$.

## 6.3 Effects of Nuclear Stopping

As seen in figure 6.1, the energy deposition will occur mainly by nuclear recoils. Thus, a large part of the energy will be deposited onto the nuclei, rather than by excitation or by ionization processes. The collisions of the nuclei will initiate a wave travelling through the medium rather than a large displacement of $Ar$ atoms[7].

[7] The mass of the projectile is the same as the recoil particle.

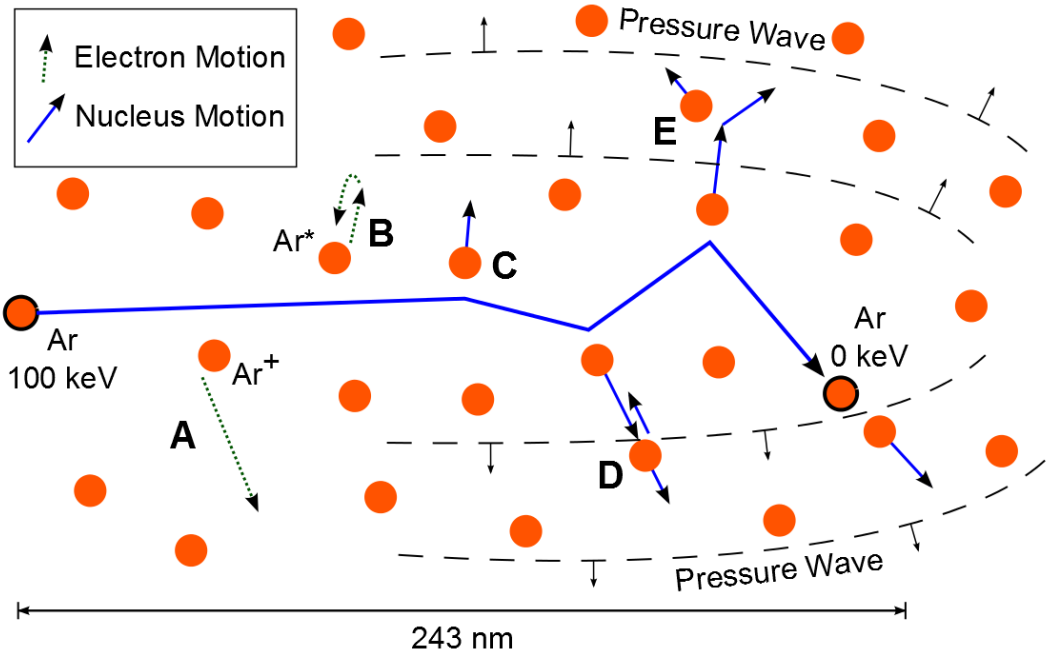


**Figure 6.3:** Stopping processes at the end of the track. This schematic drawing gives an overview over possible processes in the last layers of $Ar$ atoms in the detector liquid. The excitation particle in this case is an $100\,keV$ $Ar$ atom. Following its path through the medium several processes are depicted, including ionization (A) and excitation (B) due to electron recoils as well as nuclear recoils (C) and secondary collisions (D, E) creating a pressure wave (description in the text). This graphic is not to scale, i. e. the number of atoms is not appropriate to the length scale given.

Figure 6.3 depicts some of the processes considered for the last collisions of the projectile. At the end of the track the stopping power is dominated by the nuclear contribution (see figure 6.1). Thus, only the minor part will excite or ionize $Ar$ atoms. As it can be calculated using equation (1.3), the maximal energy transferred to an electron by a $100\,keV$ $Ar$ atom is $\approx 5.5\,eV$. This is not enough energy to ionize either an $Ar$ ($15.8\,eV$) nor a $Xe$ atom ($12.1\,eV$). Also the electron energy and motion in the orbital plays a role at such low excitation energies.

The major part of the stopping happens by the nuclear stopping power ${}^{dE}/_{dx}|_{nuc}$, i. e. by nuclear collisions. Each nuclear collision happens at a certain angle and the momentum transfer is dependent on this angle. It is assumed that secondary projectiles are soon involved in tertiary collisions, and so on. Such collision cascades need a more detailed model [105, 106], still depending on the distribution of the momentum transfers, the generation of a pressure wave and heating are expected.

## 6.4 Estimate of the Track Dimension in Zero Order

Without doubt, measurements and simulations have to be performed for future considerations. Nevertheless, an estimate of the track produced by nuclear collisions shall be calculated here. The following assumptions are made:

- The energy is evenly distributed between all atoms in the involved volume in such way, that all these atoms have exactly an energy corresponding to their specific heat of vaporization at a certain point in time[8].
- For the time-of-flight calculation the deceleration is taken to be constant[9] during the whole time from the known initial velocity until the stopping.
- The velocity of the proceeding wave in the medium is considered to be equal to the speed of sound in liquid $Ar$.
- Superheating is neglected and an instant phase transition is assumed.

Using the specific vaporization energy of $67\,{}^{meV}/_{Atom}$ and the fact that the boiling of the $Ar$-$Xe$ mixture is enough to suppress a NIR emission from the Wannier-Mott state, i. e. no further heating is taken into account, a number of atoms can be deduced, that would be influenced by a $100\,keV$ $Ar$ recoil particle: $\sim 1.5 \cdot 10^6$. Before an expansion, this would be equal to a volume of $\sim 7 \cdot 10^{-23}\,m^3$ and leads to an energy density of $\sim 2.3 \cdot 10^8\,{}^{J}/_{m^3}$.

The known penetration depth and the assumption of a cylindrical track due to the nearly constant ${}^{dE}/_{dx}|_{total}$ results in a radius of $\sim 10\,nm$. To stay consistent with the track definition that leads to equation (1.6), only 66 % of the volume have to be counted as core. As the path length is not influenced, this results in a track radius of $\sim 8\,nm$. The energy density is not affected since the energy is assumed to be evenly distributed. Using the speed of sound as an estimate of the propagation speed, this leads to $\sim 1.2 \cdot 10^{-11}\,s$ for the evolution of the whole track, core and halo. The power density can be estimated to be of the order of $\sim 2.0 \cdot 10^{19}\,{}^{W}/_{m^3}$, a similar value as for the core of the track generated by the ${}^{12}C$ ions (compare table 5.1).

The time of flight of the $100\,keV$ $Ar$ atom was derived assuming a constant deceleration from the known speed (equation (1.4)) to 0. The time of flight of

[8] There will be at least one point in time when the average energy of each atom involved will be equal to the heat of vaporization.

[9] This is a valid assumption, see the behavior of the total stopping power shown in figure 6.1.

$7 \cdot 10^{-13}\,s$ is an order of magnitude shorter than the estimated evolution time of the track. Thus, in contrast to the high-energy heavy ions (see subsection 5.2.2) the track – with the parameters of the assumptions – is forming **after** the flyby of the low-energy $Ar$ projectile.

Once again, it has to be stated that these are only rough estimations based on simple assumptions and neglecting a continuously varying distribution of energy deposition. Directly around the path the energy and power densities are much higher than calculated here. Also a temperature rise far above the boiling temperature can be assumed in the beginning after the projectile has passed, if the 'nature' of the heat equations and the time scales (compare subsection 5.2.2) are taken into account. It should be noted that before boiling, a stage of superheating will occur.

## 6.5 Relevant Questions Concerning Detector Physics

In this thesis, the question has been asked how the excitation due to *low-energy* recoil particles in the $keV$ range occurs. According to SRIM calculations, the bulk of the stopping is due to the nuclear stopping power $^{dE}/_{dx}|_{nuc}$ [95] (compare figure 6.1), i. e. due to nuclear collisions. Nuclear stopping power is, per definition, not taking into account any interaction with the electrons of the target atoms. Consequently, excitation due to low-energy particles has to be treated differently than ionization and excitation induced by high-energy particles [104] or solely electronically interacting radiation like gamma particles [107]. High-energy particles can still interact with a high electronic stopping, leading to excitation and ionization. The low-energy particles, which interact only with electrons, are not directly comparable to low-energy recoil particles that primarily interact via nuclear stopping. For low-energy projectiles ($100\,keV$) the nuclear stopping $^{dE}/_{dx}|_{nuc}$ is strongly dependent on the projectile mass ($\sim 0.1\,^{MeV}/_{mm}$ for $^{1}H$, $\sim 1\,000\,^{MeV}/_{mm}$ for $^{127}I$) while the electronic stopping $^{dE}/_{dx}|_{el}$ is nearly the same for all atoms ($\sim 80\,^{MeV}/_{mm}$) in liquid $Ar$ [95].

Although the power density of $\sim 2.0 \cdot 10^{19}\,^{W}/_{m^3}$ estimated in section 6.4 is not as high as that for the $^{127}I$ ion (compare table 5.1), which caused a strong decrease in NIR light assumably due to boiling, this power density is not low either. Thus, a detailed study of this effect can lead to a better understanding of the processes of light emission in liquid rare gases and other media.

Considering those large power densities, one major advantage of liquid rare gases in particle detectors is their durability against irreversible modifications on a chemical level. The bulk of the scintillator is present in atomic form, since only excited rare gas atoms can build molecules. And even if these molecules are

destroyed by a single event of high power density, the rare gas excimers would reform at the next excitation after a sufficient time of cooling[10]. Thus, high power densities can only appear as an issue for molecular substances used as scintillators, e. g. organic compounds. In such a case, an event-intensity dependent aging could be considered in relation to the kilogram-year exposure for an estimation of the stability of organic scintillators.

[10]Cooling times can vary in a wide range between $10^{-12}\,s$ and $10^{-3}\,s$ as discussed in subsection 5.2.2.

# Chapter 7

# Outlook

The experiments presented in this thesis revealed a particle and energy dependence of the near-infrared-to-vacuum-ultraviolet (NIR-to-VUV) scintillation ratio of the liquid $Ar$-$Xe$ mixture. The NIR part is strongly reduced by heavy-ion excitation due to high energy-deposition density.

The comparison of the dependence of the scintillation ratios on the particle velocities (figure 5.10) shows that the results for $^{1}H$ ions are very different from those of the other values obtained for the heavier ions $^{7}Li$, $^{12}C$, $^{32}S$, and $^{127}I$. These heavy ions tend to arrange along a straight line, rising with increasing projectile velocity. However, the lighter protons injected with higher velocities have smaller NIR-to-VUV ratios. The scintillation ratios induced by the electrons are also lower than expected from the arrangement of the heavier ions, but they are not as low as those for protons (see figure 5.10). The reason for the discrepancy between the heavy ion trend and the scintillation ratios of the lighter particles is not yet clarified.

Due to this off-trend behavior as well as the superposition of the particle type and particle energy dependences, the NIR-to-VUV scintillation ratios are not suitable to be used as a single particle discrimination variable. However, the scintillation ratio can be expected to be used as an additional parameter for the evaluation of data obtained by particle detectors.

In the following, several future studies are suggested.

## 7.1 Detector Experiments

For dark matter search detector-oriented experiments are interesting. The detection would then have to be customized to real single-event measurements, in contrast

to the test experiments for LET dependence performed in this thesis by the use of continuous ion beams of a particle accelerator. These detector-oriented experiments would include detector-like setups for measuring neutrons, muons, gamma particles, and also electrons as relevant background radiation [7, 10].

A model experiment imitating a 'real' detector could be performed by simulating recoiling $Ar$ atoms due to interaction by WIMPs, using e. g. neutron collisions in the medium. Concerning a dark matter detector, the neutrons generated should lead to recoil energies in the order of 1 to 100 $keV$, the energy range which is considered for WIMP recoils [101, 18, 19]. Neutrons could be produced in a controlled way by a particle accelerator[1]. Neutrons with a defined energy could then be used to investigate the scintillation yields in the $keV$-range, as described in chapter 6. By using a light detection setup including a spectral resolution, the influence on the scintillation mechanism could be studied.

Choosing an adequate larger target cell, experiments using cosmic muons as excitation particles should also be possible. Another approach including alpha, beta, and gamma particles is the use of radioactive sources in a dedicated setup to excite the liquid $Ar$-$Xe$ mixture.

The optimal solution would be the design of a multi-purpose target cell that allows the observation of different kinds of excitation by fixed photomultiplier tubes (PMTs). The calibration method could for example be similar to the one used in the present thesis. The detector mounting can be optimized by having a cylindrical target cell with the PMTs at the top and at the bottom, facing each other through the target medium. This would allow a larger solid angle and the use of several PMTs of each kind, IR and UV, respectively.

As the particle energies are drastically lower in detector-like experiments than in the accelerator experiments in this thesis, the energy deposition is changing due to the transition from electronic to nuclear stopping. For example, for a low-energy sulfur projectile the electronic contribution to the stopping power is 34 % at 100 $keV$, 12.0 % at 10 $keV$, and only 6.9 % at 1 $keV$, according to SRIM calculations [95]. Thus, the volume of the tracks can not be calculated any more via the range of secondary electrons, as described in chapter 6, but nuclear recoils [96] and an elastic thermal spike model [105, 106] could be taken into consideration for a new approach towards track volumes and power densities in the regime of nuclear collisions.

Besides a realistic detector test the following questions concerning the scintillation of an $Ar$-$Xe$ mixture should be addressed.

[1] A ${}^{11}_{5}B$ beam onto a ${}^{1}_{1}H$ target produces neutrons by nuclear reactions.

## 7.2 Investigations of the Argon-Xenon Mixing Ratio on a Linear Scale

This study was made under the assumption[2] that a volumetric fraction of $10^{-5}$ of $Xe$ is optimal for both, the NIR and the VUV emissions, in terms of intensity in photons per MeV. However, the intensities change rapidly with the order of magnitude of the $Xe$ amount (see figure 1.4). Thus before designing an up-scaled detector prototype a study on the $Ar$-$Xe$ mixing ratio should be performed.

Such a study should contain the investigation of a more precise optimal mixture ratio[3], where the NIR emission of the detector liquid is maximal, and – if feasible – also of the true mixture ratio in the liquid, since the mixing ratio is only known from the gas phase before condensation. The fact that rare gases have to be purified leads to a continuous cycling[4], including evaporation towards the gas system and recondensation in the target cell. Different gas system and target cell sizes could lead to different mixing ratios in the liquid phase (compare paragraph 2.2.1). This is important, if the volume ratio of detector and target cell is drastically altered and if a specific mixing ratio within a certain precision has to be reached. If it would be necessary but not possible to keep a precise mixture ratio constant, an intrinsic change of the scintillation ratio due to a varying $Xe$ content would result. In this case, investigations using a linear variation of the mixing ratios are crucial for a large detector setup. Also the homogeneity of the mixture should be investigated for larger target cells.

Concerning the linear variation of the $Xe$ admixture a more precise measurement of the mixing ratio is needed, a demixing measurement over time could be performed additionally. A change in the mixing ratio can especially be assumed for higher concentrations of $Xe$ due to recondensation as well as for longer time scales, since an operational detector needs not only large amounts of target material but also sufficiently long running times.

For all those measurements a stable source of excitation is necessary. Thus an electron excitation or the use of long-lived radioactive sources is recommended due to their predictability.

[2] An experiment for the determination of the exact optimal mixing ratio had been planned previously to the accelerator experiments but was canceled due to an unexpected laboratory closure.

[3] The optimal volumetric fraction of $10^{-5}$ of $Xe$ was found in a study in which the $Xe$ amount was only varied by factors of 10 [54].

[4] The mixture could not be pumped in the liquid phase due to the purification that uses a getter alloy at $670\,K$.

## 7.3 Ion Beam Experiments with Wavelength Resolution

Since the emission features in the NIR and in the VUV are known, a linear scale study of the volumetric fraction of $Xe$ could be made by integrating the whole NIR and VUV regions, respectively. However, since the liquid $Ar$-$Xe$ mixture was only investigated wavelength resolved by electron beam excitation, it might be advisable to use a wavelength-resolving setup to reveal the changes in the excitation and energy transfer processes for other excitation particles. This was already done by M. Hofmann [74] for pure liquid $Ar$ with a selection of heavy ions. Such measurements would in addition allow time-structure measurements at certain selected wavelengths if a pulsed excitation source is used.

## 7.4 Study of Timing

Time-structure measurements could be another interesting experiment since the singlet-to-triplet ratio was found to change with the injected particle type in accelerator experiments using pure liquid $Ar$ [74]. Until now the liquid $Ar$-$Xe$ mixture was only investigated concerning its time structure with electron-beam excitation (and only for one mixing ratio) [53]. The question might be asked if a particle discrimination based on the singlet-to-triplet ratio could also be possible in the $Ar$-$Xe$ mixture.

Time structure measurements could also help to determine some of the time periods involved in the heating process within the heavy ion tracks in the specific liquid mixture. These parameters could then be used in simulations on the microscopic scale for understanding the underlying processes of the heating in combination with the excitation. Such simulations would require to emulate the energy transfer from the incident primary particle to the secondary electrons as well as to nuclear recoils. An example of such a kind of simulations of the energy transfer processes can be found in [96, chapter 3]. Therein sophisticated calculations were implemented to investigate the scintillation processes in $CaWO_4$-crystals. As outlined in subsection 5.2.2, some of the processes overlap in time and it would especially be interesting to see, how the excitation in the very small volumes at the end of the particle tracks takes place, in time and in space. Also the transition from electronic to nuclear stopping should be taken into account at the lower energies of the expected WIMP-induced recoils.

One helpful way could be the implementation of the numerical solution of heat diffusion equations like in the so-called inelastic thermal spike (i-TS) model. The

i-TS model was developed by M. Toulemonde et. al [100] for calculations of thermal spikes in solids, modified by ion beam irradiation. In contrast to the liquid rare gas mixture investigated in the present thesis, solids can be studied by detailed tests after the irradiation and modifications of the bulk medium at the tracks can be found [100]. These modifications can provide information on the spatial distribution of the excitation on the nanometer scale. Liquids are not suitable for a subsequent investigation of this kind and an in situ imaging with adequate spatial resolution is technically challenging. However, with the use of simulations this obstacle can be overcome and could bring thermodynamics and particle-physics issues together.

# Appendices

# Appendix A

# Properties of the Rare Gases Argon & Xenon

For the preparation of the $Ar$-$Xe$ mixture as well as for calculations and simulations a variety of physical properties are needed. This appendix shows a selection of properties of gaseous and liquid $Ar$ and $Xe$, respectively, important for this thesis. It has to be noted that many of these properties are depending on pressure and temperature. Thus for detailed calculations, especially if a wide range of temperature and pressure is covered, the use of appropriate formulas should be considered [108, 109, 110, 111].

The phase diagram of $Ar$ is depicted in figure A.1. The consideration of the different phases is important for keeping the target cell filled with the mixture in the liquid phase below $1\,bar$ ($= 1\,000\,hPa$). It is seen that the temperature range below $1\,bar$ is very narrow, thus making demands on the setup.

| | $Ar$ | $Xe$ | |
|---|---|---|---|
| Atomic Mass | $39.948\,u$ | $131.293\,u$ | [112] |
| Density of Gas $\rho_{gas}$ (at $273\,K$) | $1.784\,{}^{kg}/_{m^3}$ | $5.897\,{}^{kg}/_{m^3}$ | [112] |
| Specific Heat Capacity $c_p^{gas}$ (Gas, at $T_B$) | $565.8\,{}^{J}/_{kg\cdot K}$ | $175.1\,{}^{J}/_{kg\cdot K}$ | [109] |
| Thermal Conductivity $\kappa_{gas}$ (Gas, at $273\,K$) | $16\,{}^{mW}/_{K\cdot m}$ | $5.1\,{}^{mW}/_{K\cdot m}$ | [108] |
| Boiling Temperature $T_B$ | $87.302\,K$ | $165.05\,K$ | [110] |
| Specific Heat of Vaporization $h_B$ (at $T_B$) | $161.1\,{}^{kJ}/_{kg}$ | $95.59\,{}^{kJ}/_{kg}$ | [109] |
| Density of Liquid $\rho_{liquid}$ | $1\,395.4\,{}^{kg}/_{m^3}$ | $2\,942\,{}^{kg}/_{m^3}$ | [113] |
| Specific Heat Capacity $c_p^{liquid}$ (Liquid, at $T_B$) | $1\,117\,{}^{J}/_{kg\cdot K}$ | $339.3\,{}^{J}/_{kg\cdot K}$ | [109] |
| Melting Temperature $T_M$ | $83.9\,K$ | $161.4\,K$ | [110] |
| Specific Heat of Fusion $h_M$ (at $T_{TP}$) | $28.0\,{}^{kJ}/_{kg}$ | $13.8\,{}^{kJ}/_{kg}$ | [109] |
| Triple Point Pressure $p_{TP}$ | $68.7\,kPa$ | $81.7\,kPa$ | [113] |
| Triple Point Temperature $T_{TP}$ | $83.81\,K$ | $161.40\,K$ | [113] |
| Speed of Sound $c_S^{liquid}$ (Liquid, at $T_B$) | $838.3\,{}^{m}/_{s}$ | $643.1\,{}^{m}/_{s}$ | [109] |
| $W$-Value (Average Energy for Ionization) | $23.6\,eV$ | $15.6\,eV$ | [104] |
| $W_{ph}$-Value (Average Energy for Photon Creation) | $19.5\,eV$ | $14.7\,eV$ | [104] |

**Table A.1:** Selected Properties of Argon and Xenon. If not noted otherwise, all values are valid at standard pressure $1013\,hPa$.

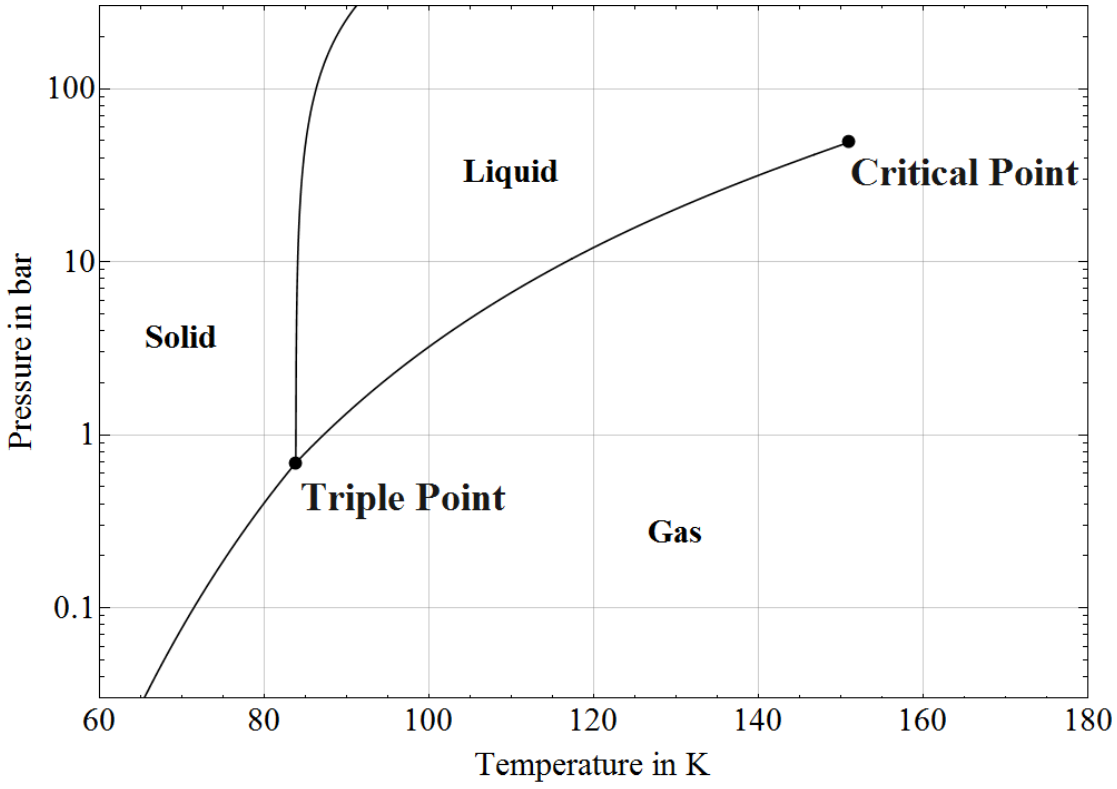


**Figure A.1:** Phase diagram of $Ar$ with logarithmic pressure axis showing the interesting region of the triple point and the critical point of pure $Ar$. Note that the temperature range for liquid $Ar$ is very narrow at $1\,bar$. The data for this plot is taken from [110].

For continuous circulation including different phases of a mixture, segregation effects have to be considered. If distinct substances have different solubilities in different phases, a passing gas flow can lead to a liquid-gas extraction of one component into the liquid. In process engineering, the binary phase diagram is used to depict this issue.

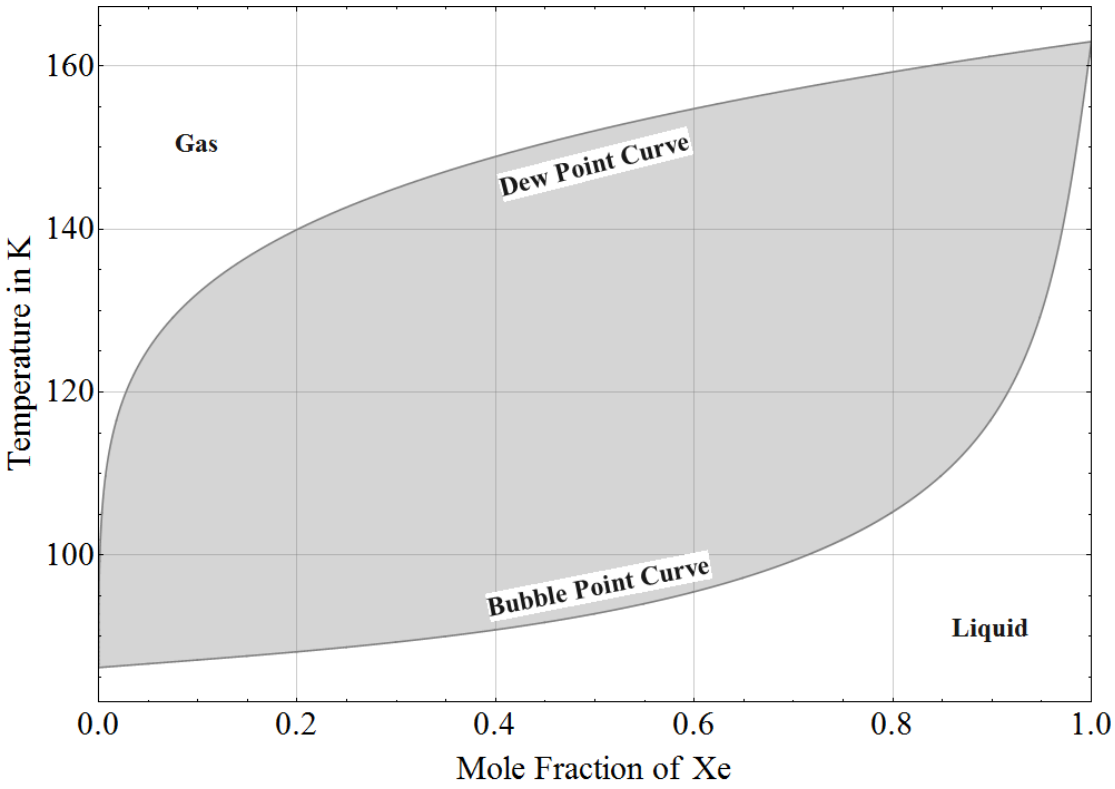


**Figure A.2:** Binary phase diagram for a $Ar$-$Xe$ mixture. This plot shows how segregation occurs because of different solubilities in the gas and in the liquid phase at the same temperature. At a specific temperature between the boiling points of $Ar$ (intersection of the curves at left axis, 0 % $Xe$) and $Xe$ (intersection on the right, 100 % $Xe$) the gray shaded area excludes forbidden mixing ratios. Data from [111]

Figure A.2 is the binary phase diagram for $Ar$-$Xe$ mixtures (mole fractions from 0.0 to 1.0). The gray-shaded area denotes the parameter space – mole fraction of $Xe$ and temperature – in which no mixtures exist. This gap starts at the boiling temperature of $Ar$ and ends at the boiling temperature of $Xe$. The dew point curve and the bubble point curve are the borders of this area. For example, a mixture at 120 $K$ would tend to a fraction of $Xe$ of about 0.05 in the gas phase while the liquid phase would have a fraction of about 0.9 of $Xe$. This

behavior is used in segregation processes, by removing the phase with the increased fraction of the wanted component.

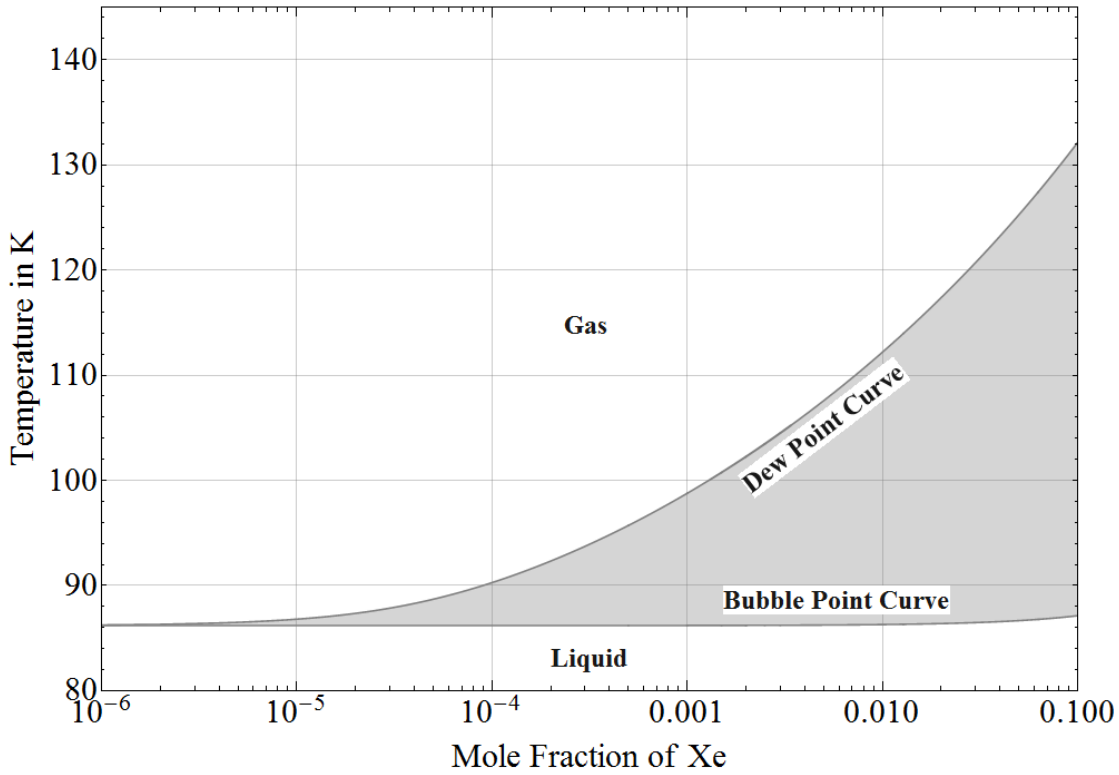


**Figure A.3:** Detail of the binary phase diagram A.2 for the $Ar$-$Xe$ mixture with a logarithmic ratio-axis for the $Xe$ concentration. Data from [111].

The cutout of the binary phase diagram in figure A.3 uses a logarithmic axis for the (mole) fraction of $Xe$ to emphasize the increasing concentration gap. This gap, confined by the dew point curve and the bubble point curve, separates the distinct mixing ratios in the gas and in the liquid phase at the same temperature.

# Appendix B

# Stopping Power Curves on a Linear Scale

The stopping powers of the various ions used are of particular interest in this thesis. However, for comparison of the different stopping powers in one single diagram logarithmic axes have to be used. The stopping power curves in this appendix are plotted in linear diagrams to get an undistorted view. Especially for $^{32}S$ and $^{127}I$ the 'shift' of the Bragg peak out of the target cell ($Ti$ entrance foil at $x = 0$) can be seen.

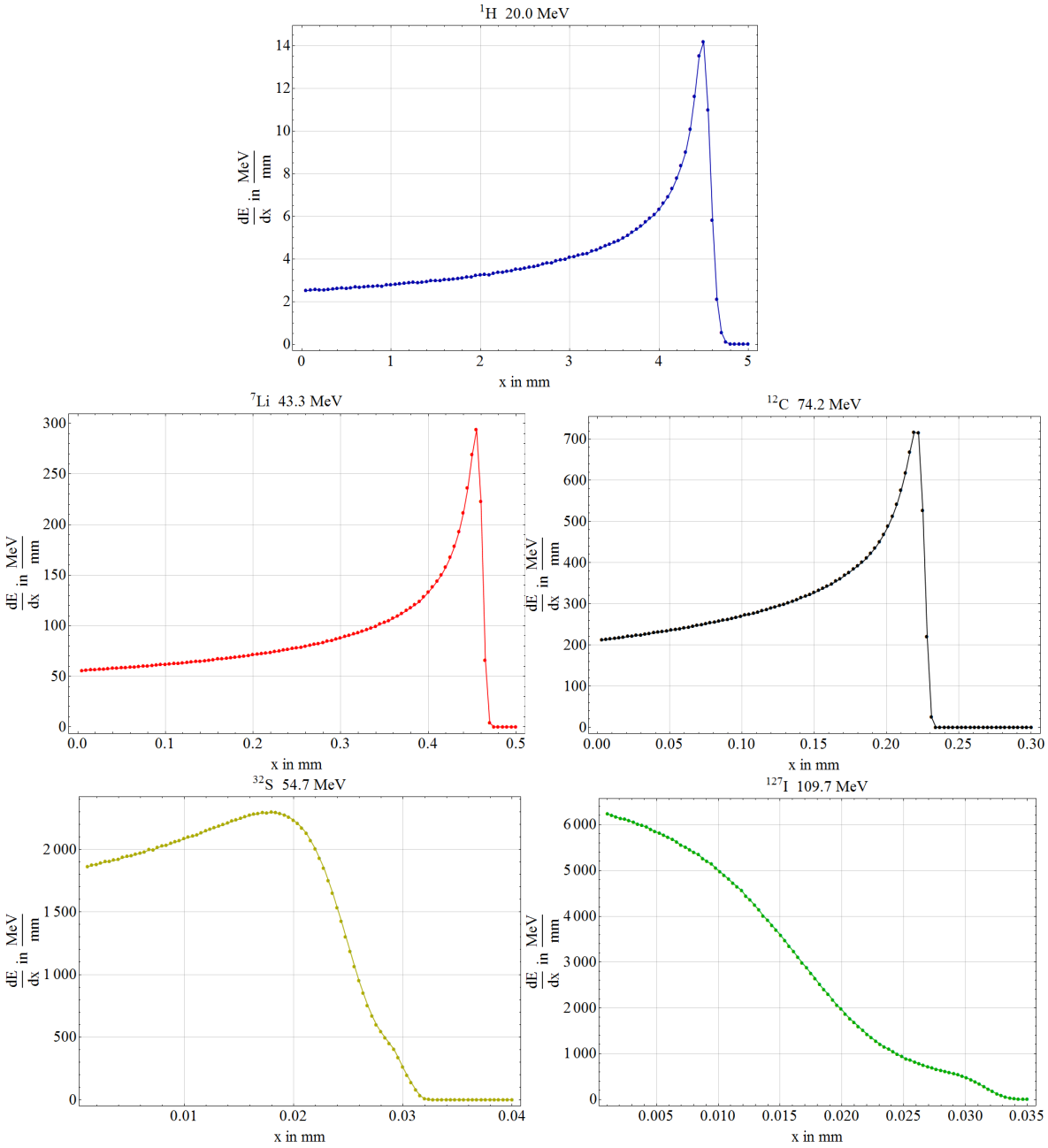


**Figure B.1:** These diagrams depict all the total stopping power curves calculated with SRIM on a double-linear scale [95]. The calculated points are joined to guide the eye. For the ions that were used with different energies, only the one with highest energy is shown. For the corresponding ion with lower energy the plotted curves are just shifted to the left (shorter range).

# Bibliography


[1] J. C. Kapteyn, *First Attempt at a Theory of the Arrangement and Motion of the Sidereal System*, The Astrophysical Journal **55**, 302 (1922)

[2] J. H. Oort, *The force exerted by the stellar system in the direction perpendicular to the galactic plane and some related problems*, Bulletin of the Astronomical Institutes of the Netherlands **6**, 249 (1932)

[3] F. Zwicky, *On the Masses of Nebulae and of Clusters of Nebulae*, The Astrophysical Journal **86**, 217 (1937)

[4] H. W. Babcock, *The rotation of the Andromeda Nebula*, Lick Observatory Bulletin **19**, 41 (1939)

[5] G. Bertone, et al., *Particle dark matter: Evidence, candidates and constraints*, Physics Reports **405**, 279 (2005)

[6] D. Clowe, et al., *A direct empirical proof of the existence of dark matter*, The Astrophysical Journal Letters **648**, L109 (2006)

[7] R. J. Gaitskell, *Direct detection of dark matter*, Annu. Rev. Nucl. Part. Sci. **54**, 315 (2004)

[8] J. E. Kim, *Light pseudoscalars, particle physics and cosmology*, Physics Reports **150**, 1 (1987)

[9] D. J. Marsh, *Axion cosmology*, Physics Reports **643**, 1 (2016)

[10] J. Liu, et al., *Current status of direct dark matter detection experiments*, Nature Physics **13**, 212 (2017)

[11] C. Amole, et al., *Dark matter search results from the PICO-60 $CF_3I$ bubble chamber*, Physical Review D **93**, 052014 (2016)

[12] A. Aguilar-Arevalo, et al., *Search for low-mass WIMPs in a 0.6 kg day exposure of the DAMIC experiment at SNOLAB*, Physical Review D **94**, 082006 (2016)

[13] W. Zhao, et al., *Search of low-mass WIMPs with a p-type point contact germanium detector in the CDEX-1 experiment*, Physical Review D **93**, 092003 (2016)

[14] R. Agnese, et al., *Demonstration of surface electron rejection with interleaved germanium detectors for dark matter searches*, Applied Physics Letters **103**, 164105 (2013)

[15] R. Agnese, et al., *Search for low-mass weakly interacting massive particles with SuperCDMS*, Physical Review Letters **112**, 241302 (2014)

[16] M. Bravin, et al., *The CRESST dark matter search*, Astroparticle Physics **12**, 107 (1999)

[17] R. F. Lang, et al., *Search for dark matter with CRESST*, New Journal of Physics **11**, 105017 (2009)

[18] R. Strauss, et al., *A prototype detector for the CRESST-III low-mass dark matter search*, Nuclear Instruments and Methods in Physics Research Section A: Accelerators, Spectrometers, Detectors and Associated Equipment **845**, 414 (2017)

[19] F. Petricca, et al., *First results on low-mass dark matter from the CRESST-III experiment*, arXiv preprint arXiv:1711.07692 (2017)

[20] D. Gastler, et al., *Measurement of scintillation efficiency for nuclear recoils in liquid argon*, Physical Review C **85**, 065811 (2012)

[21] M. Schumann, *Dark matter search with liquid noble gases*, arXiv preprint arXiv:1206.2169 (2012)

[22] A. Morozov, et al., *Conversion efficiencies of electron beam energy to vacuum ultraviolet light for Ne, Ar, Kr, and Xe excited with continuous electron beams*, Journal of Applied Physics **103**, 103301 (2008)

[23] G. F. Knoll, *Radiation detection and measurement*, John Wiley & Sons (2010)

[24] E. Aprile, et al., *Energy resolution studies of liquid argon ionization detectors*, Nuclear Instruments and Methods in Physics Research Section A: Accelerators, Spectrometers, Detectors and Associated Equipment **261**, 519 (1987)

[25] H. Ichinose, et al., *Energy resolution for gamma-rays and electrons from $^{207}Bi$ in liquid Xe doped with TEA*, Nuclear Instruments and Methods in Physics Research Section A: Accelerators, Spectrometers, Detectors and Associated Equipment **322**, 216 (1992)

[26] E. Aprile, *Noble gas detectors*, John Wiley & Sons (2006)

[27] L. Miller, et al., *Charge transport in solid and liquid Ar, Kr, and Xe*, Physical Review **166**, 871 (1968)

[28] E. Shibamura, et al., *Drift velocities of electrons, saturation characteristics of ionization and W-values for conversion electrons in liquid argon, liquid argon-gas mixtures and liquid xenon*, Nuclear Instruments and Methods **131**, 249 (1975)

[29] E. Aprile, et al., *A study of ionization electrons drifting large distances in liquid and solid argon*, Nuclear Instruments and Methods in Physics Research Section A: Accelerators, Spectrometers, Detectors and Associated Equipment **241**, 62 (1985)

[30] B. Dolgoshein, et al., *New method of registration of ionizing-particle tracks in condensed matter*, ZhETF Pisma Redaktsiiu **11**, 513 (1970)

[31] K. Masuda, et al., *A liquid xenon position sensitive gamma-ray detector for positron annihilation experiments*, Nuclear Instruments and Methods in Physics Research **188**, 629 (1981)

[32] A. Bolozdynya, et al., *Emission detectors*, IEEE Transactions on Nuclear Science **42**, 565 (1995)

[33] A. I. Bolozdynya, *Two-phase emission detectors: foundations and applications*, IEEE Transactions on Dielectrics and Electrical Insulation **13**, 616 (2006)

[34] E. Aprile, et al., *Proportional light in a dual-phase xenon chamber*, IEEE Transactions on Nuclear Science **51**, 1986 (2004)

[35] C. Hagmann, et al., *Two-phase emission detector for measuring coherent neutrino-nucleus scattering*, IEEE Transactions on Nuclear Science **51**, 2151 (2004)

[36] E. Aprile, et al., *Liquid xenon detectors for particle physics and astrophysics*, Reviews of Modern Physics **82**, 2053 (2010)

[37] A. Di Giovani, *The XENON1T Dark Matter Experiment*, Proceedings, 51st Rencontres de Moriond, Cosmology session (2016)

[38] R. Lang, *The XENON Experiment (Homepage)*, URL `http://www.xenon1t.org/`, retrieved 2018-01-24 (2017)

[39] D. McKinsey, et al., *The LUX dark matter search*, in *Journal of Physics: Conference Series*, volume 203, 012026, IOP Publishing (2010)

[40] B. Mount, et al., *LUX-ZEPLIN (LZ) Technical Design Report*, arXiv preprint arXiv:1703.09144 (2017)

[41] X. Cao, et al., *PandaX: a liquid xenon dark matter experiment at CJPL*, Science China Physics, Mechanics & Astronomy **57**, 1476 (2014)

[42] X. Cui, et al., *Dark matter results from 54-ton-day exposure of PandaX-II experiment*, Physical Review Letters **119**, 181302 (2017)

[43] P. Meyers, et al., *DarkSide-50: a WIMP search with a two-phase argon TPC*, Physics Procedia **61**, 124 (2015)

[44] P. Agnes, et al., *First results from the DarkSide-50 dark matter experiment at Laboratori Nazionali del Gran Sasso*, Physics Letters B **743**, 456 (2015)

[45] K. Abe, et al., *XMASS detector*, Nuclear Instruments and Methods in Physics Research Section A: Accelerators, Spectrometers, Detectors and Associated Equipment **716**, 78 (2013)

[46] K. Ichimura, *XMASS 1.5, the next step of the XMASS experiment*, Proceedings of Science 1223 (2015)

[47] M. Kuźniak, et al., *DEAP-3600 dark matter search*, Nuclear and Particle Physics Proceedings **273**, 340 (2016)

[48] C. Jillings, et al., *Search for Dark Matter with DEAP-3600*, in *APS Meeting Abstracts* (2017)

[49] C. Wiesinger, *The TUM Liquid Argon Test Stand: Commissioning and Characterization of a Low Background Test Stand for Background Suppression Studies in the Frame of the GERDA ($0\nu\beta\beta$)-Experiment*, Master-thesis, TUM (2014)

[50] M. Agostini, et al., *First results of GERDA Phase II and consistency with background models*, in *Journal of Physics: Conference Series*, volume 798, 012106, IOP Publishing (2017)

[51] T. Heindl, et al., *The scintillation of liquid argon*, EPL (Europhysics Letters) **91**, 62002 (2010)

[52] A. Neumeier, et al., *Attenuation measurements of vacuum ultraviolet light in liquid argon revisited*, Nuclear Instruments and Methods in Physics Research Section A: Accelerators, Spectrometers, Detectors and Associated Equipment **800**, 70 (2015)

[53] A. Neumeier, et al., *Intense vacuum ultraviolet and infrared scintillation of liquid Ar-Xe mixtures*, EPL (Europhysics Letters) **109**, 12001 (2015)

[54] A. Neumeier, *Optical Properties of Liquid Noble Gas Scintillators*, Dissertation, Technische Universität München, Physik-Department (2015)

[55] Y. Tanaka, et al., *Continuous emission spectrum of xenon in the vacuum ultraviolet region*, JOSA **44**, 254_1 (1954)

[56] C. K. Rhodes, *Excimer lasers*, Springer-Verlag New York Inc., New York, NY (1984)

[57] A. R. Striganov, et al., *Tables of spectral lines of neutral and ionized atoms*, IFI / Plenum Data Corporation, translated from Russian (1968)

[58] A. Bondar, et al., *Study of infrared scintillations in gaseous and liquid argon. Part I: methodology and time measurements*, Journal of Instrumentation **7**, P06015 (2012)

[59] A. Bondar, et al., *Study of infrared scintillations in gaseous and liquid argon. Part II: light yield and possible applications*, Journal of Instrumentation **7**, P06014 (2012)

[60] T. Alexander, et al., *Near-infrared scintillation of liquid argon*, Journal of Instrumentation **11**, C03010 (2016)

[61] T. Heindl, *Die Szintillation von flüssigem Argon*, Dissertation, Technische Universität München (2011)

[62] S. Lawton, et al., *The high-pressure neutral infrared xenon laser*, Journal of Applied Physics **50**, 3888 (1979)

[63] A. Ulrich, et al., *Lasers in dense gases pumped by low-energy electron beams*, Journal of Applied Physics **86**, 3525 (1999)

[64] C. Skrobol, et al., *A miniature electron beam pumped laser*, The European Physical Journal D - Atomic, Molecular, Optical and Plasma Physics **54**, 103 (2009)

[65] G. Nowak, et al., *The heteronuclear excimers ArKr*, ArXe* and KrXe*, Journal of Physics B: Atomic and Molecular Physics **18**, 1355 (1985)

[66] A. Neumeier, et al., *Intense infrared scintillation of liquid Ar-Xe mixtures*, EPL (Europhysics Letters) **106**, 32001 (2014)

[67] A. Neumeier, et al., *Attenuation of vacuum ultraviolet light in pure and xenon-doped liquid argon—An approach to an assignment of the near-infrared emission from the mixture*, EPL (Europhysics Letters) **111**, 12001 (2015)

[68] B. Raz, et al., *Experimental evidence for trapped exciton states in liquid rare gases*, in *Proceedings of the Royal Society of London A: Mathematical, Physical and Engineering Sciences*, volume 317, 113–131, The Royal Society (1970)

[69] O. Cheshnovsky, et al., *Emission spectra of deep impurity states in solid and liquid rare gas alloys*, The Journal of Chemical Physics **57**, 4628 (1972)

[70] T. Efthimiopoulos, et al., *Excimer emission spectra of rare gas mixtures using either a supersonic expansion or a heavy-ion-beam excitation*, Journal of Physics D: Applied Physics **30**, 1746 (1997)

[71] T. Heindl, et al., *Table-top setup for investigating the scintillation properties of liquid argon*, Journal of Instrumentation **6**, P02011 (2011)

[72] A. Hitachi, et al., *Effect of ionization density on the time dependence of luminescence from liquid argon and xenon*, Physical Review B **27**, 5279 (1983)

[73] P. Peiffer, et al., *Pulse shape analysis of scintillation signals from pure and xenon-doped liquid argon for radioactive background identification*, Journal of Instrumentation **3**, P08007 (2008)

[74] M. Hofmann, et al., *Ion-beam excitation of liquid argon*, The European Physical Journal C **73**, 2618 (2013)

[75] E. Kobetich, et al., *Energy deposition by electron beams and $\delta$ rays*, Physical Review **170**, 391 (1968)

[76] F. A. Cucinotta, et al., *Heavy Ion Track-Structure Calculations for Radial Dose in Arbitrary Materials*, Technical Memorandum 3497, University of Nebraska, National Aeronautics and Space Administration (1995)

[77] S. Valkealahti, et al., *Energy deposition of keV electrons in light elements*, Journal of Applied Physics **65**, 2258 (1989)

[78] A. Ulrich, et al., *Anregung dichter Gase mit niederenergetischen Elektronenstrahlen: Neue Wege zu brillanten Lichtquellen und Excimer-Lasern*, Physikalische Blätter **56**, 49 (2000)

[79] M. Waligorski, et al., *The radial distribution of dose around the path of a heavy ion in liquid water*, International Journal of Radiation Applications and Instrumentation. Part D. Nuclear Tracks and Radiation Measurements **11**, 309 (1986)

[80] M. Toulemonde, et al., *Temperature and pressure spikes in ion-beam cancer therapy*, Physical Review E **80**, 031913 (2009)

[81] M. Toulemonde, *Privat Communication* (2017)

[82] M. Hofmann, *Liquid Scintillators and Liquified Rare Gases for Particle Detectors Background-Determination in Double Chooz and Scintillation Properties of Liquid Argon*, Dissertation, TUM (2012)

[83] D. Akimov, et al., *Study of Xe-doping to LAr scintillator*, in *Journal of Physics: Conference Series*, volume 798, 012210, IOP Publishing (2017)

[84] K. Hamamatsu Photonics, *Photomultiplier tubes: Basics and applications*, Edition 3a **310** (2007)

[85] E. T. D. Hamamatsu Photonics K.K., *Final Test Sheet*, delivered (2014)

[86] Thorlabs, *InGaAs Photodiode*, URL `https://www.thorlabs.com/_sd.cfm?fileName=2234-S01.pdf&partNumber=FGA10`, retrieved 2012-01-31 (2017)

[87] H. Geissel, et al., *ATIMA*, URL `http://web-docs.gsi.de/~aprochaz/webatima/`, retrieved 2017-03-24 (2014)

[88] L. C. Northcliffe, et al., *Range and stopping-power tables for heavy ions*, Atomic Data and Nuclear Data Tables **7**, 233 (1970)

[89] A. Neumeier, et al., *Attenuation of vacuum ultraviolet light in liquid argon*, The European Physical Journal C **72**, 2190 (2012)

[90] A. Neumeier, *Privat Communication* (2016)

[91] A. Hitachi, et al., *Luminescence quenching in liquid argon under charged-particle impact: Relative scintillation yield at different linear energy transfers*, Physical Review B **46**, 11463 (1992)

[92] A. Mozumder, *Track-core radius of charged particles at relativistic speed in condensed media*, The Journal of Chemical Physics **60**, 1145 (1974)

[93] W. Stapor, et al., *Practical approach to ion track energy distribution*, Journal of Applied Physics **64**, 4430 (1988)

[94] W. Wesch, et al. (editors), *Ion Beam Modification of Solids*, Springer (2016)

[95] J. F. Ziegler, et al., *SRIM–The stopping and range of ions in matter (2010)*, Nuclear Instruments and Methods in Physics Research Section B: Beam Interactions with Materials and Atoms **268**, 1818 (2010)

[96] S. B. Roth, *The potential of Neganov-Luke amplified cryogenic light detectors and the scintillation-light quenching mechanism in $CaWO_4$ single crystals in the context of the dark matter search experiment CRESST-II*, Dissertation, Technische Universität München (2013)

[97] D. Verner, et al., *Atomic data for permitted resonance lines of atoms and ions from H to Si, and S, Ar, Ca, and Fe*, Atomic Data and Nuclear Data Tables **64**, 1 (1996)

[98] A. Kramida, et al., *NIST Atomic Spectra Database (ver. 5.5.1)*, URL `https://physics.nist.gov/asd`, retrieved 2017-11-09 (2017)

[99] J. Roth, et al., *Molecular dynamics simulations studies of laser ablation in metals* **1464**, 504 (2012)

[100] M. Toulemonde, et al., *Experimental phenomena and thermal spike model description of ion tracks in amorphisable inorganic insulators*, Mat. Fys. Medd **52**, 263 (2006)

[101] W. Potzel, *Privat Communication* (2017)

[102] S. Messenger, et al., *Nonionizing energy loss (NIEL) for heavy ions*, IEEE Transactions on Nuclear Science **46**, 1595 (1999)

[103] W. H. Barkas, *Nuclear research emulsions. Vol. 1: Techniques and theory*, New York: Academic Press (1963)

[104] T. Doke, et al., *Estimation of absolute photon yields in liquid argon and xenon for relativistic (1 MeV) electrons*, Nuclear Instruments and Methods in Physics Research Section A: Accelerators, Spectrometers, Detectors and Associated Equipment **291**, 617 (1990)

[105] P. Sigmund, et al., *Sputtering from elastic-collision spikes in heavy-ion-bombarded metals*, Journal of Applied Physics **52**, 990 (1981)

[106] M. Toulemonde, et al., *Synergy of nuclear and electronic energy losses in ion-irradiation processes: The case of vitreous silicon dioxide*, Physical Review B **83**, 054106 (2011)

[107] E. Aprile, et al., *Scintillation response of liquid xenon to low energy nuclear recoils*, Physical Review D **72**, 072006 (2005)

[108] V. D. Ingenieure (editor), *VDI Wärmeatlas*, Springer, 10th edition (2006)

[109] W. M. Haynes (editor), *CRC handbook of chemistry and physics*, CRC press, 93rd edition (2012)

[110] W. M. P.J. Linstrom (editor), *NIST Chemistry WebBook, NIST Standard Reference Database Number 69*, National Institute of Standards and Technology, Gaithersburg MD, Gaithersburg, MD 20899, URL `http://webbook.nist.gov/`, retrieved 2017-09-21

[111] E. Lemmon, et al., *REFPROP 9.1*, NIST Standard Reference Database **23** (2013)

[112] H. Kuchling, *Taschenbuch der Physik*, Carl Hanser Verlag München, 19th edition (2007)

[113] A. Liquide, *Gas encyclopaedia*, Gas Encyclopedia URL `https://encyclopedia.airliquide.com/`, retrieved 2017-09-22

# Danksagung

An allererster Stelle möchte ich meinem Doktorvater Prof. Dr. Andreas F. Ulrich danken, für seine intensive Betreuung ab der ersten Stunde. Mit ihm stand mir seit meiner Master-Arbeit ein sehr erfahrener Experimentator zur Seite, der mir bei so vielen Versuchen über die Schulter blickte und immer hoch interessiert an den neusten Ergebnissen war. Die vielen Stunden, mit denen ich mit ihm über die Versuchsaufbauten, die Durchführung der Experimente und die Physik dahinter diskutieren durfte, lehrten mich die Kunst der Experimentalphysik zu perfektionieren. Als Privatdozent des Lehrstuhls E12 - "Hadronen und Kerne" war er ebenso wie ich als Doktorand von der Auflösung desselben Betroffen und wir hatten gemeinsam eine ungewisse Zeit mit vielen Hürden zu durchleben. Die interessante Gespräche über alltägliche Themen und über die Abenteuer seine Hündin Mocca waren dabei eine willkommene Abwechslung und werden mir immer in guter Erinnerung bleiben.

Meine Anstellung als Doktorand wurde erst durch Prof. Dr. Stefan Schönert ermöglicht. Ich möchte ihm nicht nur dafür danken, dass er damals in den ungewissen Stunden als kommissarischer Leiter den sterbenden Lehrstuhl E12 die Hand gereicht hat, sondern auch dafür, dass er die kleine Gruppe um Prof. Ulrich in seinem sehr erfolgreichen Lehrstuhl E15 - "Experimentelle Astroteilchenphysik" aufgenommen und ein sicheres Umfeld gegeben hat. Als hauptamtlicher Leiter des Lehrstuhls und Teilhaber an zahlreichen Experimenten ein vielbeschäftigter Professor der dennoch nicht zögerte, sich als Mentor für mich zur Verfügung zu stellen.

Auch Prof. Dr. Lothar Oberauer, zweiter Professor am Lehrstuhl E15, möchte ich an dieser Stelle lobend erwähnen. Mit seiner offenen ermunternden Art hat er uns allen die Arbeit am Lehrstuhl immer angenehm gemacht hat.

Mit Dr. Jochen Wieser durfte ich einem sehr erfahrenem Experimentalphysiker begegnen, dessen Wissen mir immer noch unerschöpflich scheint. Sei es bei den Details der Versuchsaufbauten und deren Bedienung, bei allgemeinen Themen über Medizin bis Schifffahrt oder bei Tipps für den Alltag. Wann immer ich im Zweifel über den physikalischen Hintergrund oder der technischen Durchführung eines

Experiments war, konnte ich nach den Diskussionen mit ihm die Arbeit erfolgreich fortsetzen. Vielen Dank für deine Hilfe Jochen und “lass’ uns schütteln die Hände!”

Einen herzlichen Gruß darf ich an Prof. Dr. Marcel Toulemonde richten, ehemals Direktor der Forschungsabteilung am Grand Accélérateur National d’Ions Lourds des CIMAP-Labors, der nicht zögerte meine Arbeit mit seiner Expertise auf dem Gebiet der Festkörperphysik zu unterstützen. Zahlreiche Diskussionen brachten mir die gelebte Internationalität der Forschung nahe. Seinen Aufwand für meine Forschung kann ich gar nicht genug honorieren.

Herrn Dr. Walter Potzel lernte ich als hocherfahrene Leseratte des Lehrstuhls E15 kennen. Er bügelt kritisch auch die kleinsten Fehler in Publikationen wie Dissertationen aus und war gleichzeitig unserer Arbeit gegenüber immer aufgeschlossen und enthusiastisch. Selten begegnet man heute noch Menschen, die fremden Ideen so offen gegenüberstehen.

Einen ganz besonderen Dank gilt Dr. Dominik Hellgartner, der mir trotz seiner eigenen stressigen Arbeit immer voller Elan geholfen hat. Nicht nur, dass er seine altgediente Elektronik zur Verfügung stellte, er investierte auch seine wertvolle Zeit bis zur vollständigen Einsatzbereitschaft der von ihm vervollständigten Datenaufnahme meines Experiments.

Mit Dr. Tina Pollmann stand mit eine versierte Kollegin zur Verfügung, die mir immer gerne Einsicht in die Arbeit der DEAP-Kollaboration und deren Flüssig-Argon-Detektor gab. Ihre detaillierten Erklärungen vervollständigten mein Verständnis über die Anwendung einsatzbereiter Detektoren für die Suche nach Dunkler Materie. Vielen Dank Tina, für deine gelebte Politik der offenen Bürotür!

Unvergessen wird mir meine Zeit in der kleinen Gruppe um Priv.-Doz. Dr. A. F. Ulrich bleiben: Meine beiden Vorgänger Dr. Thomas Dandl und Dr. Alexander M. Neumeier sowie mein Nachfolger Raphael J. Hampf. Mit ihnen durfte ich viele praktische Erfahrung sammeln und weitergeben, sowohl für die Uni, als auch für das Leben. Die vielen produktiven und lustigen Stunden haben immer für eine gute Arbeitsatmosphäre gesorgt.

Nichts läuft in der Experimentalphysik ohne selbstentworfene Versuchsaufbauten. Doch gebaut werden die meisten Komponenten nicht selbst. Die Werkstatt-Crew von E12, Ralf Lang und Michael Klöckner, die Besetzung bei E15, Harald Hess und Thomas Richter, sowie die Belegschaft am Maier-Leibnitz-Laboratorium, Fritz Haftlmeier und Georg Obermaier, ermöglichten mir erst die Realisierung dieser Doktorarbeit. Bei Ralf und Michael, die mir auch nach meinem erzwungenen Wechsel zu E15 das ein oder andere ’heiße Eisen schmiedeten’, lernte ich viel über ihre Arbeit an den Dreh- und Fräsmaschinen und bekam ein ganz neuen Blick auf unsere technische Welt. Für einen geselligen Plausch war Ralf immer zu haben,

womit das Klima nicht nur in der Werkstatt an heißen Sommertagen erträglicher wurde. Fritz und Georg waren immer sofort zu Stelle, was bei der Vorbereitung oder gar während einer Strahlzeit am Beschleuniger von unschätzbarem Wert ist. Und da man sich auch bei Harald und Thomas immer auf freundlichem Terrain bewegte, konnte ich zu Stoßzeiten sogar des Öfteren mehrere Werkstätten gleichzeitig 'belegen'.

Es ist nicht allzu selten, dass man an einer Universität altgediente Mitarbeiter findet, denen ihr Beitrag zur Wissenschaft wichtiger ist als die Abgeschiedenheit eines Ruhestands. Das Engagement von Herrn Hermann Hagn allerdings übertraf meine Vorstellungen bei Weitem. Eine Koryphäe auf dem Gebiet der Elektrotechnik, die seinesgleichen sucht und die erst nach einem erfahrungsreichen Berufsleben zwischen den Akademikern Fuß gefasst hat. Das enormen Wissen und die Fähigkeit es in die Praxis umzusetzen hat mich nicht nur einmal an der theoretischen Ausbildung durch die Universität, welche selbst in der Experimentalphysik in vielen Semestern üblich ist, zweifeln lassen. Ich möchte Herrn Hagn im Namen aller Studenten und Doktoranden dafür danken, dass er über viele Jahre unsere Experimente zum Laufen und uns die Kniffe der Hochfrequenztechnik näher gebracht hat.

Das Maier-Leibnitz-Laboratorium, von manchen vielleicht auf Grund seines fortgeschrittenen Alters verlacht, stellt eine wahre Wunderwaffe in allen Forschungsbereichen der Beschleunigerphysik dar. Das verdankt es seiner beherzten Crew, die allen Widrigkeiten zum Trotz nicht aufgibt. Da wäre zum einen ihr technischer Leiter, Dr. Ludwig Beck, der das Labor mit besonnener Hand für das Forschungskollegium führt und immer darum bestrebt ist, dem Nachwuchs die Faszination Forschung näher zu bringen. Es war mir eine Ehre, ihm in diesem Belang bei der Führung von Besuchergruppen tatkräftig unterstützen zu dürfen. 'Gefahren' wird Linearbeschleuniger von weniger als einer Hand voll Operateure. Dem technischen Personal – zu dem zu Beginn meiner Arbeit Michi Wiesheu, Oliver Gosau, Michi Pelzer und Christian Lenz angehörten – ist es zu verdanken, dass das 'U-Boot' aus den 1970er Jahren immer noch Dutzende von Wissenschaftlern mit Ionenstrahlen versorgt. Es war immer wieder ein Genuss, das eingespielte Team in Aktion zu sehen.

Dem gesamten Lehrstuhl E15 – auch allen bisher nicht namentlich Genannten – möchte ich für die herzliche Aufnahme nach der Auflösung von E12 danken. Man ist immer sofort unter Gleichgesinnten und Freunden.

An dieser Stelle möchte ich die hervorragende Arbeit der E15-Sekretärin Sabine Kaps würdigen. Man zögerte keine Sekunde mit Verwaltungsfragen zur ihr zu kommen und sie wusste immer Rat. Auch die hingebungsvolle Betreuung der E15-Küche sollte nicht als selbstverständlich betrachtet werden.

Bereits vor meiner Zeit bei E15 konnte ich mich auf die Sekretärinnen von E12, Petra Zweckinger und Sigrid Weichs, verlassen. Auch nach Abwerbung von

Sabine Kaps kam ich gerne zurück in das altbekannte E12-Sekretariat, welches den Lehrstuhl E15 übergangsweise betreute. Meinen herzlichen Dank an die, die das Chaos im Zaum halten.

Das von manchen Doktoranden als lästig erachtete Sammeln von Lehrpunkten wurde mir im doch recht zeitaufwendigen Demonstrationspraktikum von Dr. Dieter Brunner, Dr. Andreas Hauptner und Dr. Karl Dressler als angenehme Abwechslung zum manchmal recht stressigen Labor- oder Büroalltag ermöglicht. Die Möglichkeit zukünftigen Lehrkräften mit zahlreichen Tipps für Schulexperimente zur Hand zu gehen sowie ihre Vortragsfähigkeiten und ihren Unterrichtsstil zu verbessern, war für mich eine verantwortungsvolle Aufgabe, der ich mich gerne jedes Semester einen Nachmittag pro Woche gewidmet habe. Die Diskussionen mit Dieter, Andreas und Karl bereicherten meinen Horizont, sowohl physikalisch als auch politisch und menschlich.

Einen ganz speziellen Dank spreche ich an das Städtische Bauamt 2 aus, das in enger und intensiver Zusammenarbeit mit dem Maier-Leibnitz-Laboratorium und den beteiligten Universitäten sowohl dafür gesorgt hat, dass das Labor nach einem etwa zehnjährigen Vorlauf aus Brandschutzgründen geschlossen werden musste – wobei alle Forschungsarbeiten eingestellt wurden – und auf Drängen der gesammelten Professoren und Studentenschaft nach nur einem Jahr Sperrung mit Einschränkungen wiedereröffnet werden konnte. Ein ganz besondere Erwähnung hat hierbei die Transparenz und die Kommunikation verdient, mit der die Maßnahmen im Voraus angekündigt wurden. — Der Einfluss, den manche Entscheidungen auf die Durchführung oder Nichtdurchführung von experimentellen Arbeiten haben, darf nicht unterschätzt werden. Es ist von meinem Standpunkt aus unbedingt notwendig, dass die Politik nachhaltige Maßnahmen ergreift, um den Forschungsstandort Deutschland in vielen Disziplinen konkurrenzfähig zu halten.

Neben den Menschen, denen ich erst im Zusammenhang mit meiner Doktorarbeit begegnet bin, haben auch Personen aus meinem persönlichen Umfeld erheblich zum Gelingen dieser Arbeit beigetragen. Dazu gehört allen voran mein ehemaliger Schulkamerad und guter Freund Andreas T. Rarrek, der zur selben Zeit im Maschinenwesen mit seiner eigenen Dissertation beschäftigt war. Die intensiven Diskussionen über unsere beiden Arbeiten eröffneten einen neuen Blickwinkel für den jeweils anderen und verhalfen zu manch neuen Ansätzen der Problemlösung.

Einen besonders herzlichen Dank möchte ich schlussendlich meiner Familie aussprechen, die mich immer bedingungslos in meinem Bestreben unterstützt hat. Die – auch wenn ihnen die Physik fern liegt – nie an meiner Arbeit gezweifelt hat und mir das sichere und entspannte Umfeld bereitgestellt hat, das nötig war, um meine Energie auf meine Doktorarbeit zu konzentrieren. Ich bin dafür sehr dankbar und ich weiß, dass es nicht selbstverständlich ist, eine liebende und fürsorgende Familie zu haben.